Technical University of Denmark

DTU

Structure and transport properties of atomic chains and molecules

Strange, Mikkel; Jacobsen, Karsten Wedel; Thygesen, Kristian Sommer

[Link back to DTU Orbit](#)

DTU Library
Technical Information Center of Denmark

Abstract

The work presented in this thesis is based on density functional theory (DFT) applied mainly to calculate conductance properties of nano-scale systems.

A full charecterization of Ag-oxygen chains between Ag contacts has been performed. Using spin DFT the electronic and magnetic properties of atomically thin, suspended chains containing silver and oxygen atoms in an alternating sequence has been studied. The conductances of the chains exhibit weak even-odd oscillations around an anomalously low value of $0.1G_0$ ($G_0 = 2e^2/h$) in agreement with experiments [1] in the long chain limit. These unusual conductance properties are explained in terms of a resonating-chain model, which takes the reflection probability and phase-shift of a single bulk-chain interface as the only input. The stability of silver-oxygen chains was studied with a thermodynamic model. This model has been developed in this work to describe tip-suspended atomically thin chains between macroscopic size electrodes. It has been tested with the use of DFT calculations on metal chains for which good agreement with experiments was obtained.

To ensure the correctness of the DFT based transport calculations presented here, and in more general in the literature, a set of benchmark calculations for the Kohn-Sham elastic transmission function of representative single-molecule junctions has been performed. The transmission functions are calculated using two different density functional theory methods, namely an ultrasoft pseudopotential plane-wave code DACAPO [2] in combination with maximally localized Wannier functions and the norm-conserving pseudopotential code SIESTA [3] which applies an atomic orbital basis set. For the systems studied we find that the SIESTA transmission functions converge toward the plane-wave result as the SIESTA basis is enlarged. Overall, we find that a double zeta polarized atomic basis is generally sufficient, and in some cases necessary, to ensure quantitative agreement with the plane-wave calculation.

In a detailed DFT study of the carbon monoxide molecule between Pt electrodes, a particularly stable tilted bridge configuration is found, with a conductance of $0.5G_0$ over a wide range of electrode displacements. This is in agreement

with the observed peak at $0.5G_0$ in the experimentally obtained conductance histogram for Pt/CO [4]. Also, for homogenous Pt point contacts and short chains good agreement with experiments is obtained. A study of CO in Au, Cu and Ni, reveals that the conductance for CO in the tilted bridge configuration for Ni is $0.5G_0$, in agreement with experiments [5]. For Au/CO and Cu/CO we find the effect of CO compared to the homogenous metal contacts is much smaller, in qualitative agreement with the experimental findings [5]. The observed conductance properties of Metal/CO are shown to be determined by the local d-band at the Metal apex atoms.

For carbon nanotubes it is shown that the conductance may be controlled by site selective adsorption of molecules. A model to explain this behavior is verified by direct visualization of Kohn-Sham eigenchannel states. The possibility of non-carbon based nanotubes is also discussed. Both calculations of the strain energy of infinite PtO_2 nanotubes that this material could be a candidate for non-carbon based nanotubes, as was recently suggested [6].

Resumé

I denne Ph.D afhandling bliver tæhedsfunktional teori (DFT) anvendt i en række studier af systemers strukturer og elektriske ledningsegenskaber på nanometer-skala.

En fuldstændig karakterisering af atomare sølv-ilt kæder udspændt imellem sølv elektroder er blevet udført. Baseret på spin-DFT er de elektriske og magnetiske egenskaber af alternerende sølv-ilt kæder blevet studeret. Ledningsevnen af kæderne viser sig at oscillere som funktion af kædelængden med en lille amplitude omkring en usædvanlig lav konduktans på $0.1G_0$ ($G_0 = 2e^2/h$). Dette er i overenstemmelse med eksperimenter [1] i grænsen for lange kæder. De specielle ledningsegenskaber forklares ved hjælp af en resonans model for atomare kæder. Modellen afhænger kun af reflektionssandsynligheden og faseskiftet af en elektron, som bliver tilbagespredt på en kæde-elektrode overgang. Stabiliteten af sølv-ilt kæderne er blevet undersøgt på baggrund af en model udviklet til generelt at beskrive strengspændingen af atomare kæder imellem makroskopiske metal elektroder. Modellen viser, at sølv-ilt kæder har et lokalt minimum i strengspændingen, der indikerer, at de er specielt stabile. Et sådant lokalt minimum i strengspændingen blev desuden kun fundet for de rene metaller, som eksperimentelt er vist at danne kæder.

Dels for at sikre, at de DFT baserede elektrontransport-beregninger er korrekte og konvergerede i denne afhandling, og for at afdække de noget uoverensstemmende resultater i litteraturen, er et benchmark studie af den elastiske Kohn-Sham transmissionsfunktion blevet udført. Transmissionsfunktionen er blevet beregnet med to forskellige og uafhængige DFT koder: (i) En præcis DFT kode baseret på et planbølge basisst og ultrabløde pseudopotentialer [7] kombineret med maksimalt lokaliserede Wannier funktioner [8, 9], og (ii) en normbevarende pseudopotential kode SIESTA [3] der anvender atomare orbitaler som basisfunktioner. For de studerede systemer bliver det vist, at beregningerne af transmissionsfunktionerne med SIESTA koden konvergerer mod resultatet af den præcise planbølge baserede kode, og at et dobbelt zeta polariseret basissæt generelt er nødvendigt.

I et detaljeret DFT studie af et kuldioxid molekyle imellem Pt elektroder bliver en "tiltet-bro" identificeret som værende en specielt stabil konfiguration, der desuden har en konduktans på $0.5G_0$ i overenstemmelse med eksperimenter [5, 4]. Det vises også, at der er god overenstemmelse med ledningsevneberegningerne og etablerede eksperimenter for rene Pt kontakter [10]. Yderligere vises det, at de generelle trends af transportegenskaberne for CO i Pt, Ni, Au og Cu kontakter kan forklares af en simpel model for ledningsevnen. Modellen afdækker, at metal apex atomernes d-tilstande hovedsagligt bestemmer transportegenskaberne.

Desuden demonstreres det, at transportegenskaberne af et kulstofnanorør kan kontrolleres ved at adsorbere molekyler på bestemte sites. Muligheden for at lave små nanorør af andre materialer end kulstof er også diskutteret. Nanorør baseret på PtO_2 kunne være en mulighed, da de har en forholdsvis lav krumningsenergi, hvorimod nanorør af MoS_2 har en væsentlig højere krumningsenergi.

List of included papers

Paper I
Electron transport in a Pt-CO-Pt nanocontact: First-principles calculations
M. Strange, K. S. Thygesen, and K. W. Jacobsen
Physical Review B, **73**, 125424 (2006).

Paper II
Benchmark density functional theory calculations for nano-scale conductance
M. Strange, I. S. Kristensen, K. S. Thygesen, and K. W. Jacobsen
Journal of Chemical Physics, **114**, 114714 (2008).

Paper III
Formation and properties of metal oxygen atomic chains
W. H. A. Thijssen, M. Strange, J. M. J. aan de Brugh, and J. M. van Ruitenbeek
New Journal of Physics, **10**, 033005 (2008).

Paper IV
Site-selective chemical control of nanotubes conductivity
J. M. García-Lastra, K. S. Thygesen, M. Strange and Ángel Rubio
Submitted to Physical Review Letters.

Paper V
Anomalous Conductance Oscillations and Half-Metallicity in Atomic Ag-O Chains
M. Strange, K. S. Thygesen, J. P. Sethna, and K. W. Jacobsen
Submitted to Physical Review Letters.

Paper Vi

Electron transport in a 4,4-bipyridine molecular junctions: Role of electrode workfunction and local d-band

J. M. C. Rauba, M. Strange, and K. S. Thygesen

Contents

Chapter 1

Introduction

The work presented in this thesis is concerned with the physics of systems at the nanometer length scale and, in particular, the theoretical modeling of the electronic properties of such systems.

Thanks to advances in experimental techniques for manipulating and contacting atoms and molecules, it is today possible to form stable structures consisting of a nano-scale object, such as an organic molecule, a nanotube, or a suspended string of atoms, in contact with metallic electrodes. In this way the electrical properties, i.e. the conductance or more generally the IV characteristics, of nano structures can be directly measured. Molecular electronics could be the next step, if the incessant downscaling of semiconductor devices is to continue to the ultimate limit [11]. At this length scale quantum effects such as conductance quantization, interference of electron waves, Coulomb blockade, and Kondo effects become dominant. This demonstrates that the current description of the semiconductor based electronic devices in terms of semi-classical physics will no longer apply at such small scales [12, 13, 14]. Nano sized contacts require a new framework of ideas, representing an important scientific challenge, which has been taken up in a variety of fields. Chemists may combine their knowledge of molecules and electrochemistry with a solid state physicist's expertise in metal bulk and surface properties.

Experiments on molecular junctions are far from trivial. This is seen in the rather large variation in results obtained within a given experimental setup between different experiments. Part of the problem arises from the extreme sensitivity of the junction's electrical properties to the detailed atomic arrangement of the contacts, which is beyond experimental control. This is particularly pronounced at the nano-scale, where the electrons often travel phase-coherently through the junction. This means that interference effects are directly observable

in macroscopic quantities, such as the conductance. One example of this is the phenomena where the conductance oscillates as a function of wire length [14, 15].

The above discussion demonstrates that experiments on nano-scale junctions are quite indirect and subject to statistical fluctuations. This means that they cannot stand alone, but must be complemented by theoretical models. These models may quantify the effect of the various parameters involved, e.g. atomic geometries, electron-phonon coupling, and polarization effects of the surrounding medium. The development of such models is a great challenge, as not only the quantum nature of the electrons, but also the atomistic details of the junction must be accounted for. This calls for combining traditional first-principles electronic structure methods with the transport formalisms developed for mesoscopic systems, i.e. micro-meter sized semi-conductor structures. Indeed, the most popular approach to quantum transport in molecular junctions is based on a combination of density functional theory (DFT) [16, 17] and nonequilibrium Green's function (NEGF) techniques [18]. This method has been successful for strongly coupled systems such as homogeneous metal point contacts and monatomic wires. Here, both the size of the conductance, the number of conductance channels, and conductance oscillations are well reproduced by calculations. The same good agreement between theory and experiment has been found for a heterogeneous molecular junction consisting of a single hydrogen molecule captured between Pt electrodes [10, 19]. However, the DFT-transport method has been found to systematically overestimate the conductance of weakly coupled junctions such as benzene-dithiolate between Au electrodes [20, 21, 22]. The latter could be due to the exchange-correlation functionals, which are known to underestimate the band gap. Alternatively, the DFT-transport method may simply not be adequate, due to the underlying single-particle approximation. Finally, the experiments could be in error or the molecule may not be attached to the electrode as expected [20, 23].

The DFT-based transport calculations - which occupy the main part of this thesis - are not trivial. This is mainly because of the open boundary conditions which are required to simulate transport. Thus, a detailed atomistic description of the central nanostructure is required. At the same time the coupling to the infinite leads must also be invoked. In practice, this requires a localized basis set. However, this is incompatible with the fact that electronic wave functions tend to delocalize. One option is to transform to Wannier-like functions [9, 24, 8] to obtain a minimal and accurate basis. Another is to use atomic-like basis functions from the outset [18]. Both approaches have pros and cons which will be addressed in this thesis.

Transport calculations are very sensitive to changes in the scattering potential due to the interference effects. In fact, there are several examples in

the literature where different transmission functions have been reported for the same or very similar systems. Regardless of the validity of the DFT-transport approach in principle, and given the fact that it seems to perform well in practice for strongly coupled systems, it is important to remove such confusions and establish some benchmarks. This requires a detailed study and comparisons of independent computation schemes. Such a benchmark study has been performed in this work by comparing results from a scheme using Wannier-like orbitals obtained from accurate plane-wave calculations with results from an atomic-like basis set code.

Monatomic wires have been found to exhibit peculiar and unexpected chemical and electrical properties [25]. In recent break junction experiments it was observed that silver exposed to oxygen could form unusually long wires [26]. Also, the average conductance as a function of wire lengths was rather surprising. An initial exponential-like decrease transitioned into a constant value for long wires. In this thesis work, a full characterization of silver-oxygen monatomic chains between silver electrodes has been performed based on standard DFT and the DFT-transport method. The calculated electrical and energetic properties are both in good agreement with experiments. The former reveals the mechanism behind the unusual conductance observed for a silver contact exposed to oxygen.

As another part of this project, we studied a carbon monoxide (CO) molecule between Pt, Ni, Au and Cu electrodes. In agreement with experiments [5] a conductance of half a quantum conductance unit $0.5G_0$, $G_0 = 2e^2/h$, is observed in the calculation. This is found to be related to a special CO bridge configuration.

Finally, a project on nanotubes showed that the conductance of carbon nanotubes can be controlled by site selective adsorption of molecules. Also, materials other than carbon may be envisioned forming nanotubes having special electronic and mechanical properties. A limited study of the stability of such non-carbon nanotubes has been conducted.

Outline of the thesis

Chapter 2 is an overview of density functional theory and some aspects related to its numerical implementation.

Chapter 3 introduces a theoretical framework based on Green's functions for calculating the current through a general quantum contact.

Chapter 4 provides details on how the general Green's function transport scheme may be connected with DFT.

Chapter 5 presents a benchmark study of the DFT transport method and is a

summary of Paper II.

Chapter 5 describes a thermodynamic model for tip-suspended chains, and presents DFT calculations for metal chains.

Chapter 6 reviews an experiment on a silver/oxygen contact with silver electrodes, and presents DFT calculations to fully characterize the experimental results. This chapter is based on Paper III and V.

Chapter 7 presents the work on CO in Pt, Ni, Au and Cu nano-contacts and is primarily based on Paper I.

Chapter 8 presents work on both carbon and non-carbon nanotubes. The former is based on Paper IV.

Chapter 2

Electronic Structure Calculations

Electronic structure theory deals with the quantum mechanical description of electrons in atoms, molecules and condensed phases. The main goal of electronic structure methods is to evaluate total energies, forces, response functions and other quantities of interest. Due to increasing computer power, ab-initio electronic structure calculations have become a valuable tool for studying a variety of systems, including surfaces, nanotubes and nanocontacts.

After a brief introduction to the many-body problem, a description of the main concepts of DFT follows. The construction of explicit exchange-correlation functionals is then discussed, and finally the important aspects of the numerical implementation of DFT are outlined. Atomic units will be assumed throughout this chapter, $e^2 = \hbar = m_e = 1$, unless stated otherwise.

2.1 The many-body Hamiltonian

A system composed of negatively charged electrons and positively charged nuclei constitute matter and may be described quantum mechanically by an electronic and nuclear dependent wave function The dynamics of the wave function is governed by a self-adjoint operator on a Hilbert space: The many-body Hamiltonian. The large difference in mass between electrons and ions $(m_e/M_I \approx 10^{-3} - 10^{-6})$ suggests that the electron and ionic parts of the Hamiltonian may be decoupled. This decoupling is known as the Born-Oppenheimer approximation, and constitutes a major simplification of the many-body Hamiltonian. Here, electrons may be viewed as responding instantaneously to changes in the nuclear positions, which in turn are kept fixed. The Hamiltonian describing N electrons

moving in the field of M fixed nuclei with charges Z_a is the sum of the electron kinetic energy T, the attractive Coulumb interactions between the electrons and the fixed nuclei V_{en}, the repulsive Coulomb interaction among the electrons and nuclei, termed V_{ee} and V_{nn}, respectively, so that

$$\hat{H} = \hat{T} + \hat{V}_{en} + \hat{V}_{ee} + \hat{V}_{nn}. \tag{2.1}$$

A more explicit form may be obtained by replacing $\hat{V}_{nn}$ by a static external potential $\hat{V}_{ext}$. In the position representation the Hamiltonian in Eq. 2.1 takes the form

$$H = -\frac{1}{2} \sum_{i=1}^{N} \nabla_i^2 - \sum_{i,a} \frac{Z_a}{|\boldsymbol{r}_i - \boldsymbol{R}_a|} + \sum_{i<j} \frac{1}{|\boldsymbol{r}_i - \boldsymbol{r}_j|} + \sum_{a<b} \frac{Z_a Z_b}{|\boldsymbol{R}_a - \boldsymbol{R}_b|}, \tag{2.2}$$

and acts on the Hilbert space of complex, square integrable and anti-symmetric functions $\Psi(\boldsymbol{r}_1, \boldsymbol{r}_2, ..., \boldsymbol{r}_N)$.

Finding a ground state Ψ_0 and possible excited states Ψ_n is one of the main problems in condensed matter physics and quantum chemistry. A ground state and the corresponding energy E_0 satisfies the eigenvalue equation $H\Psi_0 = E_0\Psi_0$. The variational theorem for the ground state $E_0 \leq \langle \Psi|H|\Psi\rangle/\langle\Psi|\Psi\rangle$ directly suggests an approximate scheme where the groundstate is searched for with the help of a finite set of trial functions. Many methods in the field of quantum chemistry are based on this scheme, and one of the earliest methods along this line is the Hartree-Fock (HF) approximation.

Here, the trial functions are taken as a set of N-particle Slater determinants. The energy not accounted for in HF is generally referred to as the correlation energy $E_c^{\mathrm{HF}} = E_0 - E_0^{\mathrm{HF}}$. The HF energy usually accounts for 99% of the exact total energy but the remaining 1% turns out to be very important for describing chemical phenomena. For example,the cohesive energy of the noble metals such as Au, Cu and Ag are underestimated by a factor of 3[27] and some alkali metals are unstable at the level of HF theory [27]. To include correlation, the set of HF trial functions should obviously be extended and the question of how to accomplish this naturally arises. In configuration interaction (CI) the single Slater determinant trial function is replaced by a linear combination of Slater determinants. The Slater determinants in CI are sometimes generated by low-energy particle-hole excitations of a reference Slater determinant.

A different variational scheme is offered by the variational Quantum Monte Carlo method, where a trial function consists of a HF determinant multiplied by a tunable Jastrow factor. The Jastrow factor is designed to increase the correlation between opposite spin electrons, which is totally neglected in HF, and thereby keep them apart.

Methods based on many body perturbation theory have also been developed, such as Møller-Plesset perturbation (MP) theory [28], which take a sum of Fock operators as the unperturbed Hamiltonian. Also, single particle Green's functions may be used to obtain the ground state energy. Here, standard diagrammatic techniques may be used to sum a part of the perturbation series to infinite order. One such method is the GW approximation to Hedin's equations [29]. Regardless of the details in improving on the HF method mentioned above, all the methods share the common feature of a high computational cost.

An alternative scheme focusing on ground state properties is provided by density functional theory (DFT) [16, 17]. The electron density, which only depends on a single position $\boldsymbol{r}$, replaces the more complex objects, such as the wave functions and green's functions, which depend on the positions of all N electrons, $\boldsymbol{r}_N$, as the central object. DFT is presently the most powerful method for calculating ground state properties of atomic-scale systems. The next section is devoted to a general introduction to DFT.

2.2 Density functional theory

The Hohenberg-Kohn (HK) theorems [16] states that for a system with a non-degenerate ground state the ground state density $n(\boldsymbol{r})$ uniquely determines the external potential $V_{ext}(\boldsymbol{r})$ within an additive constant. Since the external potential in turn defines the Hamiltonian in Eq. 2.1, the electron density also determines the ground state wave function, $n_0 \to \Psi_0[n_0]$. Consequently, the correspondence $n_0 \to \langle \Psi[n_0]|\hat{A}|\Psi_0[n_0]\rangle$ shows that all ground state properties are determined by the ground state density, including the ground state energy.

The second HK theorem provide an energy variational principle $E_0 \leq E_v[\tilde{n}]$, where $\tilde{n}$ is the trial electron density. In fact, the set of trial densities $\{\tilde{n}\}$ may be associated with the ground state wave function of the Hamiltonian in Eq. 2.1 with some external potential $v_{ext}(\boldsymbol{r})$. The difficulty in mathematically characterizing this set of densities has become known as the v-representability problem. However, a more general and useful formulation of the HK theorems is known as the constrained search

$$E_v[n] = \min_{n \to N} \left\{ \min_{\Psi \to n} \langle \Psi|\hat{T} + \hat{V}_{ee}|\Psi\rangle + \int d\boldsymbol{r} v_{ext}(\boldsymbol{r})n(\boldsymbol{r}) \right\} \qquad (2.3)$$

where the search is over non-negative densities which are termed N-representable. The first term $F[n] = \min_{\Psi \to n} \left\langle \Psi|\hat{T} + \hat{V}_{ee}|\Psi \right\rangle$ does not depend on the external potential, and is in this sense a universal functional. The exact form of $F[n]$ is not known, and the constrained search approach is therefore not of practical use.

The Kohn-Sham (KS) scheme deals with this problem in a indirect but formally exact way [17].

2.3   Kohn-Sham theory

Kohn and Sham assumed that for a given interacting ground state density $n(\boldsymbol{r})$ there exists a potential v_s such that the ground state density of the non-interacting Hamiltonian $h_s = T + v_s$ is equal to the interacting ground state density $n(\boldsymbol{r})$. The potential v_s is in turn uniquely determined by $n(\boldsymbol{r})$ such that we get the energy density functional

$$E_s[n] = T_s[n] + \int v_s(\boldsymbol{r})n(\boldsymbol{r})d\boldsymbol{r}. \tag{2.4}$$

Now, the energy in Eq. (2.3) may be rewritten on the form

$$E_v[n] = T_s[n] + E_H[n] + E_{xc}[n] + \int d\boldsymbol{r}v_{ext}(\boldsymbol{r})n(\boldsymbol{r}), \tag{2.5}$$

where E_H is the classical Hartree energy and the exchange-correlation (xc) functional is defined by

$$E_{xc}[n] = F[n] - T_s[n] - E_H[n]. \tag{2.6}$$

From this definition it is clear that the xc-functional will contain the correlation contribution to the kinetic energy and the electron-electron interaction energy beyond the classical Hartree term. The principle behind introducing the xc-functional in this way is to extract as much energy as possible such that E_{xc} is a (possibly) small correction. In order to determine the potential v_s, we note that both $E_v[n]$ and $E_s[n]$ are minimized by the ground state density n_0. The variational densities should integrate to N. The minimization of $E_{v/s}[n]$ under the constraint that the variational densities should integrate to the total particle number N may be expressed in terms of functional derivatives as

$$\frac{\delta}{\delta n(\boldsymbol{r})}(E_{v/s}[n] - \mu \int n(\boldsymbol{r})d\boldsymbol{r})) = 0, \tag{2.7}$$

where μ is a Lagrange multiplier and leads to the potential v_s

$$v_s(\boldsymbol{r})[n] = v_{ext}(\boldsymbol{r}) + \int d\boldsymbol{r}' \frac{n(\boldsymbol{r}')}{|\boldsymbol{r} - \boldsymbol{r}'|} + v_{xc}(\boldsymbol{r})[n], \tag{2.8}$$

where $v_{xc}(\boldsymbol{r})$ is the exchange correlation potential defined by $\delta E_{xc}[n]/\delta n(\boldsymbol{r})$. The potential v_s defines a single particle Hamiltonian: The Kohn Sham Hamilton.

The ground state density is obtained from the N lowest Kohn Sham eigenstates. However, since v_s is dependent on the density, the solution must be obtained self-consitently, i.e. until the density defining v_s is equal to the density obtained from the corresponding Kohn Sham eigenstates.

2.4 Exchange-correlation functional

The Kohn-Sham scheme is in principle exact, but the expression for the exchange correlation functional E_{xc} is not known, and includes many body effects. In order to make the underlying physics clear, E_{xc} may be written in the form [30]

$$E_{xc}[n] = \int d\boldsymbol{r} n(\boldsymbol{r}) \int d\boldsymbol{u} \frac{\bar{n}_{xc}(\boldsymbol{r}, \boldsymbol{r} + \boldsymbol{u})}{|\boldsymbol{u}|}, \tag{2.9}$$

where $\bar{n}_{xc}(\boldsymbol{r}, \boldsymbol{r} + \boldsymbol{u}) = \int_0^1 n_{xc}^\lambda(\boldsymbol{r}, \boldsymbol{r} + \boldsymbol{u})$ is the so-called system averaged exchange correlation hole. The coupling constant $\lambda = 0$ represents a non-interacting system, while $\lambda = 1$ corresponds to the fully interacting electron system. $\bar{n}_{xc}$ is a consequence of the depletion of electrons around a single electron, since an electron at position $\boldsymbol{r}$ reduces the probability of finding another electron near this point. Integrating n_{xc}^λ over all space gives -1, implying n_{xc}^λ has the same charge as a proton.

2.4.1 Explicit exchange-correlation functionals

The simplest approximation to the exchange-correlation is obtained by assuming that the exchange-correlation hole resembles the hole in a uniform interacting electron gas with the same density. This is the local density approximation (LDA)

$$E_{xc}^{LDA} = \int n(\boldsymbol{r}) \varepsilon_{ex}^{\text{hom}}(\boldsymbol{r}) d\boldsymbol{r}. \tag{2.10}$$

The function $\varepsilon_{xc}^{\text{hom}}$ is an xc-energy density which in practice is represented by an analytic function fitted to calculations [31]. The LDA has been rather successful, despite that it is only valid for slowly varying densities. An improvement to the LDA is the so-called Generalized Gradient Approximation (GGA), where also the gradient of the density is considered

$$E_{xc}^{GGA} = \int f(n(\boldsymbol{r}), \nabla n(\boldsymbol{r})) d\boldsymbol{r}. \tag{2.11}$$

However, the function f must be chosen with care, and conditions such as the xc-hole sum rule, must be imposed by hand. The xc functional used for most

of the calculations in this work is the GGA of Perdew, Burke and Ernzerhof (PBE) [32] or the closely related PW91 GGA [33].

2.5 Numerical implementation of DFT

This section describes a selection of important aspects of the numerical implementation of a DFT code. A number of approximations are introduced and the associated error size is often a compromise between computational time and accuracy. A criteria for a reasonable error size is the requirement of being smaller than the uncertainty related to the employed approximative exchange-correlation functional. The DFT codes used throughout this work are: (i) Dacapo [2] based on plane waves, and ultrasoft pseudopotentials [7], and (ii) Siesta [3] based on atomic orbitals and norm conserving pseudopotentials. The real space code Gpaw [34] based on the projector augmented wave methods has been used occasionally.

2.5.1 Boundary conditions

The KS Hamiltonian operator is a second order partial differential operator in the position representation. To this end, a specification of certain boundary conditions is required in solving for the eigenfunctions and spectrum of the KS Hamiltonian. The choice of boundary conditions may significantly influence the spectrum and eigenfunctions. For electronic structure calculations, two types are usually employed: periodic and vanishing boundary conditions. The latter is often encountered in quantum chemistry codes, reflecting the focus on finite systems such as atoms and molecules, for which they are well-suited.

Periodic boundary conditions may be used to efficiently treat infinite periodic systems such as bulk crystals. Also, infinite systems with helical symmetry, such as nanotubes and DNA strings, may be treated using a generalized form of periodic boundary conditions where screw-operators are introduced. These are simply translational operators augmented by a rotation about the tube axis. When considering periodic systems, one may decompose the total one electron Hilbert space into $\mathbf{k}$-subspaces with the wave vector $\mathbf{k}$ in the first Brillouin zone. The Hamiltonian leaves each $\mathbf{k}$-subspace invariant and thus allows for the diagonalizing of each subspace separately resulting in a spectrum $\varepsilon_n\mathbf{k}$ and wave functions in Bloch's form [35]

$$\psi_{n\mathbf{k}}(\mathbf{r}) = e^{i\mathbf{k}\cdot\mathbf{r}}u_{n\mathbf{k}}\mathbf{r}, \tag{2.12}$$

where $u_{n\mathbf{k}}(\mathbf{r})$ is a function with the periodicity of the underlying lattice.

By forming supercells, it is possible to model a much larger class of non-periodic structures using periodic boundary conditions. Within the supercell approach, the system of interest is modeled within a finite cell which is repeated in all directions to form a super-lattice. In this way, molecules may be modeled by including an appropriate amount of vacuum regions in the supercell such that molecules in the superlattice do not interact. Also, surfaces may be modeled in this way by introducing a surface slab. The ground state expectation value of a one particle operator R is to be calculated as an integral over the first Brillouin zone

$$\langle R \rangle = \frac{1}{V_{\text{BZ}}} \int_{\text{BZ}} R(\mathbf{k}) d\mathbf{k}, \qquad (2.13)$$

where V_{BZ} is the volume of the first Brillouin zone and $R(\mathbf{k}) = \sum_{n \in \text{occ}} \langle \psi_{n\mathbf{k}} | R | \psi_{n\mathbf{k}} \rangle$. In practice the Brillouin zone integral is approximated by a finite sum, $\frac{1}{V_{BZ}} \int \rightarrow \sum_{\mathbf{k}} w_{\mathbf{k}}$, where $w_{\mathbf{k}}$ are appropriate weights. Effective methods has been devised to construct special $\mathbf{k}$-point sets [36] for the approximated Brillouin zone integration. Supercells are always applied in the DACAPO, SIESTA and GPAW program for this work. However, GPAW may also use vanishing boundary conditions.

2.5.2 Description of the ions

Solving the non-interacting KS-equations is a much more manageable task than solving for the many-body Hamiltonian directly. However, the KS-equation still poses substantial numerical difficulties: (i) In the the atomic region near the nucleus the kinetic energy of the electrons is large and the wave functions oscillate rapidly so that a very fine grid is required for an accurate numerical representation. The large kinetic energy makes the KS-equations stiff in the sense that a change in the chemical environment will only have a small effect on the shape of the wave functions in the atomic-region. This suggests that the wave-function in the atomic-region can be well represented by a small basis set. (ii) In the bonding region between atoms the situation is reversed. The kinetic energy is small and the wave-functions are smooth. The latter thus respond strongly to a change in the environment, which in turn requires a large and flexible basis set.

The combination of the two requirements (i) and (ii) is a non-trivial task, and different strategies have been developed which may broadly be divided into three groups.

Atomic like orbitals have traditionally been most appealing to quantum chemists. The wave function is well represented in the atomic region by a few atomic like orbitals, and the bonding is then to be described by the overlapping tails.

Pseudopotentials aim at representing the bonding part of the wave function between the atoms in an numerically accurate way. To this end, it is exploited that bonding to a large extent is determined by the outermost valence electrons of the individual atoms. Consequently, the chemically inert core electrons are assumed to be frozen in the atomic core states, and are in turn neglected in the self-consistent solution of the KS problem. This leads to a major reduction in the number of wave functions which must be handled. However, the remaining wave functions are still required to be orthogonal to the core states, which introduces rapid oscillations in the atomic region. In order to use a coarse grid to accurately represent the valence wave functions, the strong field from the nucleus is replaced by a softer pseudopotential.

Augmented wave methods use a composed basis of the localized atom like basis functions in the atomic region and a set of so-called envelope functions in the interfacial region appropriate for describing the bonding between the atoms.

A general and in principle exact framework, for which the pseudopotential method may be seen as an approximations, is offered by the projector augmented wave method (PAW) [37, 38]. The PAW method is based on the simple principle of a defining a linear transformation τ from smooth easily numerical representable wave functions $\{\tilde{\phi}_n\}$ to the exact KS all electron wave functions $\{\phi_n\}$

$$\psi_n = \tau \tilde{\psi}_n, \tag{2.14}$$

where the operator τ has to modify the smooth pseudowave function in each atomic region so that the resulting wave function has the correct all electron nodal structure. The general form of a pseudopotential for ion a follows directly from the PAW formalism. It may be written as [38]

$$v_{NL}^a = v^a(r) + \sum_{ij} |\beta_i^a\rangle V_{ij}^a \langle \beta_j^a|, \tag{2.15}$$

where $v^a(r)$ is a local part and $\{\beta_i(r)\}$ are projector functions localized in the core region. If the pseudopotentials are constructred such that the integrated charge of the pseudo wave functions is equal to the all electron wave function in the atomic (core), they are refered to as norm-conserving. For some elements, such as Ni and O, the high amplitude of the valence state around the nucleus are still retained in norm-conversing pseudopotentials and in return an accurate

description of the atomic region is still required. However, relaxing the constraint of norm-conservation may alleviate this problem as was first shown by Vanderbilt [7]. The resulting pseudopotentials are termed ultrasoft. In return for an improved smoothness in the atomic region, the pseudo wave functions $\{\tilde{\psi}_n\}$ now satisfy a generalized orthonormality relation $\langle\tilde{\psi}_n|S|\tilde{\psi}_m\rangle = \delta_{nm}$, where $S = 1 + \sum_{ija} |\beta_i^a\rangle Q_{ij}^a \langle beta_i^a|$ is a generalized overlap operator [7]. It is related to the linear transformation in PAW by $S = \tau^\dagger \tau$ [37].

In this work both ultrasoft and normconserving pseudopotentials have been used.

Chapter 3

Quantum Electron Transport

This chapter provides an introduction to the basic theoretical concepts and framework concerning the conductance from contacts of mesoscopic size to junctions consisting of a only a single atom or molecule.

3.1   Calculating the current

This section begins with a description of a rather general framework to describe the flow of electrons from one electron reservoir through a quantum conductor and into a second reservoir. The introduction of nonequilibrium Green's function may then lead to a compact expression for the calculating the current.

To this end, we introduce a model where a quantum conductor (C) is connected to a left (L) and right (R) lead. For time $t < t_0$ we consider the three regions to be disconnected, each being in local equilibrium with the chemical potentials μ_L, μ_C and μ_R as shown schematically in Fig. 3.1. The three systems are connected at time $t = t_0$ and electrons will start to flow from the lead with higher chemical potential through the conductor and into the lead with a lower chemical potential. The initial discharge from one lead will give a transient current. However, in this work we shall only be concerned with the steady state current.

We now introduce an orthonormal set of orbitals $\{\phi_i\}$ and the single particle Hilbert space $\mathcal{H}$ spanned by $\{\phi_i\}$. To limit the technical details, in this section the discussion of the general case of a non-orthogonal basis is postponed to the description of the implementation using DFT in Sec. 4.1.

The orbitals ϕ_i are assumed to be localized in such a way that $\mathcal{H}$ may be decomposed into three orthogonal subspaces $\mathcal{H} = \mathcal{H}_\mathcal{L} + \mathcal{H}_\mathcal{C} + \mathcal{H}_\mathcal{R}$, where each subspace is associated with one of the three subsystems L, C and R, respectively.

The noninteracting part of the Hamiltonian for the three *connected* regions is

Before coupling
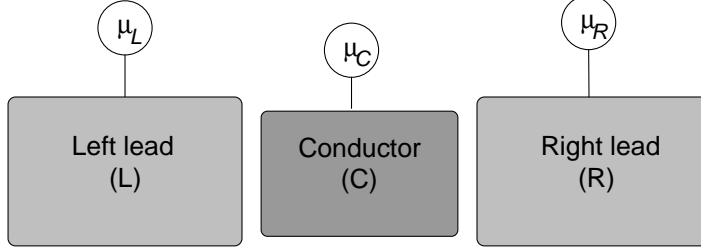
After coupling
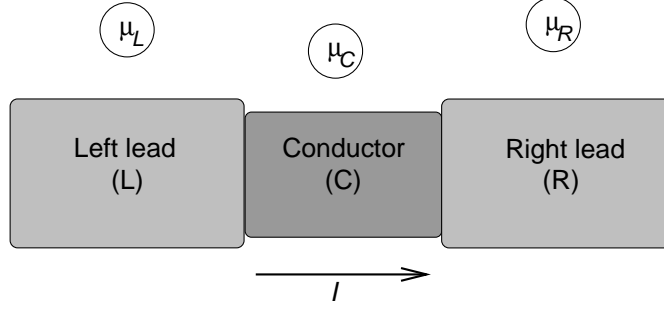
Figure 3.1: The subsystems are held in thermodynamic equilibrium at, in general, tree different chemical potentials μ_L, μ_C, and μ_R. After coupling is made electrons will discharge from the lead with highest chemical potential through the central conductor and into the other lead.

written as

$$\hat{h} = \sum_{i,j,\sigma} h_{ij} c_{i\sigma}^{\dagger} c_{j\sigma}, \tag{3.1}$$

where the sum is over basis functions for the entire system. To describe the system before connection is made we introduce

$$\hat{h_0} = \hat{h}_{LL} + \hat{h}_{CC} + \hat{h}_{RR}, \tag{3.2}$$

where $\hat{h}_{\alpha\alpha}$ is obtained by restricting i, j to $\alpha \in L, C, R$. To allow for two-body interactions in the central region the interacting part of the Hamiltonian is denoted by $\hat{V}$ and the full Hamiltonian describing the system may be written as

$$\hat{H}(t) = \left\{ \begin{array}{ll} \hat{H}_0 = \hat{h}_0 + \hat{V} & , t < t_0 \\ \hat{H} = \hat{h} + \hat{V} & , t \geq t_0. \end{array} \right. \tag{3.3}$$

Before the connection is made, all three subsystems are in local thermal equilibrium and are described by their respective equilibrium state operator. For the central region it is

$$\rho_C = \frac{1}{Z_C} e^{-\beta(\hat{h}_{CC} + \hat{V} - \mu_\alpha)}, \tag{3.4}$$

where Z_C is the partition function and $beta = k_B T^{-1}$, where k_B is Boltzmann's constant and T is the temperature. The state operators for lead α may be obtained by replacing C with α and removing $\hat{V}$, since two-body interactions are only included in C. The state of the decoupled system is $\hat{\rho} = \hat{\rho}_L \hat{\rho}_C \hat{\rho}_R$ and the time evolution of ρ at times $t \geq t_0$ is

$$\hat{\rho}(t) = \hat{U}(t)\hat{\rho}\hat{U}^\dagger(t), t \geq t_0, \tag{3.5}$$

where $\hat{U}(t)$ is the solution of $i\partial_t \hat{U}(t) = \hat{H}(t)\hat{U}(t)$. By using the equation of motion technique for $\rho(\hat{t})$ the Kubo formula can be derived, which in turn may be used to calculate the linear-response conductance [39]. In this work a different approach is taken, where the current is calculated in terms of single particle nonequlibrium Green's functions [40]. This is a method explored by Meir and Wingreen [41].

The particle current from lead α may be calculated as the time derivative of the expectation value of the lead α number operator

$$\begin{aligned} I_\alpha(t) &= -i\langle [H, N_\alpha] \rangle_0 \tag{3.6} \\ &= i \sum_{i_\alpha, j_c} h_{i_\alpha, j_c} \langle c_{i_\alpha}^\dagger(t) c_{j_c}(t) \rangle_0 - h_{i_\alpha, j_c}^* \langle c_{j_c}^\dagger(t) c_{i_\alpha}(t) \rangle_0, \tag{3.7} \end{aligned}$$

where i_α and j_c refers to basis functions in lead α and the central region, respectively. The matrix elements $h_{i_\alpha, j_c} = \langle \phi_{i_\alpha} | \hat{h} | \phi_{j_c} \rangle$ describes the coupling between lead α and the central region. Time evolution in Eq. 3.6 is governed by the full Hamiltonian, while the expectation values are with respect to ρ_0, hence the subscript 0. The lesser Green's function is defined by $G_{i_\alpha, jC}^<(t, t') = i\langle c_{i_\alpha}^\dagger(t) c_{jC}(t') \rangle_0$ and thus the two terms in Eq. (3.6) can be recognized as the equal time lesser Green's function. The machinery of nonequilibrium Green's functions [42] may at this point be applied to obtain expressions for the lesser Green's functions. This results in the compact expression for the particle current from lead α

$$I_\alpha = \int \frac{d\varepsilon}{2\pi} \text{Tr}[\mathbf{\Sigma}_\alpha^< \mathbf{G}_C^> - \mathbf{\Sigma}_\alpha^> \mathbf{G}_C^<], \tag{3.8}$$

where the trace is over central region basis functions and the bold face indicate matrices. In the next section explicit expressions for the self-energies and Green's functions will be given for the case of non-interacting electrons.

3.2   Phase-coherent transport

For non-interacting electrons the self-energy for the central region GF is only composed of lead contributions, $\Sigma = \Sigma_L + \Sigma_R$. Furthermore the lesser and greater GF now take a particular simple form [42]

$$
\begin{aligned}
\mathbf{G}_C^<(\varepsilon) &= \mathbf{G}_C^r(\varepsilon)[f_L(\varepsilon)\mathbf{\Gamma}_L + f_R(\varepsilon)\mathbf{\Gamma}_R]\mathbf{G}_C^a(\varepsilon), & (3.9) \\
\mathbf{G}_C^>(\varepsilon) &= \mathbf{G}_C^r(\varepsilon)[(f_L(\varepsilon)-1)\mathbf{\Gamma}_L + (f_R(\varepsilon)-1)\mathbf{\Gamma}_R]\mathbf{G}_C^a(\varepsilon), & (3.10)
\end{aligned}
$$

where $f_\alpha(\varepsilon)$ is the Fermi function of lead α and $\mathbf{\Gamma}_\alpha$ is given by

$$\mathbf{\Gamma}_\alpha = i(\mathbf{\Sigma}_\alpha^r - \mathbf{\Sigma}_\alpha^a). \tag{3.11}$$

Inserting these expressions into the current formula (3.8) $I = (I_L - I_R)/2$ leads to the simple expression

$$I = \frac{2e^2}{h} \int (f_L(\varepsilon) - f_R(\varepsilon))T(\varepsilon)d\varepsilon, \tag{3.12}$$

where the transmission function is defined by

$$T(\varepsilon) = \text{Tr}\big[\mathbf{G}_S^r(\varepsilon)\mathbf{\Gamma}_L(\varepsilon)\mathbf{G}_S^a(\varepsilon)\mathbf{\Gamma}_R(\varepsilon)\big]. \tag{3.13}$$

Note units have been introduced in Eq. (3.12). In this work we shall only be concerned with the low bias and low temperature for which the conductance $G = I/V$ becomes

$$G = G_0 T(\varepsilon_F), \tag{3.14}$$

where the quantum conductance unit is given by $G_0 = 2e^2/h$. The transmission coefficient matrix, $\mathbf{t}(\varepsilon)$, as defined within Landauer-Büttiker theory, is related to the GFs by $\mathbf{t}(\varepsilon) = [\mathbf{\Gamma}_R(\varepsilon)]^{1/2} \mathbf{G}_S^R(\varepsilon) [\mathbf{\Gamma}_L(\varepsilon)]^{1/2}$, showing the equivalence of Eq. (3.14) to the Landauer formula [43].

Finally, we mention that phase-coherent transport refers to the situation where electrons are behaving as weakly interacting quasi-particles with a life

time greater than the time it takes the electrons to traverse the central scattering region. The central region Hamiltonian may then be approximated with an effective single particle Hamiltonian leading to the simplified conductance formula in Eq. (3.13)

3.3 Transport through a single level

To illustrate and develop a physical understanding of the general formalism developed above, transport through a single level contacted to a left and right lead is considered. As we shall see later in this work, this model is well-suited for analyzing the electron transport properties of more complicated molecular junctions. For a more detailed description of the model we refer to Paper I and VI.

We consider the Newns Anderson model [44] and introduce a single molecular state ϕ_c associated with the central region subspace $\mathcal{H}_C$ and an orthonormal basis $\phi_{\alpha i}$ associated with the α lead subspace $\mathcal{H}_\alpha$. The molecular state is coupled to infinite leads via $t_{\alpha i} = \langle \phi_c | H | \phi_{\alpha i} \rangle$. The GF for the molecular state is

$$G_c(\varepsilon) = \frac{1}{\varepsilon - \varepsilon_c - \Sigma_L(\varepsilon) - \Sigma_R(\varepsilon)}, \tag{3.15}$$

and the α lead self-energy is given by

$$\Sigma_c(\omega) = \sum_{ij} t_{\alpha i} (g_\alpha^0)_{ij} t_{\alpha j}^*. \tag{3.16}$$

A particularly elegant representation is obtained by introducing the group orbital of lead α as

$$\gamma_\alpha = \frac{1}{V_\alpha} \sum_i t_{\alpha i} \phi_{\alpha i}, \tag{3.17}$$

where the normalization factor $V_\alpha = (\sum_i |t_{\alpha i}|^2)^{1/2}$. The group orbital is a linear combination of α lead basis functions with the weights given by the coupling strength. The group orbital may therefore be expected to be localized near the molecular state at on the level-lead interface. It can be shown that the coupling between $|\phi_c\rangle$ and any state in the lead orthogonal to $|\gamma_\alpha\rangle$ is zero. Using this shows that the molecular state is only coupled to the lead via the group orbital. The relations between the diagonal elements of the Green's functions and the projected density of states ($\rho = -\pi^{-1} \mathrm{Im}[G_{ii}]$) it may be shown that in the case of a symmetric coupling the transmission function in (3.13) takes the simple form

$$T(\varepsilon) = 2\pi^2 |V|^2 \rho_c(\varepsilon) \rho_\gamma^0(\varepsilon). \tag{3.18}$$

In the case of strong asymmetric coupling where R is the "weak" side such that $V_L >> V_R$ we obtain

$$T(\varepsilon) = 4\pi^2 |V|^2 \rho_c(\varepsilon) \rho_\gamma^0(\varepsilon), \tag{3.19}$$

The later two equations are particular appealing. The first says that the transmission is determined by three parameters: The level density of states ρ_c, the coupling strength $V = (V_L = V_R)$ and the density of states of the group orbital ρ_γ^0 for the isolated leads, i.e. without the coupling V. The second says the transmission is determined by the same quantities, but now the lead quantities only refers to the weakly coupled side. This is reminiscent of scanning tunneling microscopy theory, where the current is determined by the density of states of the surface being scanned, i.e. the "weak side".

3.4   Transport through a chain

The single level method developed above may also be applied to bulk-chain-bulk systems, such as the one shown in Fig. 3.2. However, this requires both the transmission resonance overlaps and interference effects between the levels are small. In order to overcome these restrictions we introduce a simple resonating-chain model. The model is particular well suited to study transport in not only atomic chains but in general systems where a periodic potential is sandwiched between two electrodes and has been applied in the study of nanotubes [45, 46]. In fact the model is exact for coherent transport for chains above a certain chain length. The model is based on the Landauer Büttiker formalism for conductance [47, 48, 49] where scattering states, instead of Green's function is the central object. Scattering states are the eigenstates of the open system imposed with scattering boundary conditions. In the following we will consider eigen-channel states, which are a obtained by the unitary rotation of the scattering states that diagonalized the transmission probability amplitude matrix **t** [50].

Now, consider an electron approaching the chain from the left lead. It will have a certain transmission probability T_1 for entering into the chain. Inside the chain the electron can propagate back and forth between the two (identical) contacts, so that every time the electron impinges on one of the contacts it is reflected with a probability $R_1 = 1 - T_1$ and it furthermore picks up a phase shift $\phi_1 = \arg(r)$, see Fig. 3.2. We furthermore assume that the electron in the infinite chain is characterized by a single Fermi Block wave vector **k**. The interference between all the reflected waves then leads to a total transmission probability T through the chain system of
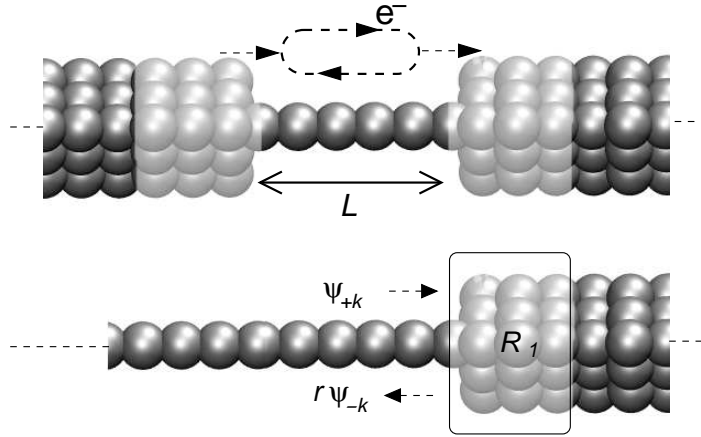
Figure 3.2: The resonating-chain model for a chain of length L. The parameters describing the resonant transport is extracted from a chain-bulk contact.

$$T = \frac{1}{1 + 4\frac{R_1}{(1-R_1)^2}\sin^2(kL + \phi_1)} \qquad (3.20)$$

where L denotes the distance between the two contacts. This expression is exact for coherent transmission in the limit where the reflections at the two ends can be considered independent, i.e. it is required that the potential in the central part of the chain is unaffected by the two contacts. It should be noted that there is a certain arbitrariness in the definition of the distance L between the two contacts, however, different choices for L also gives different results for the phase shift ϕ_1 [51] so that Eq. 3.20 still holds.

Chapter 4

Conductance Calculations

The purpose of this chapter is to provide details of how the general transport formalism described in chapter 3 can be combined with Kohh-Sham density functional theory to give a fully atomistic description of phase-coherent electron transport in nano-structures.

A number of different first principles methods have been developed to describe the phase-coherent transport properties of realistic atomic-sized junctions. Most of these methods are based on either a direct calculation of the scattering wave-functions or a calculation of the single-particle Green's function. The method in the present work is based on the latter which provides a numerically efficient scheme. Further, this method may be extended to include other interactions , such as electron-electron and electron-phonon interactions. On the other hand, scattering states can sometimes provide an alternative and useful view of the electron transport properties of a nano-junction. However, it was recently shown that one may calculate scattering states efficiently and directly from central region single-particle Green's functions [52]. Thus combining the advantages of both approaches. An application of this approach can be found in Paper V.

Although the Kohn-Sham Hamiltonian may provide the exact electron density, there is no obvious reason why it should also give the correct current. Moreover, it is not easy to estimate the effect of using approximate xc-functionals such as the LDA or GGA. We mention here that more sophisticated methods for quantum transport based on configuration interaction, the GW method, time-dependent DFT, and the Kubo formula have recently been proposed [53, 54, 55, 56, 57]. However, these schemes are very computationally demanding when compared to the method presented in this chapter. Further, these schemesare no a realistic choice for atomistic nanojunctions. Besides this more fundamental

issue concerning Kohn-Sham DFT for transport, a number of numerical approximations involved in actual implementations. These include choice of exchange-correlation potential, pseudopotentials, basis functions and boundary conditions.

This chapter is organized as follows: First the general setup for phase coherent transport is described, providing a more technical discussion of the formalism introduced in the preceding chapter. This is followed by a discussion of the boundary conditions, i.e. how to go from a supercell with periodic boundary conditions in all directions, to a system with open boundary conditions in the transport direction. In particular, the choices made in the method implemented in this work are discussed. Finally, the basis sets applied are briefly discussed, together with their respective advantages and disadvantages in connection with the methods used to perform conductance calculation in this work.

4.1   General setup

The conductance formula given in Eq. 3.13,

$$G = G_0 \mathrm{Tr}[\boldsymbol{G}_C^r \boldsymbol{\Gamma}_L \boldsymbol{G}_C^a \boldsymbol{\Gamma}_R], \tag{4.1}$$

constitute the starting point for numerical calculations. This is valid for non-interacting electrons moving phase-coherently trough a central conductor region (C) connected to a left (L) and right (R) lead. We make the additional assumption that the potential in the leads are periodic with the underlying lattice in the transport direction. In return, a very efficient computational scheme can be developed. The KS-Hamiltonian defining our system is given by

$$H = -\frac{1}{2}\nabla^2 + v_s(\mathbf{r}) + V_{\mathrm{NL}}, \tag{4.2}$$

where v_s is the local part of the effective potential and V_{NL} is the non local part associated with the pseudopotential. The Hamiltonian in terms of a basis set $\{\phi_i\}$ with the desired property of being localized in the transport direction, takes the (matrix) form

$$\boldsymbol{H} = \begin{pmatrix} \boldsymbol{H}_L & \boldsymbol{H}_{CL}^\dagger & 0 \\ \boldsymbol{H}_{CL} & \boldsymbol{H}_S & \boldsymbol{H}_{CR} \\ 0 & \boldsymbol{H}_{CR}^\dagger & \boldsymbol{H}_R \end{pmatrix}, \tag{4.3}$$

where the zeros reflect the vanishing coupling between the leads. In order to deal with nonorthogonal basis functions, we introduce the overlap matrix $\boldsymbol{S}_{ij} = \langle \phi_i | \phi_j \rangle$.

The transmission function is to be determined from the Green's functions (GFs) in the presence of the leads. The retarded GF matrix for the entire system is defined by

$$(z\boldsymbol{S} - \boldsymbol{H})\boldsymbol{G}^r(\varepsilon) = \boldsymbol{I}, \tag{4.4}$$

where $z = \varepsilon + i0^+$. It is important to recognize that $\boldsymbol{G}^r$ differs from $\langle\phi_i|(z\hat{S} - \hat{H})^{-1}|\phi_j\rangle$. In fact, $\boldsymbol{G}^r$ corresponds to $(z\hat{S} - \hat{H})^{-1}$ in the dual basis, and the two are related by

$$\langle\phi_i|(z\hat{S} - \hat{H})^{-1}|\phi_j\rangle = [\boldsymbol{S}\boldsymbol{G}^r(\varepsilon)\boldsymbol{S}]_{ij}. \tag{4.5}$$

The division into three regions (L), (C) and (R) can be used to write Eq. (4.4) explicit as

$$\begin{pmatrix} z\boldsymbol{S}_L - \boldsymbol{H}_L & z\boldsymbol{S}_{CL}^\dagger - \boldsymbol{H}_{CL}^\dagger & 0 \\ z\boldsymbol{S}_{CL} - \boldsymbol{H}_{CL} & z\boldsymbol{S}_C - \boldsymbol{H}_C & z\boldsymbol{S}_{CR} - \boldsymbol{H}_{CR} \\ 0 & z\boldsymbol{S}_{CR}^\dagger - \boldsymbol{H}_{CR}^\dagger & z\boldsymbol{S}_R - \boldsymbol{H}_R \end{pmatrix} \times$$
$$\begin{pmatrix} \boldsymbol{G}_L^r & \boldsymbol{G}_{LC}^r & \boldsymbol{G}_{LR}^r \\ \boldsymbol{G}_{CL}^r & \boldsymbol{G}_C^r & \boldsymbol{G}_{CR}^r \\ \boldsymbol{G}_{RL}^r & \boldsymbol{G}_{RC}^r & \boldsymbol{G}_R^r \end{pmatrix} = \begin{pmatrix} \boldsymbol{I}_L & 0 & 0 \\ 0 & \boldsymbol{I}_C & 0 \\ 0 & 0 & \boldsymbol{I}_R \end{pmatrix}, \tag{4.6}$$

The GFs of the central region are determined by the matrix equations

$$\boldsymbol{G}_C^r(\varepsilon) = (z\boldsymbol{S}_C - \boldsymbol{H}_C - \boldsymbol{\Sigma}_L^r(\varepsilon) - \boldsymbol{\Sigma}_R^r(\varepsilon))^{-1}, \tag{4.7a}$$

$$\boldsymbol{\Sigma}_\alpha^r(\varepsilon) = (z\boldsymbol{S}_{C\alpha} - \boldsymbol{H}_{C\alpha})\,\boldsymbol{g}_\alpha^{0,r}(\varepsilon)(z\boldsymbol{S}_{C\alpha}^\dagger - \boldsymbol{H}_{C\alpha}^\dagger) \tag{4.7b}$$

$$\boldsymbol{g}_\alpha^{0,r}(\varepsilon) = (z\boldsymbol{S}_\alpha - \boldsymbol{H}_\alpha)^{-1}, \tag{4.7c}$$

where $\boldsymbol{\Sigma}_\alpha^r$ is the self energy of the α lead, $\boldsymbol{g}_\alpha^{0,r}$ is the uncoupled lead GFs.

4.2 Coupling to leads

The important quantity to calculate in order to obtain the self energy in Eq. 4.7b is the uncoupled α lead Green's function $\boldsymbol{g}_\alpha^{0,r}$. The assumption of a periodic potential in the leads means that they may be divided into principal layers containing an integer number of potential periods. The localization of the functions in the transport direction allows us to choose a principal layer size such that only nearest neighboring layers will couple. This allows us to write the Hamiltonian in the block-tridiagonal form

$$\boldsymbol{H}_L = \begin{pmatrix} \ddots & \vdots & \vdots & \vdots \\ \dots & \boldsymbol{h}_0 & \boldsymbol{h}_1 & 0 \\ \dots & \boldsymbol{h}_1^\dagger & \boldsymbol{h}_0 & \boldsymbol{h}_1 \\ \dots & 0 & \boldsymbol{h}_1^\dagger & \boldsymbol{h}_0 \end{pmatrix} \tag{4.8}$$

where $\boldsymbol{h}_0$ is the Hamiltonian matrix within a single layer and $\boldsymbol{h}_1$ is the nearest neighbor layer coupling. The assumption of a periodic lead can in principle always be fulfilled by enlarging the central region until all perturbations are screened. In practice the mobile metal electrons screen such perturbations effectively and the potential converges to its bulk value after a few atomic layers. The devision of the leads into principal layers with nearest neighbor coupling implies that the central region only couples to the first principal layer. Also from the form of Eq. (4.7b), it follows that only the lead Green's function of the first layer is needed, the so-called surface Green's function, to obtain the self-energy. Due to the periodic nature of the leads the surface Green's function can be calculated iteratively using a particularly efficient scheme known as the decimation technique [58]. However, it could also be calculated using a "simple" iterative scheme, starting from some initial surface Green's function. This has the advantage of not being restricted to periodic leads. In fact, combining a simple iterative scheme with an initial surface Green's function, calculated using the decimation technique results in a linear scaling algorithm for calculating the conductance.

4.3   Boundary conditions

In this section we describe the transport formalism resulting from calculations using supercells with periodic boundary conditions. The DFT calculation for the supercell modeling the central region is performed with periodic boundary conditions in all directions. In order to "open up" the system the potential, at the end planes perpendicular to the transport direction of the supercell should be extended by appropriate semi-infinite lead potentials. In the case where the localized basis set is fixed, i.e. atomic orbitals, we choose the lead potential extension with in the following way. First, periodic boundary conditions in the transport direction are removed by setting all coupling matrix elements in the Hamiltonian and overlap matrix to zero if the basis function centers are are more than $L/2$ away. Here, L is the length of the supercell in the transport direction. Second, because the KS potential to the left and right of C as by definition converged to the value in the leads, we may take the coupling between central

region and lead α, $H_{C\alpha}$, from the infinite lead calculation. In practice the intra-lead coupling matrix elements $(H_{\alpha\alpha})$ in $H_{C\alpha}$, can be controlled by including a larger portion of the lead in C. In practice we find that 3-4 atomic layers must be included in C on both sides of the junction to obtain converged conductances.

Since the scattering region of the system is still periodic in the transverse direction, all matrices entering the transmission formula Eq. 4.1 are infinite in size. However, the periodicity from the use of a supercell implies the wave vector $\mathbf{k}_\perp$ of the first Brillouin zone (BZ) of the transverse supercell gives good quantum numbers. All matrices are therefore diagonal with respect to $\mathbf{k}_\perp$. The total transmission function can thus be decomposed into transverse wave vector dependent transmissions

$$T(\mathbf{k}_\perp; \varepsilon) = \mathrm{Tr}\left[\boldsymbol{G}_S^r(\mathbf{k}_\perp; \varepsilon)\boldsymbol{\Gamma}_L(\mathbf{k}_\perp; \varepsilon)\boldsymbol{G}_S^a(\mathbf{k}_\perp; \varepsilon)\boldsymbol{\Gamma}_R(\mathbf{k}_\perp; \varepsilon)\right]. \qquad (4.9)$$

Consequently, the transmission per supercell is to be evaluated over an integral of the two dimensional transverse or surface BZ

$$T(\varepsilon) = \frac{1}{A} \int d\mathbf{k}_\perp T(\mathbf{k}_\perp), \qquad (4.10)$$

where A is the area of the first transverse supercell BZ. However, in practice the integral is approximated by a finite sum: $T(\varepsilon) = \sum_{\mathbf{k}_\perp} w_{\mathbf{k}_\perp} T(\mathbf{k}_\perp)$, where $w_{\mathbf{k}_\perp}$ are symmetry determined weight factors which add up to 1. The importance of sufficiently large number of $\mathbf{k}_\perp$ is illustrated in Paper II and a more detailed discussion can be found in Ref. [59].

4.4 Basis set

The conductance calculations and transport analysis presented in this work have all been performed using one of two type of basis sets, (i) Pseudo atomic orbitals (PAO) [60, 61] or (ii) Wannier functions (WFs) [9, 8].

Neither the PAO nor the WFs can be directly used as basis functions, since they are not associated with a specific wave vector in the first BZ of the transverse plane. Thus they do not comply with the periodic boundary conditions used in these directions. In this section it is explained how appropriate Bloch-like basis functions can be constructed from localized functions. The various advantages and drawbacks associated with each of the two types of basis sets used in relation to conductance calculations are also discussed.

The imposed periodic boundary conditions in the surface plane directions means that we are in fact considering the conductance of a periodic array of

junctions instead of a single junction. Instead of the localized basis functions $\phi_n(\mathbf{r})$ (these could be a WF or a PAO) we consider the Bloch function

$$\chi_{n\mathbf{k}_\perp} = \frac{1}{\sqrt{N_{R_\perp}}} \sum_{\mathbf{R}_\perp} e^{i\mathbf{k}_\perp \cdot \mathbf{R}_\perp} \phi_n(\mathbf{r} - \mathbf{R}_\perp), \qquad (4.11)$$

where $\mathbf{R}_\perp$ runs over supercells in the surface plane and $\mathbf{k}_\perp$ is a wave-vector in the corresponding two-dimensional BZ. Since $\mathbf{k}_\perp$ gives a good quantum number, we can construct the Hamiltonian, $H(\mathbf{k}_\perp)$ and overlap matrix $S(\mathbf{k}_\perp)$ for each $\mathbf{k}$-point separately.

4.4.1   Pseudo atomic orbitals basis

The use of pseudo atomic orbitals in DFT calculations was introduced by Sankey and co-workers [60] and is also the "standard" basis set used in the SIESTA-code citesiesta and the conductance calculations based on PAO in this work. The PAO are defined as the product of a numerical radial function and a spherical harmonic

$$\phi_{lmn}(\mathbf{r}) = r(r)_{ln} Y_{lm}. \qquad (4.12)$$

Orbitals with the same angular dependence, but different radial dependence is refered to as a multiple-ζ basis. In order to accurately account for deformation induced by bond formation so-called polarization functions is often required. These can be generated by applying a small constant electric field [3, 61]. The PAO are excited orbitals of a free atom as described by a pseudopotential, and are obtained by requiring the orbital to be zero at a certain radial cutoff. This augments the pseudo potential with a certain confining potential, such as an infinite wall at the cutoff radius.

In order to obtain $H(\mathbf{k}_\perp)$ and $S(\mathbf{k}_\perp)$ a simple scheme has been implemented. We use SIESTA to calculate the "real space" Hamiltonian $H(\mathbf{R})$ and overlap matrix $S(\mathbf{R})$ and subsequently perform the transformation

$$H(\mathbf{k}_\perp) = \sum_R e^{i\mathbf{k}\cdot\mathbf{R}} H(\mathbf{R}), \qquad (4.13)$$

where $H(\mathbf{R})_{ij} = \langle \phi_i(r) | H | \phi_j(r - R) \rangle$. The same holds for $S(\mathbf{R})$.

4.4.2   Wannier function basis

Thygesen *et al.* introduced the expansion of partly localized Wannier functions (WFs) in terms of the M lowest lying eigenstates $\{\psi_m\}$ and L extra degrees of

freedom (EDF) $\{\phi_l\}$

$$\omega_j = \sum_{n=1}^{M} \psi_n U_{nj} + \sum_{l=1}^{L} \phi_l U_{l+M,j}, \qquad (4.14)$$

where EDF in turn are expanded in terms of the remaining $N - M$ unoccupied eigenstates

$$\phi_l = \sum_{n=1}^{N-M} \psi_{n+M} c_{nl}. \qquad (4.15)$$

The $(N - M \times L)$ matrix $\mathbf{c}$ will in general be a rectangular matrix and the transformation in Eq. 4.15 can bee viewed as "down-folding" the unoccupied space. Instead of the number of lowest lying eigenstates M it can be convenient to specify a cutoff-off energy E_0 instead, such that all states below E_0 can be reproduced exactly by the Wannier functions. In order to obtain localized functions a measure of the localization of an orbital have to be defined. Following the the work of Mazari *et al.* [24] the spread for WFs was defined as sum of local second moments

$$S = \sum_{n=1}^{N_w} (\langle \omega_n | r^2 | \omega_n \rangle - \langle \omega_n | \mathbf{r} | \omega_n \rangle^2) \qquad (4.16)$$

By varying $\mathbf{U}$ and $\mathbf{c}$, the spread S may be be minimized, and leads to localized functions. For more details and the extension to periodic systems we refer to Ref. [8, 62]. A detailed discussion of the construction of basis functions and Hamiltonian matrices can be found in Ref. [63].

4.5 Two methods

In this section, we describe the two specific nonequilibrium (NEGF)-DFT implementations applied in the present work and their key parameters are discussed. Also the advantages and disadvantages of the two methods is discussed.

4.5.1 Method 1: Wannier functions from plane-wave DFT

In method 1 the Kohn-Sham Hamiltonian is obtained from an accurate plane-wave pseudopotential DFT code [2]. The ion cores are replaced by ultrasoft pseudopotentials [7] and we use an energy cutoff of 25 Ry for the plane wave expansion. The Kohn-Sham eigenstates are transformed into partly occupied Wannier functions (WFs) [8] which are used to obtain a tight-binding like representation of the Hamiltonian. The WFs are constructed such that any eigenstate

below a selected energy, E_0, can be exactly represented by a linear combination of WFs. In the applications we have chosen, E_0 is in the range of 2-4 eV above the Fermi level. In this way the accuracy of the plane-wave calculation is carried over to the WF basis for all energies relevant for transport.

After performing separate DFT calculations for the (periodic) leads and the central region C we obtain a set of WFs for each region. Note, that C always contains a few buffer layers of the lead material on both sides of the nano-contact to ensure that the KS potential at the end planes of C has converged to its value in the leads. Since the WFs in the lead will in general differ from those in the outermost lead unit cells of the central region, care must be taken to evaluate the coupling and overlap matrices $H_{C\alpha}$ and $S_{C\alpha}$. Also note that although the WFs by construction are orthogonal within each region, WFs belonging to different regions will in general be non-orthogonal. For more details on the construction of the WFs and the calculations of the Hamiltonian matrix for the combined $L - C - R$ system we refer to Ref. [63]. Here, we shall refer to the results obtained from method 1 as the WF results.

The main advantages of method 1 are: (i) The accuracy of the plane wave calculation carries over to the WF basis set. (ii) The WFs basis set is truly minimal and often results in even fewer basis functions than a single zeta basis. The WF basis thus combines high accuracy with high efficiency. The price one has to pay is that the actual construction of well localized WFs is not always straightforward, and requires some user interaction, particularly for metallic systems. Also the lack of finite support of the WFs is unwanted in the context of transport, although in practice it is not a serious problem since the WFs are well localized. Finally, as already explained above, the risk of obtaining different WFs for two similar but non-identical systems renders it less straightforward to patch the parts together using Hamiltonians obtained from the separate calculations.

4.5.2   Method 2: PAO Siesta basis

Method 2 is based on the DFT code Siesta [3] which uses finite range pseudoatomic orbitals (PAO) [60, 61] as basis functions and Troullier-Martins norm conserving pseudopotentials [64]. As in method 1, the Hamiltonians for the leads and the central region are obtained from separate calculations. Because the KS potential to the left and right of C, by definition has converged to the value in the leads, we can take the coupling between central region and lead α, $H_{C\alpha}$, from the pure lead calculation. Note that this is in contrast to method 1, where the different shape of the WFs in the periodic lead and the lead part of the central region makes it essential to evaluate the coupling matrix directly. Note also that this approximation, i.e. the use of the intra-lead coupling matrix

elements ($H_{\alpha\alpha}$) in $H_{C\alpha}$, can be controlled by including a larger portion of the lead in C. In practice we find that 3-4 atomic layers must be included in C on both sides of the junction to obtain converged conductances.

We take the Fermi level of the bulk lead as the common Fermi level of the combined system by shifting the levels in the central region by a constant. This is done by adding to H_C the matrix δS_c, where $\delta = [H_L]_{0,0} - [H_C]_{0,0}$ and the $(0,0)$ element corresponds to the onsite energy of a basis function located near the interface between L and C.

In the present study we restrict ourselves to the standard PAOs for SIESTA: single zeta (SZ), SZ polarized (SZP) and double ZP (DZP). For the confinement energy, determining the range of the PAOs, we use 0.01 Ry and use a meshcutoff of 200 Ry, unless otherwise stated.

Most disadvantages of the WF basis are resolved by the PAO basis set. By construction they have finite support and are identical as long as the atomic species on which they are located are the same. This renders it straightforward to patch together Hamiltonians for separate subsystems as long as the KS potential can be smoothly matched at the interfaces. On the other hand, to obtain an accuracy matching the WFs results, one needs to use a significantly larger number of orbitals and thus longer computation times for the transport calculation as compared to the WF method.

Chapter 5

Benchmark calculations

First-principles calculations of electrical conductance in nano-scale contacts represents a main challenge in computational nanophysics. The interest for this type of calculations began in the mid-nineties where advances in experimental techniques made it possible to contact individual molecules thereby making it possible to study the transport of electrons through true nano-scale structures [65, 66]. Apart from the scientific interest, the development of reliable simulation tools for nano-scale quantum transport is relevant in relation to the continued miniaturization of conventional semi-conductor electronics, but also for the introduction of a new generation of molecule based electronics.

It has by now become standard to calculate conductance in nano-scale contacts by employing a combination of non-equilibrium Green's function theory (NEGF) and ground state density functional theory (DFT) as described in the preceding chapter. It has been applied extensively to a number of different systems ranging from pure metallic contacts, over organic molecules to carbon nanotubes suspended between metallic electrodes. Overall the approach has been successful in describing qualitative features and trends [67, 20], however, quantitative agreement with experiments has mainly been obtained for strongly coupled systems such as metallic point contacts, monatomic chains, as well as junctions containing small chemisorbed molecules [68, 19].

The NEGF-DFT method provided only an approximation to the true conductance - even if the exact exchange-correlation xc-functional where to be used.

Irrespective of the validity of the NEGF-DFT approach and the role played by the approximate functionals, it remains important to establish a general consensus concerning the exact result of a NEGF-DFT calculation for a given xc-functional and specified system geometry: a benchmark. Although this might seem trivial, the present situation is in fact rather unsatisfactory. A variety of

different results have been published by different groups for the same or very similar systems. As good example is provided by benzene di-thiolate trapped between gold contacts where the calculated conductance vary with up to two orders of magnitude for similar geometries [22, 21, 20, 69, 70, 71].

This chapter is organized as follows. First the main part of the work is summarized. Then three selected reference systems will be discussed in order to highlight the importance of, (i) treating the coupling between the central region and the leads in a coherent fashion, (ii) oerforming a sufficient **k**-point sampling, and finally (iii) the effect of the transverse dimensions of the supercell in comparing to cluster based transport calculations.

This chapter is a review of Paper II.

5.1   Reference systems

The main results of the benchmark study is summarized in Fig. 5.1 where we show the overall deviation

$$\Delta = \frac{1}{E_0 - E_1} \int_{\varepsilon_F + E_1}^{\varepsilon_F + E_0} |T_{\text{WF}}(\varepsilon) - T_{\text{PAO}}(\varepsilon)| \mathrm{d}\varepsilon, \qquad (5.1)$$

between the transmission functions calculated using the WF and PAO basis sets, respectively. The energy E_1 is taken as the lowest lying band edge in the lead while the cutoff energy E_0 is taken to be the energy above which the WFs are no longer able to reproduce the exact KS eigenstates of the system which is typically ~ 3 eV above the Fermi level. For all the systems we find that the deviation Δ decreases as the Siesta basis is enlarged meaning that the Siesta transmission functions converge toward the WF result. We take this as evidence for the correctness of the WF results and the justification for the use of the term *benchmark* calculation.

The next three sections will discuss will discuss the systems, Au-CO, Pt-H_2 and Au-$C_6H_4S_2$ in more detail.

5.1.1   Au chain with CO

In this section conductance properties of an infinite gold chain with a single CO molecule adsorbed is studied. Scanning tunneling microscope (STM) experiments suggest that CO strongly depresses the transport of electrons through 1d gold wires [72] supported by a Ni surface. This has been supported by NEGF-DFT calculations [73] which show that the transmission function indeed drops to zero at the Fermi level. The use of infinite gold chains as leads is clearly an
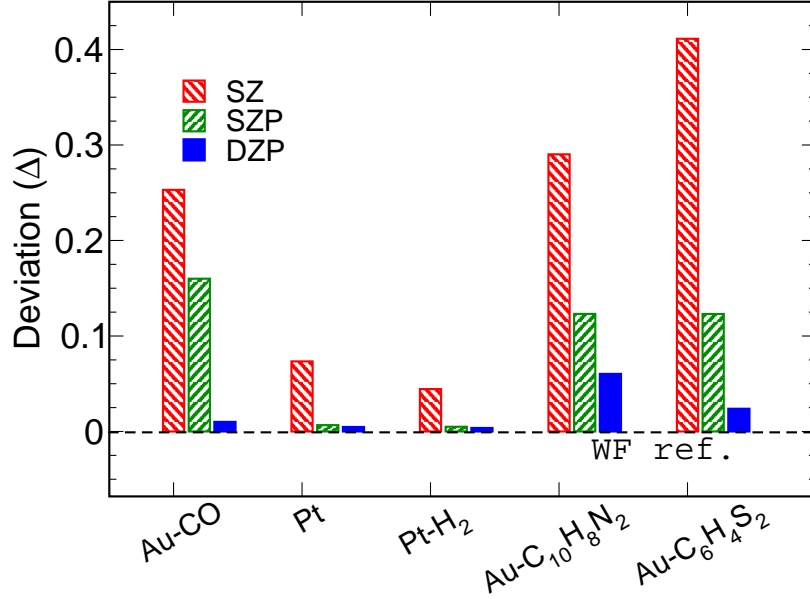
Figure 5.1: Deviation between the WF and Siesta transmission functions for for the five reference systems studied. The dashed line indicate zero deviation from the WF transmission. Notice that the Siesta results converge toward the WF result as the PAO basis is enlarged.

oversimplification of the real situation, however, the model seems to capture the essential physics, i.e. the suppression of the conductance, and furthermore is well suited as a benchmark system due to its simplicity.

The geometry of the system is shown in Fig. 5.2(a). and is is modeled using a supercell with transverse dimensions 12Å × 12Å. All bond lengths are taken from Ref. [73]: $d_{\text{Au-Au}} = 2.9$ Å, $d_{\text{Au-C}} = 1.96$ Å, and $d_{\text{C-O}} = 1.15$ Å. The Au atom holding the CO is shifted towards CO by 0.2 Å. In method 1 we obtain six WFs per Au atom and seven WFs for the CO molecular states. The WFs spans all the CO molecular states including the two degenerate LUMO's ($2\pi^*$ orbitals).

Due to the elongated bond length of the Au-wire, we found it necessary in method 2 to increase the range of the Au PAOs in order to converge the band-structure of the Au-wire. The confinement energy was therefore in this case set to 10^{-4}Ry.

In Fig. 5.2(b) the calculated transmission function using the PAO basis sets and the WF basis set is compared. Overall, the PAO result approaches the WF
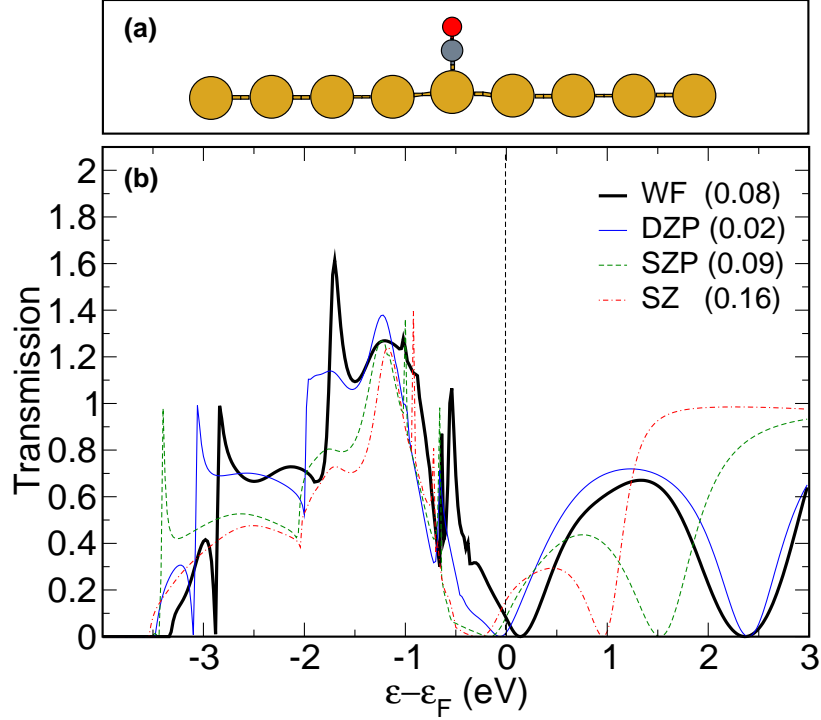
Figure 5.2: (a) Central region used to describe a single CO molecule adsorbed on a monatomic Au wire.(b) Transmission functions for the Au wire CO system calculated using method 1 (WF) and method 2 for three different PAO basis sets. The transmission function at the Fermi level is indicated in the parenthesis following the legends.

result as the basis set is enlarged. For the largest PAO basis (DZP) the agreement is in fact very satisfactory given the differences in the underlying DFT methods, e.g. ultrasoft- versus norm-conserving pseudo potentials. The remaining difference can be further reduced by a rigid shift of the DZP transmission by about 0.15 eV.

All transmission functions feature an anti-resonance near the Fermi level. However, upon enlarging the PAO basis the position of the anti-resonance shifts towards the WFs obtained postion, see table 5.1. Note that the position of the anti-resonance obtained with the WFs is approached as the PAO basis set is increased. Also, the curvature of the anti-resonance is improved as the PAO basis set is enlarged. The improvement in these features are, however, not directly reflected in the conductanses listed in table 5.1 The reason for the this apparent disagreement is clearly the rigid shift between the PAO and WF transmission

	SZ	SZP	DZP	WF
G (G_0)	0.16	0.09	0.02	0.08
ε_a (eV)	-0.27	-0.16	-0.06	0.12

Table 5.1: Conductance G and position of the anti-ressonace ε_a. The anti-resonance position with increasing PAO basis is converging towards the WFs position. The conductance does not show the same convergence since the anti-resonance position actually never crosses the Fermi level using the PAO basis.

functions.

We observe that our results differ from the calculation in Ref. [73]: While the latter finds two peaks in the energy range $0 - 2$ eV our converged transmission function shows a single broad peak. In general, both our PAO and WF based transmission functions present less structure than the transmission function reported in Ref. [73]. We suspect that these differences are related to the way the coupling $H_{\alpha C}$ is calculated in Ref. [73].

5.1.2 Pt(111)-H$_2$ contact

In this section we consider on of the simplest possible molecular junctions, namely a single hydrogen molecule between metallic Pt contacts. Like the metallic point contacts, the Pt-H$_2$-Pt junction shows stable and reproducible behavior in conductance measurements. In particular, a very pronounced peak close to $1G_0$ appears in the conductance histogram obtained when a Pt contact is broken in a hydrogen atmosphere [10]. Although reported conductance calculations show significant variation (see below), there have been given substantial evidence that the structure responsible for the peak consists of a single hydrogen molecule bridging the Pt contacts [10, 74].

Several groups have published NEGF-DFT calculations for the transmission function of the Pt-H$_2$-Pt system. Most find a conductance of $(0.9 - 1.0)G_0$ [10, 19, 75, 67], but also much lower values of $(0.2 - 0.5)G_0$ have been reported in Ref. [76].

In Fig. 5.3(a) we show the supercell used to model the scattering region of the Pt/H$_2$ contact. The Pt contact is modeled by two four-atom pyramids attached to (111) surfaces containing 3×3 atoms in the surface plane. The hydrogen molecule is in a bridge position between the two pyramid tips. The relevant bond length determining the structure after relaxation of the Pt pyramids and the hydrogen atoms are $d_{\text{Pt-H}} = 1.7$ Å and $d_{\text{H-H}} = 1.0$ Å.

In order to ensure that the effective KS potential has converged to its bulk

value at the end planes of the supercell we include 3-4 atomic layers (ABC-CABC stacking) on either side of the pyramids

In Fig. 5.3(b) we show the calculated transmission functions. The agreement between the different calculations is striking, especially in the important region around the Fermi level. The SZ basis set reproduces the qualitative features of the larger basis sets, but introduces a considerable down shift of the low-lying peaks. The conductances are summarized in Table 5.2
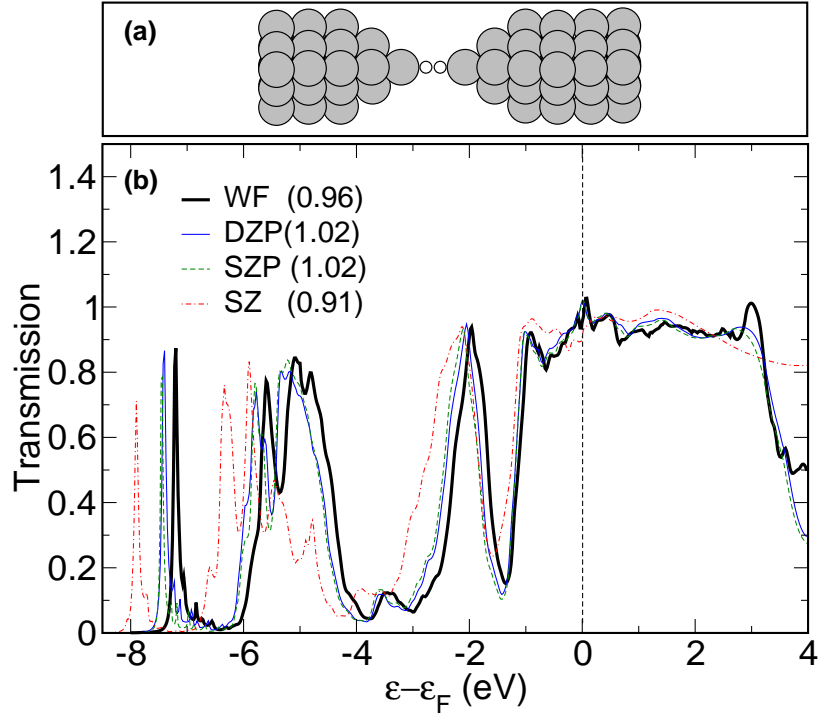

Figure 5.3: (a) Supercell used to model the central region of the $Pt - H_2 - Pt$ junction. (b) Transmission function for the Pt Hydrogen bridge. The transmission function at the Fermi level is indicated in the parenthesis following the legends.

The very good agreement between the two methods indicates that the transmission function for this system is rather insensitive to the basis set. We stress, however, that a proper $k_\perp$-point sampling of the transmission function is crucial to obtain meaningful results independently of the quality of the basis set. Restricting the calculation to the Γ point yields a transmission function with a (unphysical) peak at the Fermi level. In Fig. 5.4 we show the **k**-point dependence of the transmission function.

	SZ	SZP	DZP	WF
G (G_0)	0.91	1.02	1.02	0.96

Table 5.2: Conductance of the Pt-H_2-Pt for different basis sets
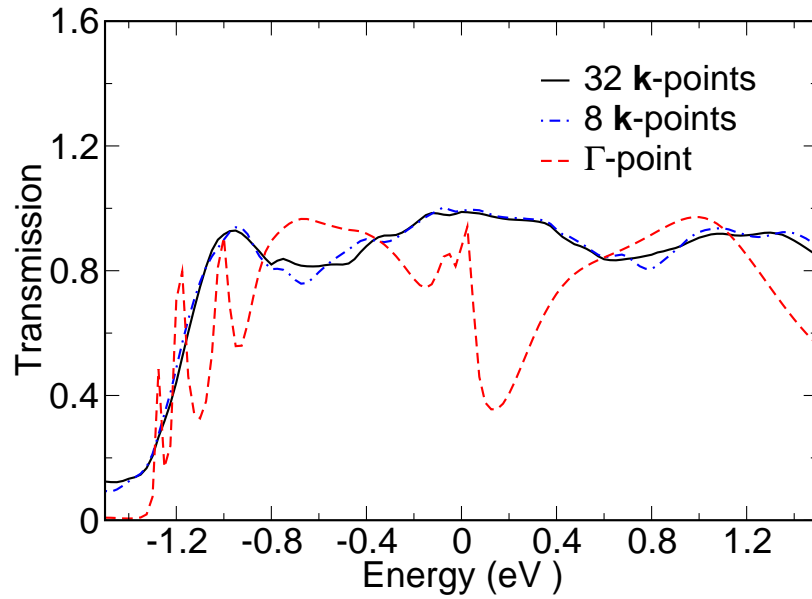
Figure 5.4: The transmission function for the Pt-H_2-Pt junction calculated using different $\mathbf{k} - point$ samplings. The Γ point calculation shows an unphysical peak near the Fermi level

We note in passing that such a peak is present in the transmission function reported in Ref. [67]. Such unphysical features resulting from an insufficient $\mathbf{k}_\perp$-point sampling are not properties of the molecular junction, but are rather due to van Hove singularities in the quasi one-dimensional leads [59]. The results reported in Ref. [75] are based on Siesta DFT code and show good agreement with our results. The conductance obtained in one of the early theoretical calculations [76] on the hydrogen molecular bridge are considerably lower than our and most other results.

5.1.3   Au(111)-benzene dithiolate contact

The Benzene-1,4-dithiol (BDT) molecule suspended between gold electrodes was among the first single-molecule junctions to be studied and has become the standard reference for calculations of nano-scale conductance. Depending on the experimental setup, measured conductances vary between 10^{-4} G_0 and 10^{-1} G_0 [77, 78, 79, 80, 81], while the calculated values typically lie in the range $(0.05 - 0.4)$ G_0 [82, 83, 20, 70, 21, 22, 71, 84]. In general it has been found that the transmission function is strongly dependent on the bonding site of the S atom [83, 71], while variations in the Au-S bond length only affects the transmission function weakly [82].

As our objective is to establish a computational benchmark for the Au-BDT system we choose the simple junction geometry shown in Fig. 5.5(a). The S atoms are placed at the minimum energy positions in the fcc hollow sites of the Au(111) surface and the molecule has been relaxed while keeping the Au atoms fixed in the bulk crystal structure. We use an Au lattice constant of 4.18 Å, and a distance between the Au(111) surfaces of 9.68 Å. With these constrains the relevant bond lengths are: $d_{\text{Au-S}}$=2.45 Å, $d_{\text{S-C}}$=1.73 Å, and $d_{\text{C-H}}$=1.09 Å.

In Fig. 5.5(b) we show the calculated transmission functions (the SZ result has been omitted for clarity). Notice that we plot the transmission function only up to 2 eV above the Fermi level. This is because the the WF transmission at larger energies is sensitive to the parameters used in the construction of the WFs, in particular the cutoff energy E_0, and thus we cannot be sure about the WF result above 2 eV $+ \varepsilon_F$.

The three transmission functions agree very well in the energy range from 2 eV below the Fermi level to 1 eV above the Fermi level, while only the DZP result agrees quantitatively with the WF result in the entire energy range. We again notice the down shift of the PAO transmission functions relative to the WF result.

The presence of a broad transmission peak positioned ~ 1 eV below the Fermi level is in qualitative agreement with previous results [83, 82, 70, 20, 85, 86]. For more stretched configurations, i.e. for larger values of the S-C bond length, than the one used in the present study, the broad peak splits into two more narrow peaks [63].

The transmission function presented in Ref. [20] was obtained using a method very similar to our method 2, however, the reported conductance of 0.4 G_0 is almost twice as high as our DZP results of 0.24 G_0. The large conductance arises because the transmission peak closest to the Fermi level is considerably broader than what we find. If, however, we restrict the $\mathbf{k}_\perp$ to the Γ-point we find the same broadening as in Ref. [20] and a very similar conductance of 0.37 G_0.
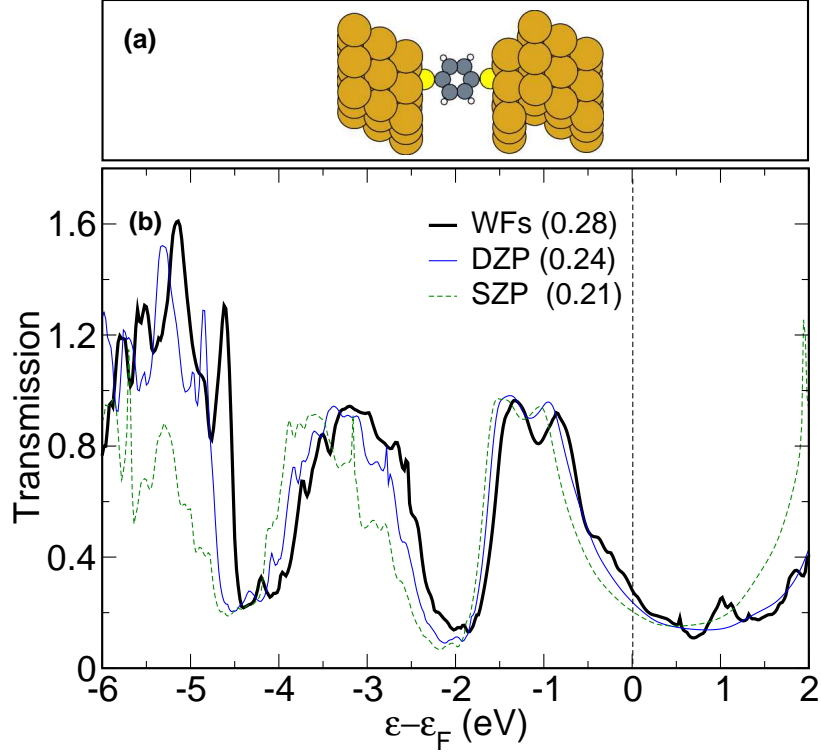
Figure 5.5: (a) Supercell used to model the central region of the Au(111)-BDT-Au(111) system with S at the fcc hollow site. (b) The calculated transmission functions. Note, that the SZ transmission function has been omitted for clarity. The transmission function at the Fermi level is indicated in the parenthesis following the legends.

Another feature of the Γ-point only transmission function is that the second peak positioned at ~ 3 eV below the Fermi level separates into a number of more narrow peaks.

In Ref. [70] the transmission function is calculated from the LMTO-ASA method and averaged over 36 irreducible $\mathbf{k}_\perp$-points. Both the width and the position of the two peaks in the transmission function at 1 eV and 3 eV below the Fermi level, are in good agreement with our results. The height of the former peak is, however, lower than in our calculation and this reduces the conductance to a value of 0.07 G_0. We suspect that this difference could be due to differences in the adopted contact geometries.

When comparing a supercell approach to quantum transport with a cluster based calculation as the one in Ref. [82] it is essential that: (i) The cluster size

is converged, and (ii) the number of $\mathbf{k}_\perp$-points and supercell size are converged. In the supercell approach a $N \times N$ Monkhorst-Pack sampling of the surface Brillouin zone corresponds to a Γ-point calculation for a supercell consisting of the original supercell repeated $N \times N$ in the surface plane [8, 62].
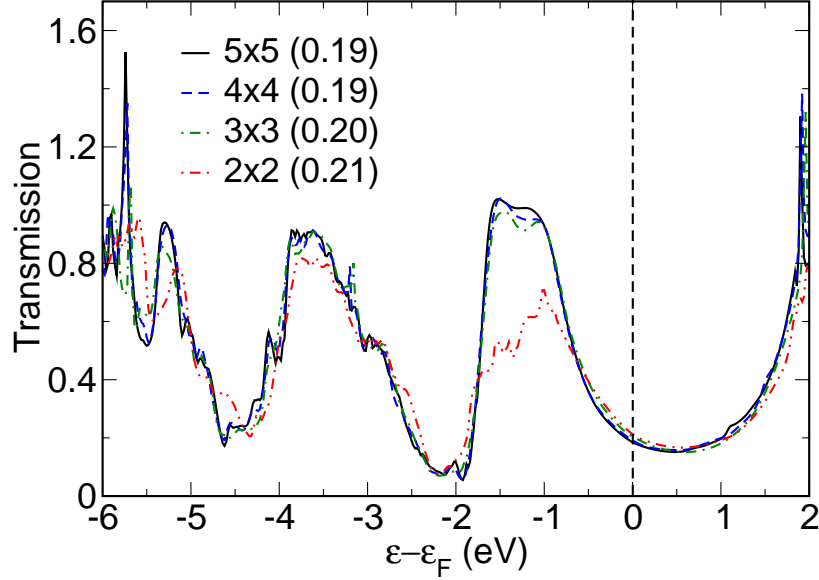

Figure 5.6: The transmission function of Au(111)-BDT-Au(111) for supercells containing a single BDT molecule and with the number of Au(111) surface atoms varying from 2x2 atoms to 5x5 atoms, as indicated in the legends. All the calculations apply the SZP basis set, and have been converged with respect to the number of $\mathbf{k}_\perp$-points. The transmission function at the Fermi level is indicated in the parenthesis following the legends.

Extrapolating our converged calculations for 3×3 atoms within the surface plane of the supercell and 4×4 $\mathbf{k}_\perp$-point to a Γ-point calculation gives a supercell consisting of ~ 1000 atoms. We speculate, that clusters of similar sizes are needed to reach the same level of convergence. However, the repeated supercell introduces a periodic array of molecules on the surface, which could give rise to interference effects blurring the comparision to single molecule cluster calculations. To quantify this inter-molecule interference effect we show in Fig. 5.6 the SZP transmission function for the Au(111)-BDT-Au(111) system where the number of Au atoms in the surface plane is varied from 2×2 atoms to 5×5 atoms. Each calculation has been converged with respect to the number of $\mathbf{k}_\perp$-points by a 4×4 Monkhorst-Pack sampling for all the supercells, except the

smallest supercell for which 8×8 $\mathbf{k}_\perp$-points was needed.

It is evident that the transmission function is well converged with 3×3 atoms in the surface plane. This shows that our calculations should be directly comparable to fully converged single molecule cluster calculations.

Chapter 6

Chain formation

The thinnest nanocontact between two metal bodies often takes the shape of regular atomically thin suspended nano wires. Due to the low coordination number of the involved atoms, these ultimate one-dimensional quantum wires may exhibit high mechanical stability and are chemically far more reactive than their bulk counterparts [25, 13, 87, 88, 89, 90]. This, combined with their ability to sustain extremely large current densities, makes atomic chains interesting from both a fundamental and a technological point of view.

Freely suspended homogeneous atomic chains of up to ten atoms may be formed by breaking a nano-contact under cryogenic conditions using a mechanically controllable break junction or a scanning tunneling microscope [91, 13, 92, 15]. Although spontaneous chain formation of homogeneous systems is observed only for certain transition metals (Au, Pt and Ir) [93, 94], the incorporation of impurity atoms, such as oxygen, have recently been found to act as chain formation promoters for Ag and Cu [26, 1], which are not themselves among the chain-forming metals [90, 95]. Alternative experimental techniques, such as deposition onto an insulating substrate, might also be used to produce atomic chains or wires for a larger range of metals [96, 97].

Concerning the stability and formation of atomic chains the general question naturally arises: What is the physical mechanism guiding the formation of chains? As key parameters determining the chain formation ability, both the ratio of the bulk to chain breaking force [94] and the resistance of a free standing chain against clustering [98] have been proposed. Interestingly, chain formation ability has been linked to the reconstruction of surfaces of the involved atoms [93, 1]. As will be demonstrated in the present chapter, metals for which chain formation may be observed experimentally and theoretically through elaborate calculations such as molecular dynamic simulations [93, 94, 90] can be

characterized by having a local minimum in the tip suspended chain string tension. The string tension is based on a simple thermodynamic model. This model provides an extreme simplicity of both calculation and understanding. The focus of this chapter is simple homogeneous metal contacts. However, this method may also be applied to the study of complex systems involving molecule and impurity atoms. An example of this will be given in Sec. 7.1 for oxygen atoms incorporated into silver chains.

The chapter is organized as follows. First, a thermodynamic model for studying chain formation is developed. This is followed by the result of DFT energy calculations of the needed parameters for a variety of homogeneous metallic chains. The results are found to be in excellent agreement with experiments and more elaborate molecular dynamics simulations [94].

6.1 String tension model

In order to theoretically describe the evolution of a nanocontact from the initial formation of a rather thick wire towards a monatomic chain, a proper thermodynamic potential governing the evolution should in principle be identified. To this end, we consider two options.

(i) Both the tip and nano wire are included in the description and the evolution at temperature T is governed by the canonical free energy $F(N, T)$ of a large number of atoms N. This is the more fundamental approach, but it will have a very high first-principle computational cost. Studies performed along this line have been based on a more approximate description of the interaction between the atoms, such as tight-binding and effective-medium-theory potentials [99], combined with molecular dynamics simulations [94, 90].

(ii) Here we propose a simplified alternative following the work of Tosatti *et al.* [100] on the thinning and observation of magic (long lived) suspended silver and gold nanotubes. The equilibrium state of an N atom free chain minimizes the free energy F. However, the aim here is not to describe a free chain, but rather a tip-suspended chain contacted with two bulk-like tips with which it can exchange atoms. To this end, we approximate the tips as bulk-like atom reservoirs, and introduce the grand canonical potential

$$G = F - \mu N, \tag{6.1}$$

which may be regarded as the positive work done in drawing a chain out of the tips [100]. This setup is illustrated in Fig. 6.1. Now the free energy F refers to an isolated chain, while the two tips and contacts enter only through the bulk chemical potential μ. In this simplified picture, important complications,
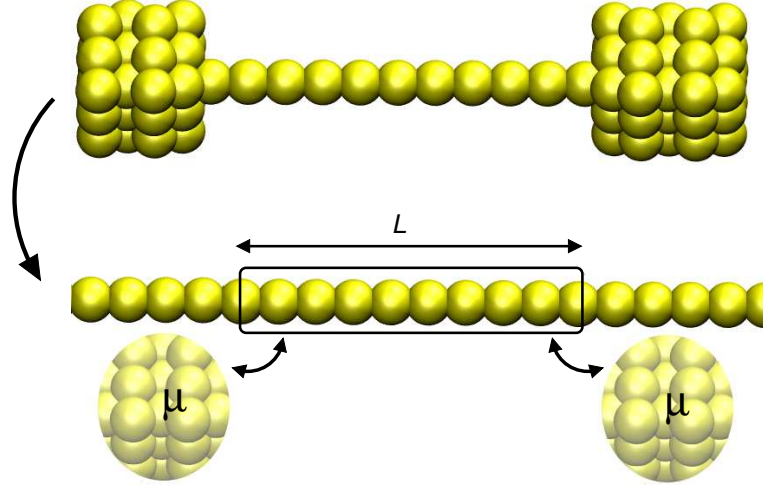
Figure 6.1: The full structure consisting of both the chain and the bulk-like tip shown above is replaced by a simpler model system shown below. The model system consist of a finite piece of wire with length L for which periodic boundary conditions are applied. The wire may exchange atoms with two bulk reservoirs. The exchange of atoms with the bulk reservoirs is in affect the linear atomic density n.

such as the nature of tip-chain junction, are completely neglected. In return, a significant simplicity in both calculations and understanding is obtained. The most stable tip-suspended chain will minimize G. At this point we mention that a general methodology exists for obtaining free energy estimates from experimental tunable parameters using zero temperature ground state DFT calculations [101, 102, 103]. However, we shall focus on chain formation trends and therefore simplify things by assuming a zero temperature, $T = 0$. Consequently, the chain free energy F and the chemical potential μ may be approximated directly by the relevant zero temperature DFT calculated energies, i.e. for metal atoms the chemical potential can be taken as the bulk binding energy per atom.

We now consider now a N atom chain of length L suspended between two tips (included through the chemical potentials) and described by

$$G^0(N) = E(N) - N\mu, \tag{6.2}$$

where $E(N)$ is the binding energy of the N atom chain.

In order to calculate $E(N)$, a reference model system for the chain must be chosen. Here, we consider the N atom chain of length L to be a finite piece of an infinite periodic wire, see Fig. 6.1, and make the approximation $E(N) \simeq NE_1$, where E_1 is the chain binding energy per atom. By introducing the linear atom

density $n = N/L$ we obtain

$$G^0(n) = nL(E_1(n) - \mu). \tag{6.3}$$

The length L is a constant that will determine the allowed discretized values of the atom density, i.e $n = N \times L^{-1}$. However, the linear density dependence of G^0 is not affected by L and we might just as well consider G^0/L. We shall refer to this as the string tension γ [100] expressed as

$$\gamma(n) = f(n) - n\mu, \tag{6.4}$$

where $f = nE_1(n)$. In the low atom density limit $\gamma(n) \sim -n\mu$, since the atoms are no longer bonding, i.e $E_1 \simeq 0$.

   The linear atom density can all ways be lowered by donating atoms from the chain to the bulk reservoirs and the global minimum of γ will in turn correspond to a $n = 0$ atom chain, e.g. all the atoms are in the bulk. This is clearly a broken chain. But how can chains then be observed? To address this question, consider first the case where γ is monotonically decreasing towards the low density limit. In this case the chain is unstable, since it is always advantageous to move a single or a few atoms from the chain and into the bulk. However, if the string tension has a local minimum, a situation may arise where both the donation and extraction of atoms from the bulk will increase the string tension (energy per length) signifying a meta-stable state. This implies that a criteria for chain formation is related to $f'(n) = df(n)/dn = \mu$. In the case where $f'(n) \neq \mu$, for any relevant n, then the chain is unstable. On the other hand, if $f'(n) = \mu$ for some n, which additionally corresponds to a minimum, the model implies a stable chain.

   From Eq. (6.4) it is clear that the only quantity to calculate besides the chemical potential μ of a bulk atom is the binding energy per atom E_1 of an infinite chain as a function of the linear atom density n.

6.2   Atomic metal chains

We consider a range of atomic metallic chains: Ir, Pt, Au, Co, Ni, Pd, Cu, Ag, Al and Na. All calculations have been performed using the plane wave code DACAPO with a plane wave cutoff and density cutoff of 25 Ry and 35 Ry, respectively. Exchange and correlation was included through the PBE functional [32] and 32 **k**-points was used to sample the chain Brillouin zone. Calculations of the bulk properties were performed using a $12 \times 12 \times 12$ Monkhorstpack **k**-point grid. Spin polarized calculations were performed for Co and Ni.

We note that various instabilities, including zig-zag and Peirls dimerizations, are often invoked for monatomic chains. The former indicates that chains spontaneously collapse into zig-zag or "double" chain structures [104]. A Peirls dimerization is also theoretically expected for half-filled 1D bands ,which would introduce an energy gap in the spectrum. Based on this, a two atom super-cell which can describe these mechanisms is selected as the reference chain model system.

In order to avoid interactions between the repeated cells in the plane perpendicular to the chain, a supercell with transverse dimensions of 12Å × 12Å was used. The chemical potentials for each of the metals was calculated as the bulk binding energy of an atom in a relaxed fcc crystal. The binding energy per atom of chains $E_1(n)$ was obtained by fully relaxing each structure for a large range of linear atom densities. Note, the approximation $E(N) \simeq N E_1$ is in fact exact for the model chain system used here.

An example of such a calculated binding energy curve is shown in Fig. 6.2 for the case of Al. Here, the binding energy is with respect to the spin-paired isolated Al atom. The binding energy at the (local) minimum is $E_1 = -1.84$ eV,
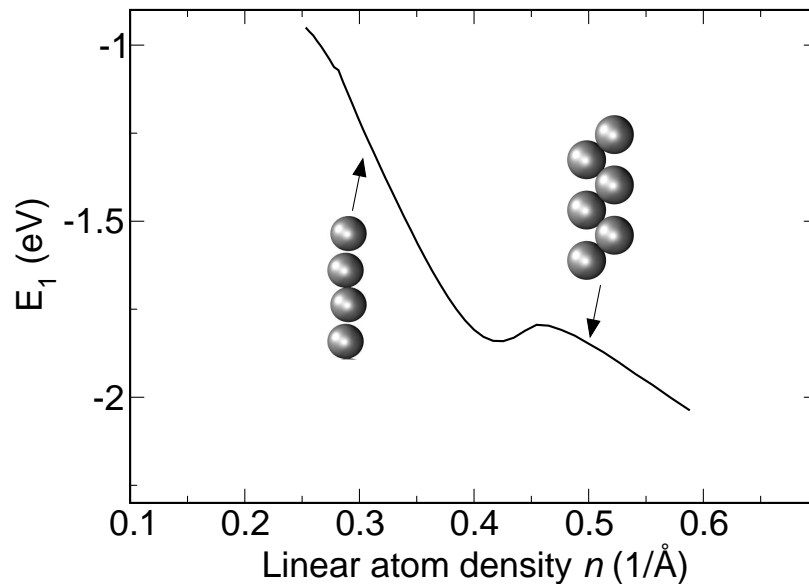

Figure 6.2: The binding energy per atom as a function of the linear atom density. The insets show the relaxed chain structures corresponding to a low and high linear atom density, respectively.

in good agreement with previous calculations [105]. The inset shows the relaxed

structures at a low and high linear atom density corresponding to a linear and zig-zag chain, respectively. We note in passing that the Al chain binding energy curve has a local minimum such that the chain does not suffer from a zig-zag instability. Consequently, according to the condition proposed in Ref. [98], Al chain formation should be possible.

In Fig. 6.3 we show the calculated string tension for a range of metals. The metals (Ir, Pt and Au) for which a local minimum is visible are shown in the left panel. The right panel contains the metals for which the string tension clearly shows no, or only very weak, local minima (Co, Pd and Na) or a flat plateau/tiny string tension "barrier" (Ni, Ag, Al and Cu). These results are in good agreement with the experimental observations that only Ir, Pt and Au readily form long tip suspended chains [93]. We take this as an indication of the model's ability to describe chain formation trends.

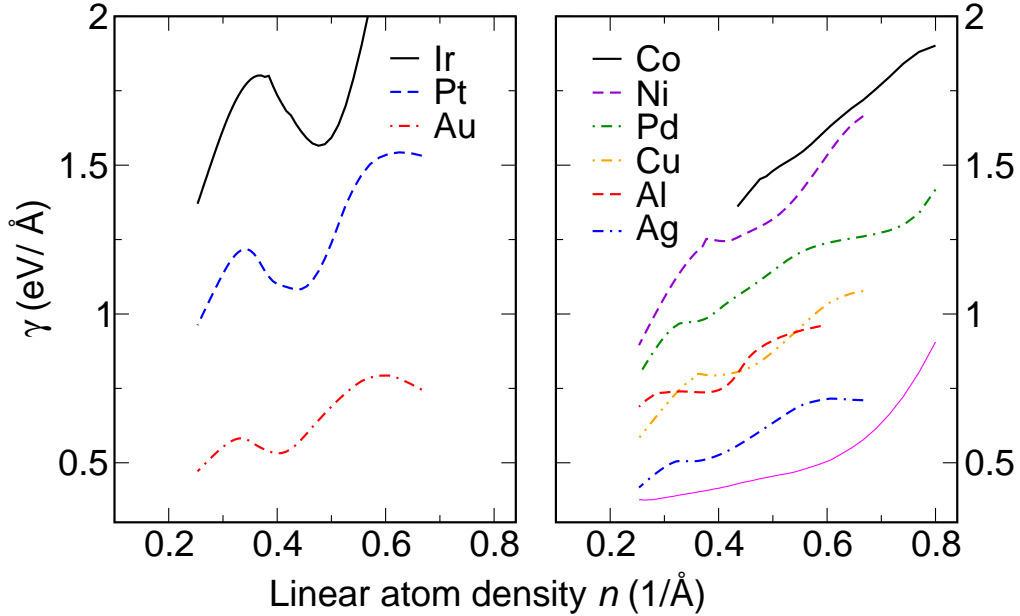
Figure 6.3: Calculated string tension for different chain geometries characterized by the linear atom density n. The left panel contains the metals for which a local minimum is visible, while the right panel contains metals for which the string tension barrier is either absent or very small.

Concerning the zig-zag instability we observe a general trend of high string tension for linear densities corresponding to zig-zag chains. In other words, the zig-zag instability observed for most of the free atomic chains is removed

when tip-suspended. The physical mechanism included in the model, which is responsible for this behavior, is that the energy gained per atom associated with the restructuring to a zig-zag conformation is out weighed by the energy cost of extracting atoms from the two bulk reservoirs of the tips. This indicates that the zig-zag instability criteria is less crucial in determining which metals can form tip-suspended chains.

Furthermore, the lowest string tension "barrier" is at lower densities, and is related to the stretching and finally breaking of bonds. This is in agreement with the proposed bulk/chain breaking force ratio as a key determining factor for chain formation [94]. We stress that for the results in Fig. 6.3 the chemical
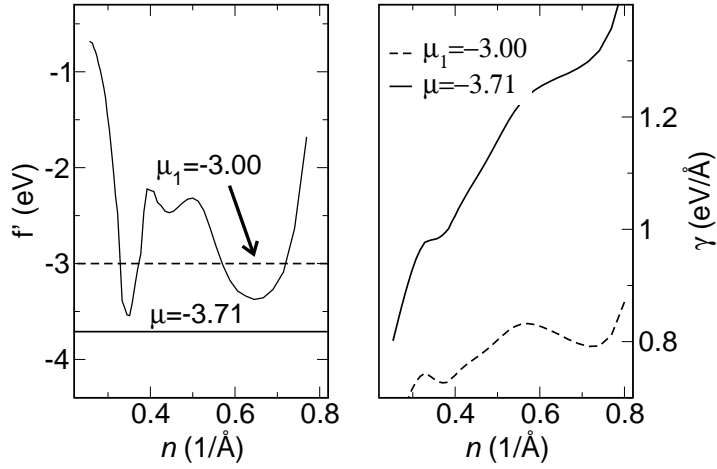

Figure 6.4: Left: An intersection of $f'(n)$ and a chemical potential signifies a possible meta-stable tip-suspended chain (see the discussion after Eq. (6.4)). Right: String tension for Pd for two chemical potentials.

potentials were all taken as the binding energy of an atom in a fcc crystal, in order to study chain formation trends. However, the chemical potential of the bulk-like tip atoms for a particular element can influence the string tension behavior and thus the chain formation properties.

As an example, consider the string tension for Pd atomic chains. In Fig. 6.4(right) the string tension obtained using either the bulk binding energy $\mu = -3.71$ eV (solid line) or $\mu_1 = \mu + 0.71$ eV (dashed line) is shown. The change in the chemical potential from μ to μ_1 clearly has an effect on the string tension and in fact local minima may now be observed. This behavior may be understood by considering $f'(n)$ and the chemical potentials (see the discussion after Eq. (6.4)) shown in Fig. 6.4(left). For the chemical potential μ, there is no intersection

with $f'(n)$ and no local minimum exists. However, changing the chemical potential to μ_1 leads to several intersections, and results in the observed extrema in the string tension.

Finally, we address the role of the discrete nature of n for a chain of finite length. To this end, we consider a (5-10) atom chain, which in the meta-stable state will corresponds to a length of 12 Å $\lesssim L \lesssim$ 25 Å. The allowed values of n are therefore equidistantly spaced, with 0.04 Å$^{-1} \lesssim n \lesssim$ 0.08 Å^{-1}, which in turn implies that the local minima may be "resolved".

Chapter 7

Characterization of an Atomic Chain Junction:
Ag-O chains in Ag

At sufficiently low temperatures the conduction electrons in a metal may often travel hundreds of nanometers without losing their quantum mechanical phase [65]. Under such conditions, the wave nature of electrons becomes important and manifests itself directly in macroscopic quantities such as the electrical conductivity. A remarkable result first predicted by DFT calculations is that the conductances of suspended atomic chains of elements such as C, Na, and Au oscillate with a period of two as the number of atoms in the chain is varied [14, 106]. In fact, calculations on the monovalent metals Na, Cs, Cu, Ag and Au have all shown period two or "even-odd" oscillations in the conductance. This behavior may be understood from a local charge neutrality condition. This implies that the Fermi level must be aligned with the center of a resonance for odd N and lie directly inbetween two resonances for even N. Deviations from these even-odd oscillations naturally occur for metals with more complex valence configurations such as Al and Pt [107, 108]. Common to the oscillations observed for all the homogeneous metal chains is that the conductance maximum (per contributing channel) is always close to $1G_0$, while the oscillation amplitude varies significantly from $\sim 0.05G_0$ in the case of Au [108, 109] to $0.5G_0$ in the case of Al and C chains [107, 21]. As discussed in Chapter 6, only certain metals (Ir, Pt and Au) have been found to form tip-suspended chains. Consequently, the theoredical prediction of conductance behavouir of long chains formed from other metals cannot at present be tested experimentally.

A striking deviation from this situation was observed in a recent experiment

by Thijssen *et al.* [26]. Firstly, the presence of oxygen was shown to greatly enhance chain formation when a Ag or Cu contact is broken at low temperature in a mechanically controlled break junction. Secondly, the conductance for the oxygen exposed Ag contact averaged over many chains and plotted as a function of chain length showed an exponential-like decrease from $1G_0$ to $0.1G_0$. Upon further extension, the conductance stayed constant over almost 1 nm. Similar features were observed for the O exposed Cu contact.

This is indeed an interesting result. The initial decrease in conductance suggests a chain with a band gap. However, this is not in line with the saturation at a finite conductance for longer chains. On the other hand, a length-independent conductance of $0.1G_0$ does not comply with the results for metallic chains discussed above, which exhibit conductance oscillations with a maximum on the order of $1G_0$. Prevous theoredical studies of the conductance properties of metal contacts (Ag, Au and Ni) exposed to oxygen have considered only one or two oxygen atoms [88, 110, 111, 112, 113]. Consequently, the studied structures were considerably shorter than the ones observed by Thijssen *et al.*, and cannot be related to the perculiar features of Ag chains exposed to oxygen.

In this chapter, we begin with a review of the main results of the experiments on Ag/O nano-contacts. This is followed by a discussion of the atomic structure of the tip suspended Ag/O chains based on the model introduced in Chapter 6. Finally, we present the results of the conductance calculations which are in good agreement with the experiments. It is shown that the conductance properties of Ag/O, as well as other metal chains, may be understood in terms of the reflection probability and phase shift at a single bulk-chain interface. The origin of the unexpectedly low conductance oscillations around $0.1G_0$ found for Ag/O may be traced to an additional phase picked up by an electron being reflected at the end of an alternating Ag-O chain. Furthermore, this Ag-O chain is found to be half-metallic, meaning that only electrons with a given spin direction may pass through the chain, making it a perfect spin-valve.

All DFT calculations for energies and structure relaxations have been performed with the DACAPO code [2]. A plane wave cutoff and density cutoff of 25 Ry and 35 Ry was used, respectively. Exchange and correlation effects were included through the PBE functional [32] and the ion cores were replaced by ultrasoft pseudopotentials [7]. The surface Brilluin zone was sampled by 4×4 **k**-points, and the system was allowed to spin-polarize.

The spin-polarized conductance calculations were in turn performed for the fully relaxed structures using method 2, and the same **k**-point sampling as for the structure relaxations. A SZP polarized basis set used in the transport calculations was found be sufficient and give results in good agreement with a Wannier function calculation. Consequently, a SZP has been used for all the transport

calculations in the present chapter.

The majority of the material presented in this chapter is a summary of Paper III and Paper V. However, the results on the stability of Ag/O chains in Sec. 7.1 have not yet been published.

7.0.1 Break junctions experiments on Ag/O contacts

The measurements on Ag/O contacts were performed using the mechanically controlled break junction technique (MCBJ) introduced in 1985 by Moreland and Ekin [114] and further developed by Muller *et al.* [115].
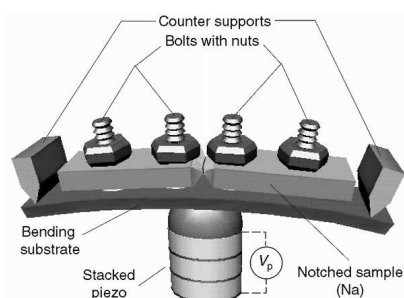

Figure 7.1: Working principle of the mechanically controlled break-junction technique. A notched metal wire is fixed by two drops of epoxy adhesive (illustrated as bolts) and can be stretched in a three point bending configuration by means of a piezo electric element.

The working principle of the technique is illustrated in Fig. 7.1. First, a surgical knife is used to make a notch in a metal wire which is then glued onto an elastic insulating substrate by two drops of epoxy adhesive. The elastic substrate is then mounted in a three-point bending configuration and the whole setup is placed in a vacuum chamber and cooled down to around 4.2K. The wire may be stretched with subatomic precisicion by moving the piezo-element forward. During the pulling and subsequent thinning of the contact, the atoms reconfigure causing sudden jumps in the conductance. An example of this behavior is seen in the conductance traces in Fig. 7.2 for Au, Ag and Cu before and after exposure to oxygen shown in the top and bottom panel, respectively. Due to the large number of atoms involved, even in the last stages where atomic thin chains can form, it is nearly impossible to predict beforehand the exact evolution and thinning of the contact, and thus the conductance trace. By repeatedly breaking and remaking the contact, and recording the conductane at a fixed time-interval, the common features shared by many individually prepared contacts may be
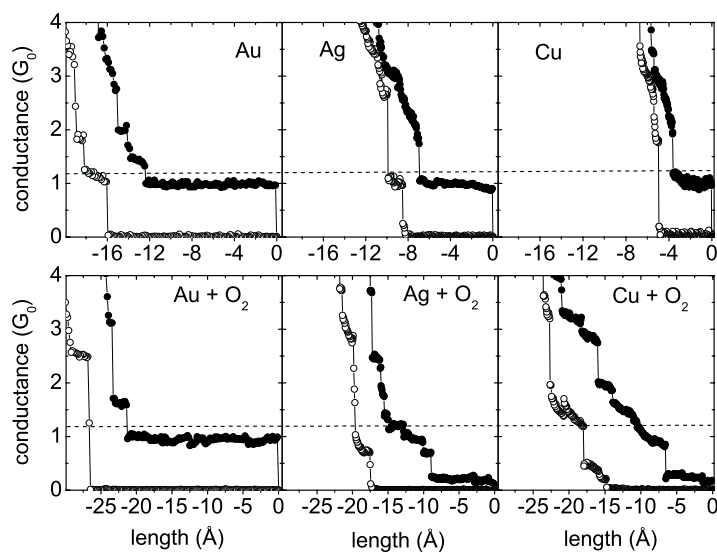
Figure 7.2: Typical conductance traces for Au, Ag and Cu before and after exposure to oxygen are shown in the top and bottom panels, respectively.

revealed through analysis of the statistical data, such as average values and histograms.
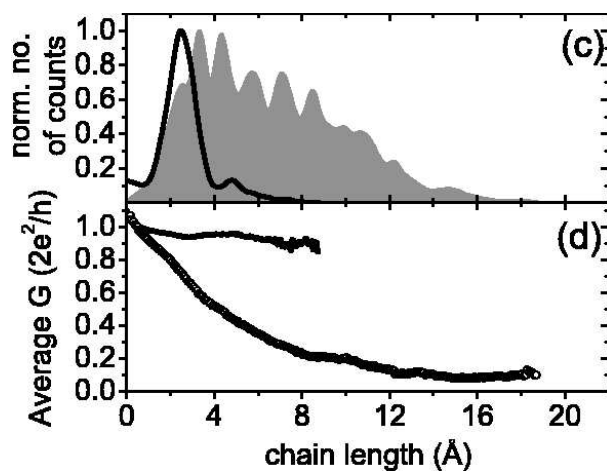

Figure 7.3: The experimentally obtained length histogram and the average conductance are shown in the top and bottom panel, respectively. The grey shaded area in the length histogram is for Ag exposed to oxygen gas, while the black line is for pure Ag.

In Fig. 7.3 the length histogram and average conductance (for Ag and Ag/O) is shown in the top and bottom panel, respectively. The length histogram has been constructed by recording the distance a contact may be pulled from the point where the conductance drops below $1G_0$ until the contact finally breaks. The contact rupture is identified by a sudden conductance drop into the deep tunneling regime. For pure Ag contacts, which are denoted by the black line, a single peak around 2.6 Å is obtained. This indicates that only relatively short structures with a chareteristic length of a few Å are formed in the last stages before the contact breaks. Having prepared the Ag contact admitting oxygen gas into the chamber leads to a drastic change in the length histogram. Several peaks may now be observed and considerably longer structures are formed with lengths up to 20 Å. The distance between the peaks may be considered to be the difference in length between particularly stable tip-suspended chains.

The average conductance of Ag, shown in the lower panel in Fig. 7.3, reveals that in the final stage of stretching a chareteristic structure appears with a conductance close to $1G_0$. Similar conductance values are also observed for homogoneous Au and Cu contacts, as shown in Fig. 7.2. On the other hand, the Ag/O contacts show a very different behaviour. After an initial exponential like conductance decrease, a plateau extending over 1 nm is formed with a conductance around $0.1G_0$. Note that in the region where the conductance is decreasing pure Ag structures may also form.

7.0.2   Point contact spectroscopy

In order to extract information about the structure of the Ag/O contacts, the local vibrations were measured by point contact spectroscopy (PCS) [65]. In PCS the differential conductance is measured as a function of the bias voltage V applied across the junction. At the point where eV exceeds the energy of a vibration mode energy $\hbar\omega$ scattering events involving emission of phonons may take place. Recently, it has been demonstrated that the correction in the conductance of an atomic wire, for the electon-phonon interaction, depends on the transmission of the channel [116, 117]. It was predicted that in the case of a single fully transmitting channel the electrons are only backscattered by interactions with local phonons. At a half-transmitting channel forward and backscattering are the same and no correction is observed. For a less than half transmitting channel a net of forward scattered electrons results in an increase in the current.   In Fig. 7.4 the differential conductance is shown for a 7 Å long Ag/O chain. The transmission is clearly low and the upward steps seen in the spectra may be interpreted as inelastic forward scattered electrons. The observed frequency is around 100 meV which is much higher than the phonon

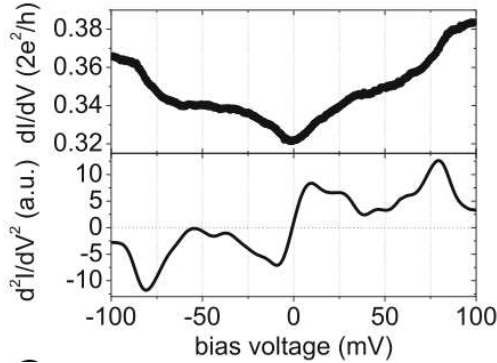Figure 7.4: dI/dV spectra obtained from low conducting Ag/O atomic chain structure which was ~ 7 Å long. A vibrational energy of 100 meV is observed

spectrum of bulk Ag. The associated vibrational mode must therefore involve O in either molecular or atomic form. Calculations of the vibrational frequencies of atomic oxygen in a silver contact are presented in Sec. 7.1.

7.1   Atomic structure and stability

In this section, the atomic structure, stability and vibrational frequencies of Ag/O contacts are discussed.

It was noticed by Smith *et al.* [93] that a relation between metals showing surface reconstruction and forming chains exists and was explained in terms of a strong dependence of the binding energy on the coordination. This was in turn related to relativistic effects. We note that although silver does not reconstruct, silver (110) surfaces reconstruct in the presents of oxygen. The structure shows rows of alternating silver oxygen chains (ASOC), e.g. —Ag-O-Ag-O—. This could indicate that a ASOC chain is a particularly stable 1D structure of Ag and O. Further evidence for the appearence of ASOC in the break junction experiments by Thijssen *et al.* is given in Paper III, where a simple model based on the interatomic distances of Ag-Ag and Ag-O was used to fit the experimental length histogram shown in Fig. 7.3. A particularly frequent occuring structure from this procedure was in fact the ASOC.

In order to investigate the local Ag/O structure in more detail, the vibrational frequencies of a single oxygen atom in a silver contact have been calculated. The starting point is the structure shown in Fig. 7.5, where the oxygen atom and the four atom Ag pyramids, as well as the surface-surface distance,

have been relaxed. The vibrational modes are then obtained by diagonalizing the Hessian matrix of the oxygen atom and the two apex Ag atoms defined by $\partial E/(\partial u_{n,c} u_{m,c'})$, where E is the DFT ground state energy and $u_{n,c}$ is the displacement of atom n in the direction $c \in x, y, z$, multiplied by the mass factor $\sqrt{m_n}$. The calculations identify 3 longitunal modes with the vibrational
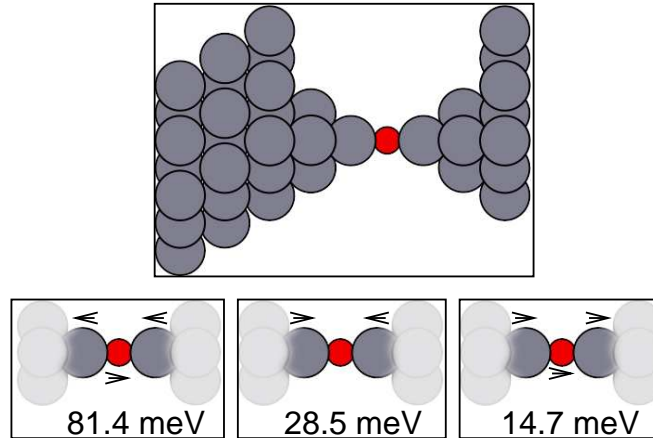

Figure 7.5: The supercell used for the DFT calculations of the vibrational modes of a single oxygen atom in a silver contact. Below: longitudinal vibration modes and the calculated vibrational frequencies.

frequencies $\omega_1 = 81.4$, $\omega_2 = 28.5$ and $\omega_3 = 14.7$ meV. The three vibrational modes correspond to (i) the oxygen atom moving in anti-phase with the silver atoms, (ii) the two Ag atoms moving in anti-phase and the oxygen atom being immobile, (iii) in phase motion of all three atoms. The relation between the vibration-mode energies may be accounted for by a simple model as described in Paper III. However, it is imediately clear that mode (ii) and (iii) have low frequencies compared to mode (i), due to the large difference in mass between Ag and O.

The high-energy mode is in good agreement with the measured vibrational energies in the range between 80 and 100 meV. We have not considered molecular oxygen. However, an oxygen molecule has double the mass of an oxygen atom, which would shift the energy of the high-freqency vibrational mode down by a factor of $\sqrt{2}$ to 57.6 meV, assuming a similar bond strength to Ag. This suggests that oxygen atoms, rather than molecular oxygen are incorporated into the chains.

Excluding molecular oxygen still leaves open the question of the composition and structure of the Ag/O chains responsible for the anomolous conductance

behavior for structures of with lengths up to 2 nm.

The results for homogenous metal chains in Sec. 6.2 indicated that chain formation was related to breaking of bonds and that strong chain bonds are a guiding factor in chain formation [94]. In Fig. 7.6 we show the calculated breaking force for three different Ag/O chains and their structure . The supercells correspond to the structures shown with transverse dimensions of $12\text{Å} \times 12\text{Å}$. In general, all structures were fully relaxed. The structure was stretched in increments of 0.2 Å from an initial compressed structure until finally breaking. From the DFT calculations, the breaking force was identified as the maximum force the chain in question could sustain.   The pure Ag chain was found to
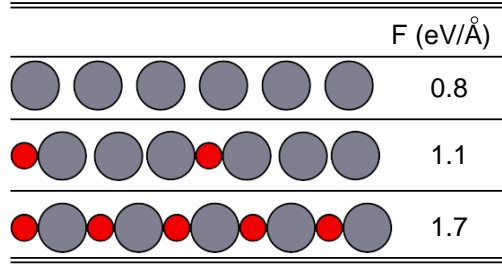

Figure 7.6: Breaking force, F, of Ag and O chains with various compositions

have a breaking force of 0.8 eV/Å, in good agreement with prevous DFT calculations [94]. Incorporating atomic oxygen into a $AgO_{1/3}$ chain enhances the mechanical strength slightly to 1.1 eV/Å. However, the ASOC has a strikingly higher breaking force of 1.7 eV/Å.

To sumarize, Ag(110) reconstructs forming ASOC, molecular oxygen may be excluded due its proposed low vibrational frequencies, and the breaking force of ASOC is much higher than Ag and $AgO_{1/3}$ chains. This all points in the direction of ASOC as a good candidate for further investigation.

To apply the string tension model developed in Sec. 6.1 to the system consisting of an ASOC suspended between two bulk-like tips, we take as a reference chain model system the supercell containing two formula units of AgO. This allows for the chain to zig-zag. For the tip-bulk reservoirs we use pure bulk Ag. To approximate the chemical potential of oxygen, we have calculated two different values: (i) The gas phase energy $\mu_{O,1} = E(\text{H}_2\text{O}) - E(\text{H}_2)$, and (ii) the gas phase energy $\mu_{O,2} = \frac{1}{2}E(\text{O}_2)$. The chemical potential difference is $\mu_{O,2} - \mu_{O,1} = 2.45$ eV. Using $\mu_{0,2}$ has recently been found to provide better agreement with experiment for the formation energies of various metal oxides [118].

The string tension expression in Eq. (6.4) may now be written in terms of the linear atom density as

$$\gamma(n) = f(n) - \bar{\mu}n, \tag{7.1}$$

where $f(n) = E(\text{AgO} \times 2)/4$ and the "average" chemical potential $\bar{\mu} = \frac{1}{2}(\mu_{\text{Ag}} + \mu_{\text{O},i})$, for $i = 1, 2$.
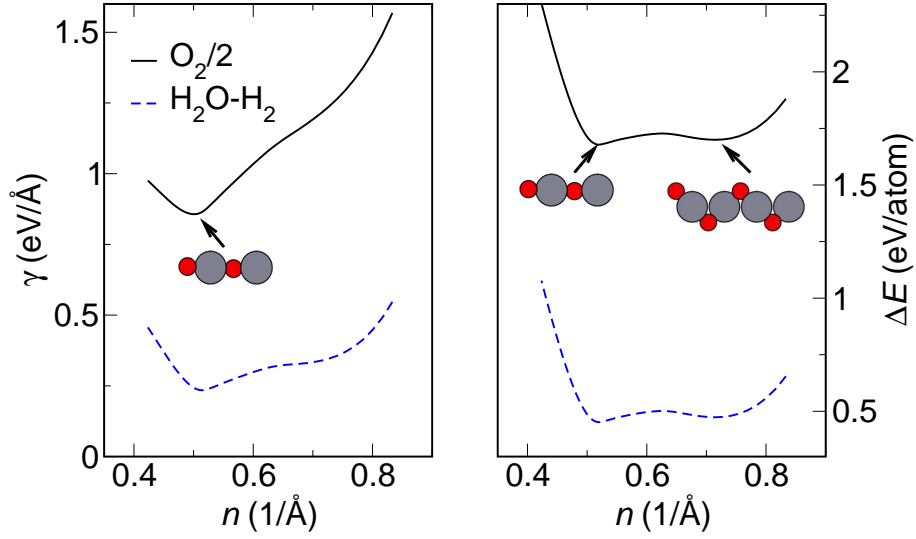

Figure 7.7: Left: String tension for an ASOC chain obtained from two different oxygen chemical potentials. The full and dashed line corresponds to chemical potentials obtained from gas phase DFT energies $\frac{1}{2}E(\text{O}_2)$ and $E(\text{H}_2\text{O}) - E(\text{H}_2)$, respectively. The robustness of the single string tension local minimum indicates that tip suspended ASOC chains may form. The structure corresponding to the local minimum is a linear ASOC chain with a Ag-O interatomic distance $d_{\text{Ag-O}}$ between 1.9 and 2.0 Å, dependent on the oxygen chemical potential. Right: The formation energy as a function of the linear atom density n. The two local minima corresponds to a zig-zag structure and a linear structure as shown by the insets.

In Fig. 7.7 the string tension and formation energy per atom ($\Delta E = E(\text{AgO} \times 2)/4 - (\mu_{\text{Ag}} - \mu_{\text{O,i}})/2$) is shown in the left and right panel, respectively. The full line and dashed lines corresponds to $\mu_{\text{O},2}$ and $\mu_{\text{O},1}$ respectively, as indicated in the legends. The string tension for both the oxygen chemical potentials show only a single local minimum. The structure which minimized the string tension is a linear ASOC shown in the inset. The destabilization of zig-zag chains is also observed for the ASOC. In fact the free ASOC chain has two local minima corresponding to a zig-zag and linear chain, see Fig. 7.7(right panel) . However,

when tip-suspended, the zig-zag structure is destabilized by the increased cost of a higher linear atom density compared to the energy gain of the chain alone, as discussed in Sec. 6.2. Furthermore, we mention that the tip suspended ASOC chain string tension minimum is robust since a variation of oxygen chemical potential (with 2.45 eV) does not change the qualitative behavior. The structure corresponding to this local minimum has an Ag-O interatomic distance between 1.9 and 2.0 eV for chemical potentials in the range between $\mu_{O,1}$ and $\mu_{O,2}$.

7.2   Conductance calculations

In this section we address the electron transport properties of the ASOC suspended between Ag electrodes. Based on these first principles conductance calculations, it will be shown that the anomolous conductance behavior of $0.1G_0$ for long chains may be understood in terms of a simple phase-shift model (see Sec. 3.4). Also, Al and Au are shown to be well described by this phase-shift or resonating-chain model.

To describe the scattering region we use the supercell shown in the inset of Fig. 7.8. It contains the oxygen terminated ASOC suspended between four-atom silver pyramids, which are attached to (111) silver surfaces. Both the Ag pyramid and the ASOC chain have been fully relaxed to obtain the most stable geometry of the linear ASOC chains found in the prevous section. Transport calculations are performed as described in Chapter 4 and applied in chapter 5.

In Fig. 7.8 we show the calculated conductance (blue squares) of the relaxed oxygen-terminated ASOCs as a function of the number of oxygen atoms N in the chain. We note in passing that the calculated conductances of Ag-terminated chains are significantly lower than the experimental value of $0.1G_0$ [1]. As discussed in the prevous section, these chains are probably less stable than oxygen-terminated chains and are likely to break in the Ag–Ag bond when elongated, see Fig. 7.5. As indicated in Fig. 7.8, we have considered relaxed chains with a length up to 23.0 Å, with the Ag-O bond length lying in the range between 1.95 and 2.10 Å, in correspondence with the local string tension minimum.

Fig. 7.8 also contains the experimental data, which is obtained by averaging the conductance trace of thousands of chains, so that features such as small-amplitude conductance oscillations are not visible. For long chains, however, there is excellent agreement between the measured and calculated (average) conductance. The significantly larger conductances found in the experiments for shorter chains are presumably due to contributions from pure Ag chains which have a conductance around $1G_0$ (see Fig. 7.3). The calculated conductance of a single oxygen atom, $N = 1$, is $0.3G_0$, which is in good agreement with the
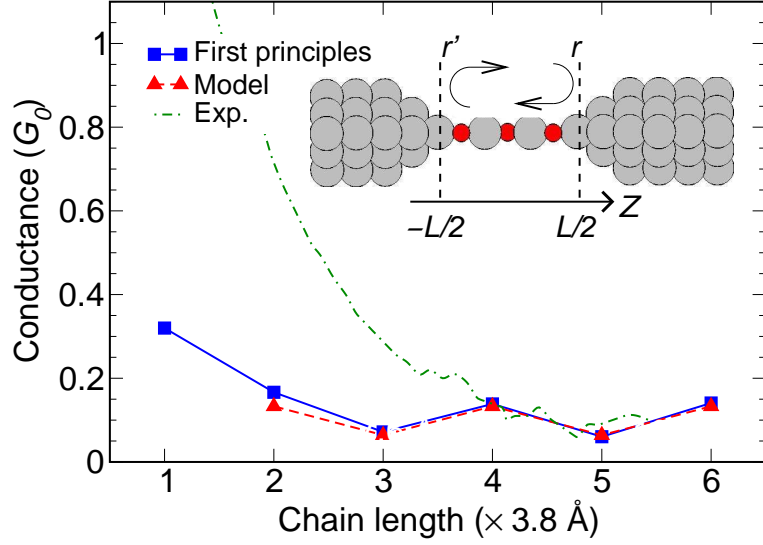
Figure 7.8: Calculated conductance as a function of chain length (blue squares). The length of the chain is given in units of 3.8 Å corresponding to the length of a AgO unit. The result of the resonating-chain model in Eq. 7.2 and experimental data are also shown. Shown in the inset is the supercell used to model the suspended chains.

results calculated in Ref. [110]. For $N > 1$ the conductance starts to oscillate with a period of two Ag-O units around an average value of $0.1G_0$. For a single oxygen atom, $N = 1$, we find a non-magnetic ground state, while for $N > 1$ the ferromagnetic state is energetically favored. For large N the electronic structure of the chain converges toward that of the infinite alternating Ag-O chain. This has a ferromagnetic (half-metallic) ground state with a magnetic moment of $1\mu_B$ per Ag-O unit mainly localized on the oxygen. The energy gain with respect to the non-magnetic state is 0.12 eV per Ag-O unit.

To gain more insight into the nature of the conductance oscillations, we show in Fig. 7.9a) how the energy dependent transmission functions change with N, which varies from $N = 2$ in the top panel to $N = 6$ in the bottom panel. The fact that only minority spin states are present at the Fermi level means that the current will be fully spin polarized, making the ASOC a perfect spin-valve. The peaks in the transmission function are found to coincide approximately with the resonances of the chain. These in turn are broadened by coupling to the contacts.

The number of resonances increases linearly with N and their width decreases as $1/N$ due to a reduction in the overlap between the levels on the chain and the

states in the contact. The resonances on the chain have the same character as the Bloch states forming the valence band of the infinite Ag-O chain whose band structure is shown in Fig. 7.9b). The spin polarized valence band is two times degenerate, with angular momentum $m = \pm 1$ and Ag(4d)-O(2p) character. The character of the Bloch states may be identified from symmetry considerations. However, this can also be seen clearly from the Wannier functions associated with the anti-bonding band crossing the Fermi-level and a bonding band located in the energy range -2.5 to -4.5 eV (not shown).

The conductance oscillations in Fig. 7.8 clearly arise because the Fermi level intersects the nearest resonance closer to its center for even N than odd N. However, in contrast to the situation for homogeneous chains, the transport is never "on resonance" but always takes place via a resonance tail and cannot be explained by charge neutrality. Indeed, from Fig. 7.9a) it can be seen that the resonances are always almost completely empty or filled, and since each resonance can accommodate two electrons, it seems that all chains accommodate an even number of electrons. But each AgO unit contains an uneven number of minority valence electrons (5), and local charge neutrality would therefore imply a half-filled resonance for every second AgO unit added to the chain. On the other hand, the small-amplitude oscillations around the experimental saturation value of $0.1G_0$ arise exactly because the Fermi level always intersects the tail of a resonance. The fact that the ASOC chains are periodic allow us to model the transport of each of the two channels (due to orbital degeneracy) with a simple resonating-chain model for symmetric coupling (see Sec. 3.4)

$$T = \frac{1}{1 + 4\frac{R_1}{(1-R_1)^2}\sin^2(kL + \phi_1)}, \qquad (7.2)$$

where R_1 is the reflection probability for the semi-inifinte chain coupled to the semi-infinite Ag bulk contact, as shown in Fig. 7.10. L is the length of the chain and k is the Fermi Bloch wave vector. For a given reflection probability R_1, the total transmission will vary with the chain length between a maximum of 1 and a minimum of $((1 - R_1)/(1 + R_1))^2$. However, due to the phase shift and the discrete nature of the length of the chain, the transmission will oscillate over a more narrow region. We have determined the parameters R_1 and ϕ_1 for the ASOCs as well as for chains of Al and Au. The parameters are obtained by considering the reflection of an electron in a semi-infinite chain impinging on a contact We determine the scattering state $|\Psi_S\rangle$ using the calculational procedure described in detail in Ref. [52]. The phase shift can then be determined by projection onto the incoming ($+k$) and outgoing ($-k$) chain states as $\phi_1 = \arg(\langle\psi_{-k}|\Psi_S\rangle/\langle\psi_{+k}|\Psi_S\rangle)$. Note, that there is a certain arbitrariness in the
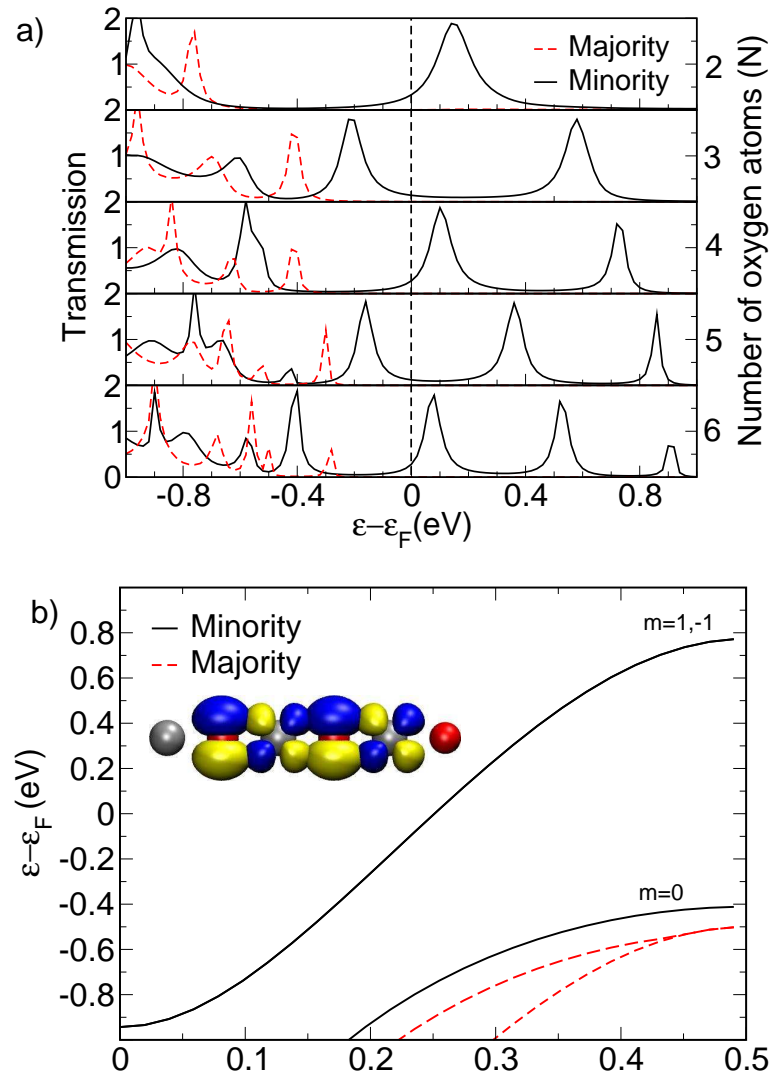
Figure 7.9: (a) Transmission function for the majority (red dashed line) and the minority spin (black full line) for AgO chains containing $2 - 6$ oxygen atoms. (b) Band structure of the infinite AgO chain. The valence band crossing the Fermi level, is doubly degenerate, and the Bloch states have $m = \pm 1$ symmetry with respect to rotation around the chain axis. The inset shows Wannier functions functions which can be associated with the half filled bands. They can be identified as p and d like atomic orbitals, each centered on O and Ag, respectively.

System	R_1	ϕ_1	kL	$T_{\max}$	ΔT_{osc}
AgO/Ag	0.64	-0.21π	$N\pi/2$	0.12	0.05
Al/Al(111)	0.43	0.92π	$(N+1)\pi/4$	0.85	0.57
Au/Au(100)	0.004	-0.36π	$(N+1)\pi/2$	0.997	0.010

Table 7.1: Calculated chain-contact reflection parameters for a number of systems.

definition of L in Eq. (7.2) which is reflected in different results of the phase shift ϕ_1, so that Eq. (7.2) is in fact independent of the particular choice of L [51].

In Table 7.1 the calculated reflection parameters for the ASOCs and for mono-atomic Al and Au chains are shown together with the obtained maximal transmissions and the magnitudes of the oscillations. In all three cases the model reproduces the results of full DFT calculations when varying chain lengths, as will be shown below. Note that the values are per channel (Al and Ag both have two eigenchannels).
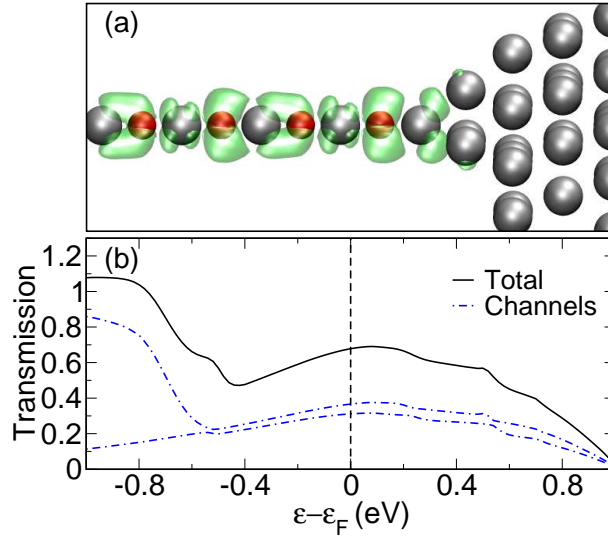

Figure 7.10: Top: Isosurface plot of an eigenchannel state at the Fermi level. Bottom: The transmission function for the chain-bulk interface.

The model results for the ASOCs are shown in Fig. 7.8 to coincide with the full calculations for chains containing two or more oxygen atoms. It should be noted that the low conductance of about $0.1G_0$ comes about not so much because

of the reduced reflection probability ($R_1 = 0.64$) which would still allow for a total transmission of 1 if a resonance condition could be met in the chain, but rather it is the phase shift of $\phi_1 = -0.21\pi$ which leads to destructive interference within the chain. We stress that the actual size of this phase shift is expected to depend on the electronic structure of both the chain and the contacts, and must be obtained from a full calculation. However, we note that a phase shift of $\phi_1 \simeq -\pi/4$ corresponds to a length of half a unit cell in the chain or equivalently an oxygen-silver distance, and this is in good accordance with Fig. 7.10 where the scattering state shown as a isosurface plot is seen to carry weight on the Ag tip atom and therefore is mostly reflected off the three-atom Ag layer below.
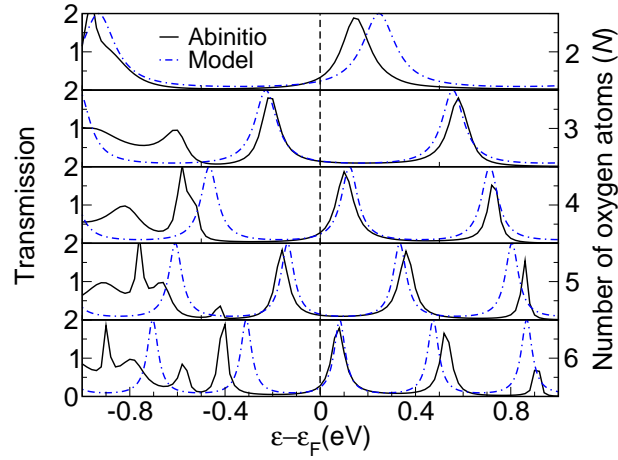

Figure 7.11: The minority energy dependent transmission function from the first-principles calculations (black) and from the transmission model of Eq. 7.2 (blue). The energy dependent transmission from the model function has been obtained by linearizing the band structure of the Ag/O chain around the Fermi level.

To make the relation between the resonator-chain model and the first-principles calculations of the energy dependent transmission function more obvious, we now consider the energy dependence of Eq. (7.2). In principle this requires the calculation of ϕ_1 and R_1 for each energy. However, we notice that the energy dependence of T_1 and thus $R_1 = T_1 - 1$ shown in the lower panel of Fig. 7.10) is rather weak and in turn approximate it with the value at the Fermi-level. If the phase shift is furthermore assumed energy independent, the only remaning energy dependent quantity in Eq. 7.2 is the Bloch wave vector k, which can be linearized around the Fermi-level.

In Fig. 7.11 we show the spin-minority channel result of these approximations

(blue dot-dashed line) and also for comparison the full first principle result (black line).

The resonator-chain model reproduces the energy dependence of the full calculations very well, including the resonant structure. This implicitly resolves the charge neutrality paradox: odd numbers of chain electrons still doubly-occupy an integer number of resonances when the effects of the phase shift at the boundaries are included. The approximations are in fact exact at the Fermi energy, which explains the very good agreement between the full calculations and the model at this point. Only for the shortest chain of $N = 2$ deviates noticable, indicating that the potential of the right side is dependent on the left side, i.e. the potential in the chain region is not yet converged.

To further investigate the applicability of the resonating-chain model, we show the results for the conductances of Al and Au chains in Fig 7.12 together with the results of earlier full DFT-transport calculations. The agreement is striking, even for rather short chains. In the case of Al, the phase shift is in agreement with the resonant-level model proposed in Ref [107]. The resonant-level model takes as a starting point the isolated chain (of length N) which is then coupled weakly to the leads. This boundary condition corresponds exactly to a phase shift of π. The small deviation of the phase shift from π accounts nicely for the fact that the conductance does not peak at $2G_0$ but only at $1.7G_0$, where the maximum of $2G_0$ is due to orbital degeneracy, e.g two channels. For
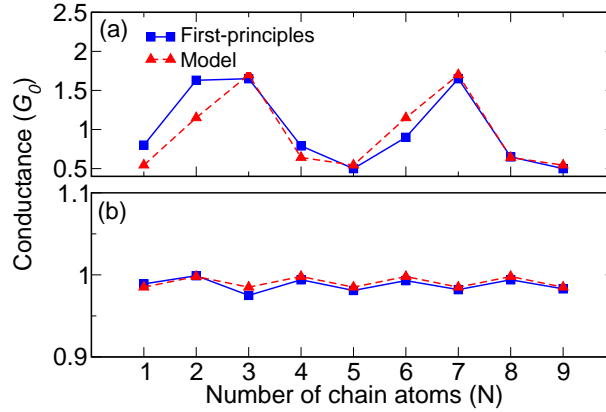

Figure 7.12: (a) Conductance for Al as a function of the number of chain atoms N. The first-principles result (squares) is taken from Ref. [107], while the model result (triangles) is obtained from Eq. (7.2)

Au we find the phase and amplitude of the even-odd conductance oscillations

in agreement with the first-principles calculations in Ref. 10. We note that the phase of the conductance oscillation is not explained by either a charge neutrality argument or a resonant model [107]. However, the phase of the oscillation may be related to our calculated phase shift of 0.36π, while the small oscillation amplitude can be traced to an almost perfectly transparent chain-bulk interface with a reflection coefficient of only 0.004.

7.3 Summary and outlook

First principles conductance calculations have been presented for alternating AgO chains suspended between silver bulk contacts. The AgO chains are half-metallic and can have an average conductance of $0.1G_0$, as was found in recent experiments. In fact, the conductance oscillates with a small amplitude and a period of two AgO units as the chain length is varied. The oscillations may be understood from a resonating-chain model, and are fully characterized by only two parameters, the reflection probability, R_1, and reflection phase-shift, ϕ_1, of a single bulk-chain interface. By extracting these two parameters from the DFT calculation, quantitative agreement between the full calculations and the model is obtained. Also, previous DFT transport calculations on Au and Al could be reproduced by the resonating-chain model.

Chapter 8

CO in transition and noble metal junctions

With the advent of molecular electronics, researchers have envisioned simple organic molecules as the basic building blocks in electronic devices. This has recently intensified the interest in electron transport in nanoscale contacts [91, 11, 119, 120]. If monanatomic chains represent the smallest possible electronic device interconnect, a small functional molecule could be the corresponding ultimate miniaturization of a transistor.

Experiments on single-molecule junctions have been performed with basically the same techniques used for studying monatomic chains described in the preceding chapter. These include mechanically controllable break junctions (MCBJ) [23, 121], scanning tunneling microscopy [122], and electro migration [12]. However, molecules introduced through a solvent might often influence the contact formation in an uncontrollable way. The organic molecules used are often carbo-hydride rings with end groups of sulfur or nitrogen designed to form strong bonds to the metal. These include bipyridine and benzene-dithiolate, as discussed in chapter 5 and in Paper II.

However, experimental techniques such as the MCBJ technique are performed at cryogenic temperature. This was used in the study of the Ag/O chains, and avoids the introduction of a solvent altogether. In fact, this technique has been used to also study several small molecules such as the hydrogen molecule [10] and carbon monoxide (CO) [4, 5] in metal junctions. For a Pt/H_2 junction, excellent agreement between experiment and DFT transport calculations was found [19].

Experiments on magnetic as well as nonmagnetic metal point contacts showed a fractional conductance of $0.5G_0$. This was interpreted as the lifting of a spin

degenerate conductance channel. However, the latter experiments could not be reproduced by Untiedt *et al.* [4]. Instead, they suggested that the reported fractional conductances could result from CO contamination. In recent experiments by Kiguchi *et al.* [5] the effect of bonding CO on metal contacts (Au, Pt, Ni and Cu) on the conductance was studied. The conductance histogram for Pt and Ni in the presence of CO indeed showed a clear peak at $0.5G_0$ in the conductance histogram. Regardless of whether CO is the source of the reported fractional conductances, the question of the physical mechanism still remains: is it a spin effect or does it have some other origin?

The chapter is organized as follows. First, the DFT results of simulated conductance traces of a homogeneous Pt point contact and short Pt chain are presented, and found to be in good agreement with experiments. This is followed by simulated conductance traces for CO in Au,Cu,Ni and Pt contacts. The conductance property of CO is found to be determined to a large extent by the pure metal contact, and we assign the fractional conductance peak at $0.5G_0$ to a particular CO configuration. Finally, vibrational calculations are presented for Pt/CO.

The result on Pt and Pt/CO may be found in Paper I, while the results for Au, Ni and Cu are as yet unpublished.

8.1 Summary of experimental results

In this section a brief summery of the experimental data obtained for CO in metal junctions by Kiguchi *et al.* [5] is presented.

The experiment was performed with the MCBJ technique described in Sec. 7.0.1. In Fig. 8.1 the conductance histogram obtained by Kiguchi *et al.* for the four different metals Au, Cu, Pt and Ni nanocontacts before (dotted line) and after (thick line) admitting CO. The clear peak at $1.5G_0$ for both Pt and Ni and $1.0G_0$ for both Cu and Au indicates typical conductances of the contacts just before breaking. Admitting a small amount of CO gas into the sample leads to a large change for the case of Pt and Ni, where the peak at $1.5G_0$ disappears, and instead new peaks appear. For both Pt and Ni a peak at $0.5G_0$ is observed.

8.2 Conductance calculations

In this section, the DFT simulated conductance traces are presented. We find that the transport properties of the Metal-CO-Metal junction is to a large extent determined by the properties of the bare metal electrodes. For this reason, we put some emphasis on verifying the ability of our method to reproduce key
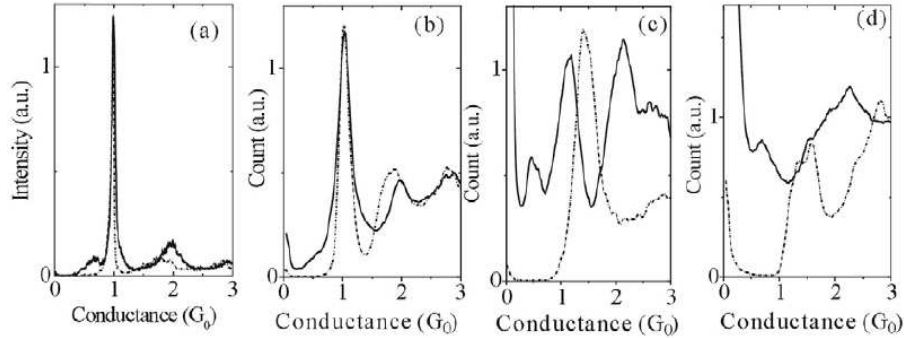
Figure 8.1: (a) Au, (b) Cu, (c) Pt, and (d) Ni contacts before (dotted line) and after (thick line) admitting CO. The figure is taken from Ref. [5].

characteristics of the transport properties of the pure Pt contacts and chains. Here we also find good agreement with experiments.

All conductance calculations have been performed using a DZP basis set and the method 2 described in Sec. 4.5.2, except the conductance calculation involving Pt which was performed using method 1 described in Sec. 4.5.1, see Paper I for more details. Furthermore, the conductance calculations for the Ni contacts was performed spin-polarized. The two-dimensional Brillouin zone of the transverse plane has been sampled by 4×4 **k**-points for all calculations and exchange and correlation effects are incorporated through the PBE functional [32].

8.2.1 Pt point contacts and chains

Mechanically controlled break junction experiments performed at cryogenic temperature on pure Pt samples show that as a Pt contact is pulled apart a structure with a characteristic conductance of around $1.5G_0$ is formed in the last stages before the contact breaks. This is inferred from conductance histograms which show a pronounced peak at this value. In addition to the peak at $1.5G_0$, many histograms on Pt contain a smaller and broader peak at around $2.1G_0$. The two peaks are believed to correspond to chains and atomic point contacts, respectively. The fact that the peak at $1.5G_0$ is higher than the peak at $2.1G_0$ is explained by the suppression of point contacts by the formation of chains, in good agreement with the high stability predicted for Pt chains in Sec 6.2. Experimental evidence for this hypothesis comes from conductance histograms recorded as the broken contacts are brought back into contact, so-called return

histograms. Such histograms contain no contributions from chains, and show a single peak at $2.1G_0$ [123].

The study of the Pt point contacts and short chains serves a dual purpose. First, it provides a theoretical justification for assigning the two peaks at $1.5G_0$ and $2.1G_0$ in the conductance histograms for Pt to chains and point contacts, respectively. Secondly, it allows us to test the ability of the calculational scheme against well established experimental results and other computer simulations before applying it to the study of CO in Pt and other metal contacts.
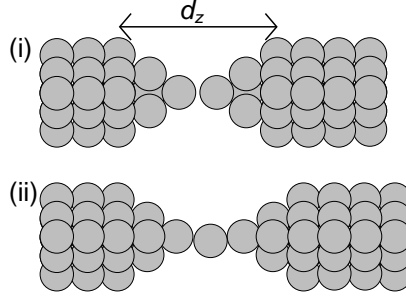

Figure 8.2: Supercells used to model the two structures considered: (i) A point-contact, and (ii) a 1-atom chain. The electrode separation d_z is defined as the distance between the (111) surfaces.

The Pt contacts are modeled using supercells with two 4-atom pyramids oriented towards each other and attached to Pt(111) surfaces containing 3x3 atoms in the surface plane. Two different structures are considered. (i) A point contact, where the apex atoms of the pyramids are in direct contact. (ii) A 1-atom chain, where a single Pt atom is inserted between the apex atoms of the pyramids, as shown in Fig. 8.2.

By increasing the electrode separation d_z, defined as the distance between the fixed (111) surfaces (see Fig. 8.2), and relaxing the pyramids at each step before calculating the conductance, we simulate the process of creating a conductance trace. The result for the point contact and short chain is shown in Fig. 8.3, where the triangles denote conductances and the circles denote the total energies measured relative to the first configuration ($d_z = 10.9$Å).

The simulated conductance trace of the point contact is in good agreement with the experimental return histograms for Pt [123], which show a peak around $2.1G_0$. Moreover, both the plateau around $2G_0$ as well as the rate of the exponential decay in the tunneling regime compare well with the calculations reported in Ref. [68].

For the short chain Pt contact the calculated conductance trace has a plateau
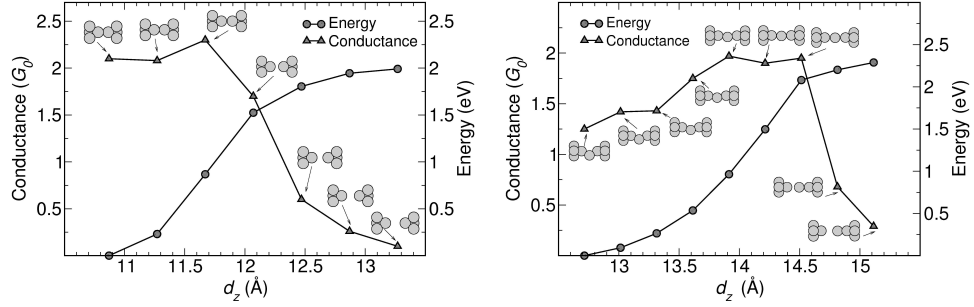
Figure 8.3: Left: Simulated conductance trace (circles) and the DFT calculated potential energy as a function of the electrode separation d_z. Right: The same, but for a short Pt chain contact.

at around $1.4G_0$ for small d_z where the chain zigzags. As the contact is stretched further, the conductance rises to a conductance just below $2G_0$, before the contact breaks at $d_z = 14.5$Å. At this point the structure relaxes towards the surfaces, and the conductance starts to decay exponentially as the tunneling regime is entered. The correlation between structural relaxations and sharp changes in the conductance is a characteristic feature of the contact formation process. The effect has been observed experimentally for gold chains by measuring the conductances and forces simultaneously [124, 13]. In fact, this has also been recently shown for Pt chains [125]. Furthermore, we note that the increase in the conductance just before the contact breaks, seen in Fig. 8.3, is also observed experimentally [125]. We stress that in order to obtain plateaus in a simulated conductance trace and thus predict the occurrence of peaks in a conductance histogram, it is necessary to allow the central atoms of the contact to relax in the elongation process.

8.2.2 CO in metal contacts

In this section we address the effect of a CO bridge on the conductance of the metal contacts. The DFT calculations identify a certain tilted bridge configuration in the last stages before rupture, which has a conductance of $\sim 0.5G_0$ for Pt and Ni and is negligible for Au and Cu. This effect is explained by the position of the metal d-band center.

As discussed in Sec. 8.1, the controlled exposure of a metal contact to a CO gas changes the conductance histogram completely for Pt and Ni, where a peak at $0.5G_0$ replaces the homogeneous contact conductance peaks at $1.5G_0$ and $1.0G_0$, respectively.

In order to understand the physical origin of the new peaks, we have carried out total energy and conductance calculations using the same setup as for the pure Pt contacts, as discussed in the preceding section. For the initial contact geometry and small d_z, CO is most stable at the central metal-metal bridge of the contact, bonding symmetrically with C to the two metal apex atoms in an upright bridge configuration (see the inset labeled A in Fig. 8.4).

The results are summarized in Fig. 8.4, where we show the conductance as a function of the electrode separation d_z. Clearly, Pt (diamond) and Ni (triangle)
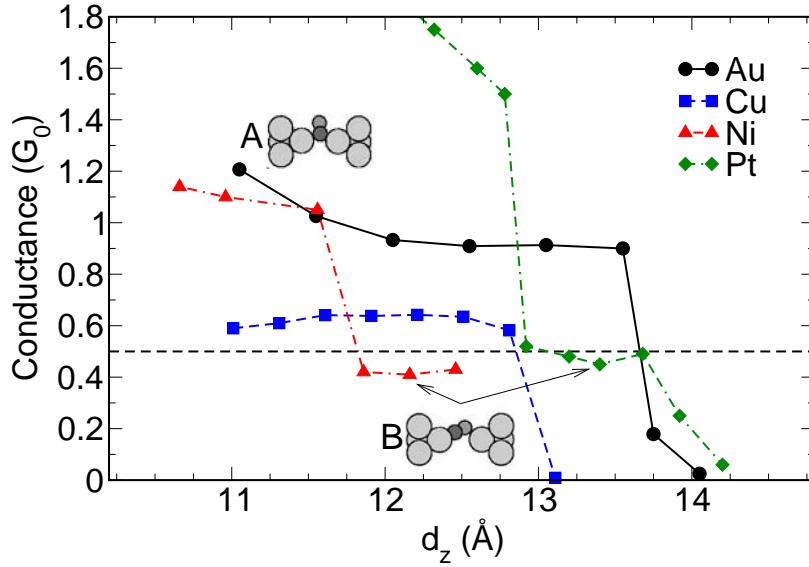

Figure 8.4: The conductance as a function of the electrode displacement d_z for Au,Cu,Ni and Pt contacts in the presence of a single CO molecule.

show a conductance close to $0.5G_0$ in the last stages before the contact break. Prior to reaching the $0.5G_0$ plateau a sudden jump can be observed in the conductance, which is related to one of the C-Pt or C-Ni bonds breaking, and the contact relaxing to a tilted bridge structure as shown in the inset labeled B. For Au and Cu a transition to the tilted bridge configuration does not lead to a plateau at $0.5G_0$ but rather a sudden jump into the tunneling regime. These results are in qualitative agreement with the experimental results [5]. However, we observe a suppression of the conductance for Cu, which would lead to a peak in the conductance histogram shifted slightly down below $1G_0$. In the experiments the peak for the pure contact at $1G_0$ is not shifted down but is nevertheless broadened.

Based on this, we propose that the observed fractional conductance value $0.5G_0$ for Pt and Ni exposed nanocontacts is due to the tilted bridge configuration.

This is illustrated further below, where we study the transport mechanism in more detail, first for Pt-CO and then more generally for Metal-CO.

Fig. 8.5a shows a typical transmission function for the upright bridge configuration (dashed line) and tilted bridge configuration (full line) immediately before and after the bridge tilts corresponding to configurations A and B in Fig. 8.4. In both cases (A and B) there is a pronounced resonance at the Fermi level, which clearly is responsible for the conductance of $1.5G_0$ and $0.5G_0$, respectively. As the following analysis will show, the resonance is not due to the CO molecule alone, but rather is a (local) band structure effect related to the d-orbitals at the Pt apex atoms.

To address the origin of this resonance, we perform an analysis of the local electronic structure in the contact region by diagonalizing the Hamiltonian within the subspace spanned by the WFs located at the CO molecule. The orbitals and eigenvalues obtained in this way represent renormalized energy levels of the CO molecule including the effect of the coupling to the Pt leads. For all the considered contact geometries, we find seven WFs located at the CO molecule, leading to seven renormalized molecular energy levels. For simplicity we focus on the tilted CO bridge in the following analysis.

Since CO has ten valence electrons, the seven renormalized CO orbitals represent the five occupied and the two lowest unoccupied molecular orbitals. The latter are the $2\pi^*$ orbitals which are known to be important for the chemisorption properties of CO [126, 127, 128]. By repeating the conductance calculations with the renormalized $2\pi^*$ orbitals removed from the basis set, we find that the resonance at the Fermi level is completely gone and the conductance is reduced to $\sim 0.05G_0$. This allows us to focus exclusively on the $2\pi^*$ CO orbitals when analyzing the transport properties of the Pt-CO-Pt contacts.

In the following, we will refer to the $2\pi^*$ states as $|a\rangle$ and $|b\rangle$. The on-site energies of these renormalized orbitals are $\varepsilon_a = 1.5$ eV and $\varepsilon_b = 1.6$ eV, respectively. The splitting of the levels is induced by the different couplings to the electrodes. Each of the molecular orbitals (MO) $|a\rangle$ and $|b\rangle$ give rise to one transmission channel through the CO molecule. If we neglect tunneling due to direct coupling between the Pt apex atoms, and neglect interference between the two transport channels, we can analyze the problem by considering the transport through each MO separately. This allow us to model the contact by a single level coupled to continuous bands (see Sec. 3.3). In the single-level model with a strong asymmetric coupling, the transmission may be expressed as
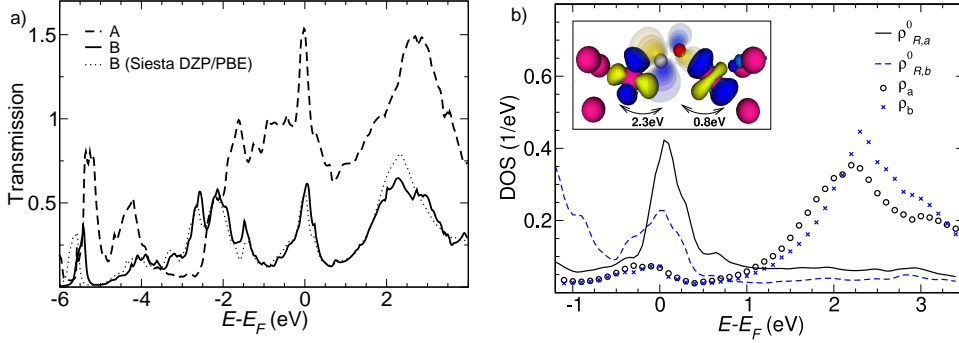
Figure 8.5: (a) Typical transmission function for the upright bridge (configuration A in Fig. 8.4) and the tilted bridge (configuration B). The dotted line is the transmission function obtained using SIESTA-DZP/PBE, while the full line is for WFs. Both transmission functions (A and B) have a resonance at the Fermi level which can be related to the density of states of the group orbitals. (b) The PDOS of the $2\pi^*$ states $|a\rangle$ and $|b\rangle$ together with the PDOS of the group orbital in the weakly coupled right lead. The inset shows an iso-surface plot of the MO $|a\rangle$ (transparent) and its corresponding left and right group orbitals (solid). The PDOS for the MOs (circles and stars) is quite flat around the Fermi level, while the the PDOS of two group orbitals (full and dashed lines) both have a peak at the Fermi level. It is this peak that gives rise to the resonance in the transmission function in (a).

$$T(\varepsilon) = 4\pi^2 V_{R,a}^2 \rho_{R,a}^0(\varepsilon)\rho_a(\varepsilon), \tag{8.1}$$

where $\rho_a(\varepsilon)$ is the projected density of states (PDOS) of the MO $|a\rangle$ and $\rho_{R,a}^0(\varepsilon)$ is the PDOS of the group orbital of the right lead in the absence of coupling to $|a\rangle$, i.e. calculated with $V_{R,a} = 0$. The limit of strong asymmetric coupling is relevant for the tilted bridge configuration, where $V_R^2/V_L^2 \approx 0.1$ for both MOs $|a\rangle$ and $|b\rangle$. The large asymmetry in the coupling strengths indicates that the Pt-C bond is much stronger than the Pt-O bond. To illustrate this situation, the inset of Fig. 8.5b) shows an isosurface plot of $|a\rangle$ (transparent) together with its left and right group orbitals (solid). The latter consists mainly of d-like orbitals centered on the apex Pt atoms. The coupling strengths $V_{L,a}$ and $V_{R,a}$ are also indicated.

In Fig. 8.5b) we show the calculated PDOS for the MOs $|a\rangle$ and $|b\rangle$ together with the PDOS of the corresponding group orbitals $|g_R^a\rangle$ and $|g_R^b\rangle$. It is clear that the transmission resonance at the Fermi level results from a corresponding peak in the PDOS of the group orbitals of the right lead, or, equivalently, from a peak in the PDOS on the d-states of the Pt apex atoms. The bare energies

of the MOs at $\varepsilon_a = 1.5$ eV and $\varepsilon_b = 1.6$ eV, respectively, are shifted upwards by the coupling to the Pt d-band, and can be seen as broad peaks in the PDOS at ~ 2.2eV. These peaks are also clearly visible in the transmission function in Fig. 8.5a).

It is well known that the DFT calculated HOMO-LUMO gap of CO is somewhat sensitive to the applied exchange-correlation functional. [128] However, since the transport properties of the investigated Pt-CO-Pt bridge involves only the tails of the PDOS of the CO orbitals and is dominated by the PDOS of the Pt leads, the exact positions of the CO energy levels are not expected to be crucial. However, an accurate description of Pt is important, and as discussed in Sec. 8.2.1, our results for Pt are in good agreement with experiments. The above analysis clearly shows that the transmission at the Fermi level is caused by the properties of the isolated Pt lead, while the role of the $2\pi^*$ CO orbitals is to provide a flat background.
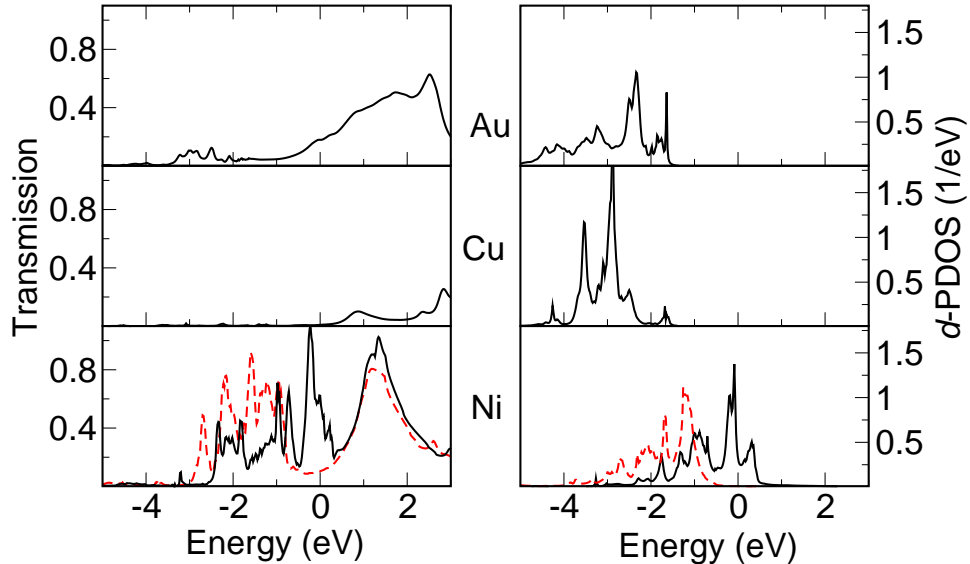

Figure 8.6: Transmission function (left) and apex atom's d PDOS (right) for Au (top), Cu (middle) and Ni (bottom) with the molecule contribution removed.

We are now ready to address the conductance behavior of Au, Cu and Ni exposed to a CO molecule. Fig. 8.6 show the calculated transmission function and weakly coupled apex atoms d-PDOS for Au, Cu, and Ni, obtained with the coupling to the molecule removed (the group orbital PDOS) in the left and right panel, respectively. Note that the Ni-CO contact spin polarizes and the current

is almost entirely carried by the minority spin electrons (black full line), while the majority spin channel (red dashed line) only has a minor contribution at the Fermi level. Clearly, the d-PDOS determines the transmission. Since neither Au nor Cu have d-states at the Fermi level, the conductance is almost zero in the tilted bridge configuration for these metals. On other hand, as with Pt, Ni does have d-states at the Fermi level, leading to a conductance of $0.5G_0$.

8.3   Vibration modes

The peak around $1.1G_0$ in the experimental histograms cannot be easily explained by our calculations for a single CO molecule in the Pt contact. We have therefore also calculated the conductance of the CO bridge in the one atom chain in search of a structure that can explain the peak at $1.1G_0$. However, we found conductances quite similar to those obtained for CO in the Pt point contact.

The vibrational frequencies of the Pt/CO structure with a conductance of $1G_0$ has been measured using point contact spectroscopy (see Sec. 7.0.2) [129].
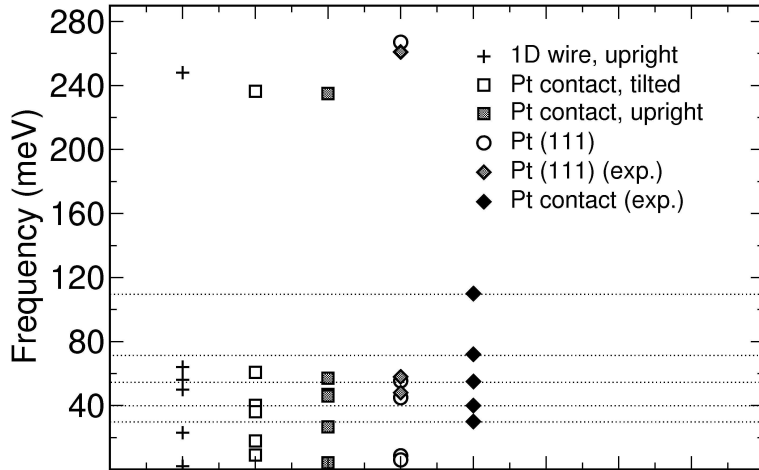

Figure 8.7: Vibrational mode calculations fo a 1D wire with CO upright (crosses), Pt contact with CO tilted (open squares), Pt contact with CO upright (filled squares), Pt(111) (open circles), Pt(111) from experiment (solid diamonds), and Pt contacts from experiment (solid diamonds). Note the anomalous frequency at ~ 110 meV from the experimental results for a Pt contact.

To gain more information about the local structure we have carried out vibrational mode calculations in the same way as for the Ag/O system, as discussed in Sec. 7.1. However, the Pt atoms have been fixed due to large mass differ-
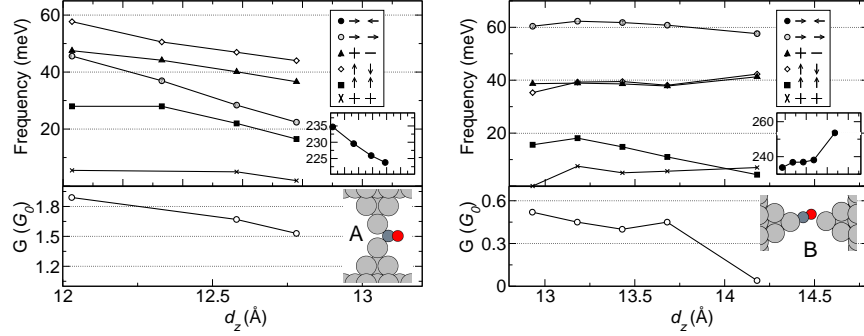
Figure 8.8: Strain induced frequency shift in meV (top) and conductance G in $G_0 = 2e^2/h$ (bottom) versus electrode separation d_z in Å for an upright (left) and tilted (right) Pt-CO-Pt contact. Insets show the internal CO frequencies for the two configurations.

ence with CO. For all the structures considered, as indicated by the legends in Fig. 8.7, we have fully relaxed both the CO molecule and Pt atoms prior to calculating the Hessian matrix. The calculation identified Pt-CO related frequencies are all located in the range between 0 and 60 meV, while the internal CO vibrational frequency is in the range between 220 and 270 meV. The calculated vibrational frequencies are to a large extend in agreement with the experiments. However, a striking exception is the experimentally observed frequency around 110 meV. Considering the quite similar vibration frequencies obtained for a variety of Pt/CO structures, we speculate that the vibrational frequency at 110 meV is not directly related to CO. This will implicitly explain why we do not observe a $1G_0$ conductance in our calculations. Furthermore to exclude a strain induced frequency shift, we have also performed vibrational calculations as a function of the electrode separation d_z. The results for the upright and tilted bridge are shown in Fig. 8.8 in the left and right panel, respectively. Also shown is the the corresponding modes and conductances. The inset shows the internal CO frequency. Clearly, no vibrational mode comes even close to 110 meV.

8.4 Summary and outlook

For the pure Pt contacts, we obtain conductance traces which are in good agreement with experiments, as well as other recent theoretical calculations. Our results show that Pt point contacts have a conductance in the range betwen 2.0 and 2.3G_0 while that of short Pt chains is between 1.3 and 2.0)G_0. This provides a theoretical justification for assigning the peaks at $\sim 2.1G_0$ and $\sim 1.5G_0$ in the

conductance histogram for Pt to point contacts and chains, respectively.

For the Pt-CO-Pt contact, we identify an energetically stable configuration with the CO molecule providing a tilted bridge between two Pt apex atoms. Based on realistic DFT simulations of the creation of a conductance trace with the elastic response of the electrodes included, we propose that the tilted CO bridge is responsible for the peak at $0.5G_0$ observed recently in the conductance histogram for Pt-CO-Pt. We characterize and explain the main features of the transmission function for the Pt-CO-Pt contact in terms of the properties of the isolated CO molecule and the free Pt leads. The analysis shows that the conductance is to a large extent determined by the local d-band of the Pt apex atoms, and to a smaller extent by the $2\pi^*$ CO orbitals. The same analysis was applied to CO in the tilted bridge configuration in Au, Cu and Ni. Since Au and Cu have filled d-bands, the group orbital density of states is zero at the Fermi level and the conductance is essentially zero. For Ni-CO we find a conductance of $0.5G_0$ in agreement with experiments. Interestingly, the transport through Ni-CO is almost completely spin-polarized, in contrast to the homogeneous Ni contact [130].

Chapter 9

Nanotubes

Carbon nanotubes (CNTs) were first discovered in 1991 by Iijima [131], and have since been the subject of an ever growing interest due to their remarkable mechanical and electronic properties. Today, light emitting diodes, transistors and extremely sensitive sensors have all been built using CNTs.

In this chapter, the atomic and electronic structure of carbon nanotubes will be introduced. A method of controlling the conductance of a CNT by site selective adsorption of molecules is also shown. Nanotubes formed from the tri-layered structures of MoS_2 and PtO_2 are then studied.

9.1 Structure of nanotubes

The ideal nanotube may be viewed as being obtained by rolling up a a strip of a quasi two dimensional (2D) layered structure into a seamless cylinder [132]. The circumference of the tube may then be choosen to correspond to an edge of the strip. To obtain a seamless tube, the strip is cutout along the chiral vector $\mathbf{C}_h$, defined by

$$\mathbf{C}_h = n_1\mathbf{a_1} + n_2\mathbf{a_2}, \tag{9.1}$$

and a vector $\mathbf{T} = t_1\mathbf{a_1} + t_2\mathbf{a_2}$ perpendicular to $\mathbf{C}_h$. In the case of a hexagonal unitcell, $\mathbf{T}$ may be obtained from the relation

$$t_2 = -t_1\frac{2n_1 + n_2}{2n_2 + n_1} \tag{9.2}$$

From Eq. 9.1 and 9.2 it may be seen that a nanotube is specified by the pair of integers: (n_1, n_2). The vectors C_h and T are illustrated in Fig. 9.1b for a graphene sheet shown in Fig. 9.1, and will yield a $(4, 4)$ carbon nanotube.
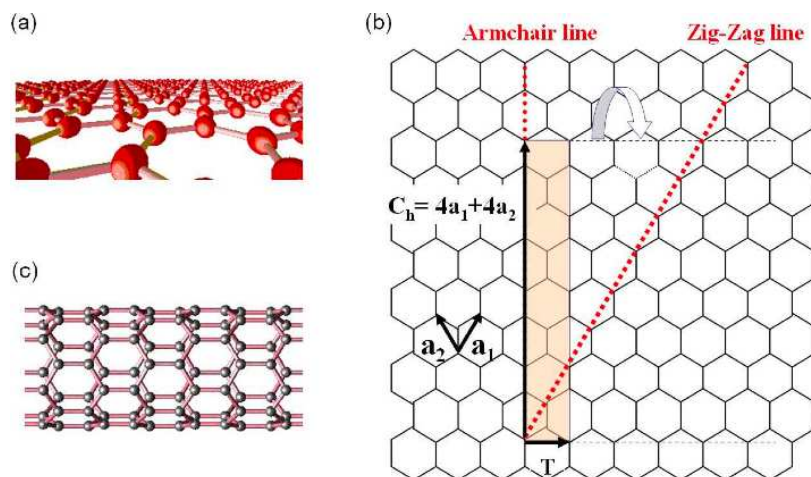
Figure 9.1: (a) Graphene layer. (b) The tranlational unit cell (shaded area) of a $(4,4)$ carbon nanotube. (c) A zig-zag nanotube obtained by folding the sheet along the zig-zag line

The generation of a nanotube may be accomplished in the three steps. (i) The N unit cell atoms are mapped to the surface of a cylinder with radius $r = |\mathbf{N}|$. (ii) The cylinder mapped N unitcell atoms are used to locate $N \times (\gcd(n_1, n_2) - 1)$ additional atoms by repeated rotation around the tube axis by the angle $2\pi/\gcd(n_1, n_2)$. (iii) The rest of the tube may now be generated by a screw operation specified by a translation h and rotation by α on the tube axis. For details about obtaining the screw operation parameters we refer to Ref. [133].

Consider a $(6,4)$ PtO_2 nanotube as an example (see below for more details). In Fig. 9.2(a) we show the atoms in the unit cell which are obtained by (i) mapping a single PtO_2 unit of α-PtO_2 to a cylindrical surface, and (ii) performing a rotation of π around the tube axis to obtain the second PtO_2 unit. To obtain the translational nanotube unit cell shown in Fig. 9.2(b) a screw operation on the helical motif is performed successively.

9.2 Site selective adsorption on carbon nanotubes

The influence of defects and adsorption of molecules on the conductance of carbon nanotubes (CNTs) is of fundamental relevance for their performance in electrical devises such as sensors. In this section, we illustrate how the conductance properties of metallic CNTs may be controlled by site selective adsorption
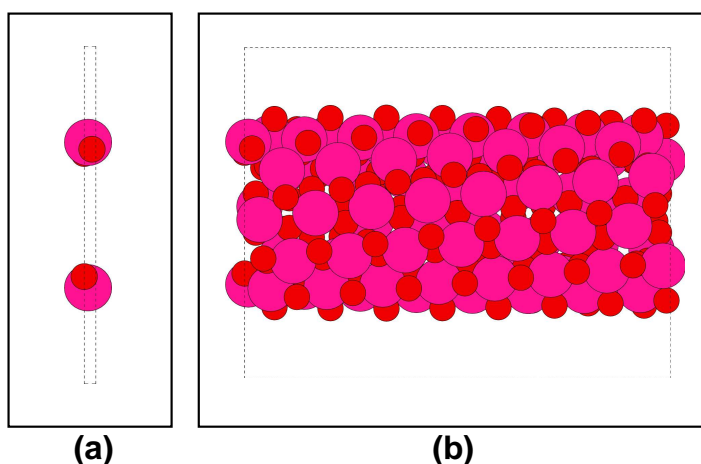
Figure 9.2: (a) Helical motif of a (6,4) PtO$_2$ nanotube, which is used to generate the tranlational unit cell shown in (b).

of molecules in a systematic fashion.

The transport calculations have been performed using method 2, as described in Sec. 4.5.1, and structures have been relaxed with the SIESTA code [3].

It is well known that an armchair CNT $(n_1, n_2 = n_1)$ is metallic, with two bands crossing the Fermi-level [134]. A defect free armchair CNT therefore has two eigenchannels [50] at the Fermi level. In Fig. 9.3(a) we show the transmission function for a $(6, 6)$ CNT where a single molecule (COOH, H, NH$_2$, NO$_2$ or OH) has been chemisorbed. The anti-resonance appears, irrespective of the particular molecular species. In fact, as the inset shows, only one of the two eigenchannels is affected by the adsorption of a molecule. This effect is independent of whether the molecule is adsorbed on one of the two inequilvalent sites of the underlying graphene sheet. To gain insight into the scattering mechanism, we consider a single hydrogen atom adsorbed on a $(6, 6)$ graphene sheet, neglecting curvature effects. In Fig 9.3(b) and 9.3(c) we show an isosurface plot of the unaffected eigenchannel state and the nearly blocked eigenchannel state, respectively. The eigenchannel states were calculated at the energy corresponding to the position of the anti-resonance according to the method described in Ref. [52]. Clearly, the fully transmitting eigenchannel state has almost no weight on the site where the H atom is adsorbed (denoted by the arrow) and on a sub
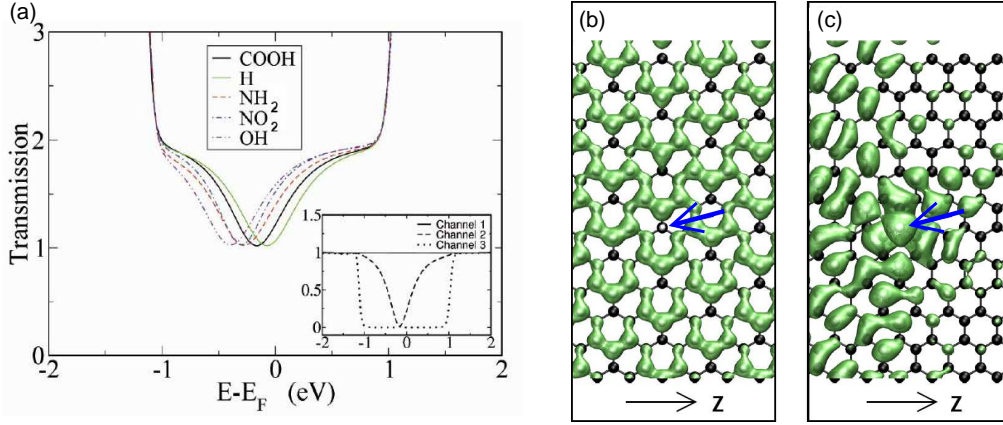
Figure 9.3: (a) Transmission functions for a (6,6) CNT with a single chemisorped molecule (COOH, H, NH_2 NO_2 or OH) on the the on top site. Inset: Eigenchannel resolved transmission (COOH). Channel 1 is unaffected while channel 2 is almost blocked at the Fermi level. Channel 3 is zero in a region near the Fermi level. (b) and (c): Isosurface plot of the unaffected and blocked eigenchannel, respectively.

lattice which may be described by the lattice vectors

$$r_1 = a_1 + a_2, \qquad (9.3)$$
$$r_2 = 2a_1 - a_2. \qquad (9.4)$$

The zero weight (ZW) sub lattice may also be expressed as the condtition: $n_1 - n_2 = 3p$, for some integer p. In fact, this is the same condition required for a carbon nanotube to be (semi-)metallic [135, 134]. Since the eigenchannel state has almost no weight on the ZW sub lattice it may be expected that adsorbing multiple molecules on the aub lattice sites will not cause further scattering. In Fig. 9.4 we show the result of adsorbing two H atoms on the ZW sublattice (red full line) and two H atoms in a number of positions not belonging to the ZW sub lattice (dashed black line). Clearly, adsorbing multiple H atoms on the ZW sublattice does not affect the fully transmitting eigenchannel. On the other hand, when the H atoms are adsorbed on sites not belonging to the ZW sublattice, both eigenchannels are effected. In fact, the transmission is now almost zero at the Fermi level. A simple tight-binding model accounting for the observed phenomena may be found in Paper IV.

To summarize, by chemisorbing a single molecule on the wall of a metallic carbon nanotube, one of the two eigenchannels near the Fermi level is blocked while the other remains unaffected. This effect seems to be generally an inde-
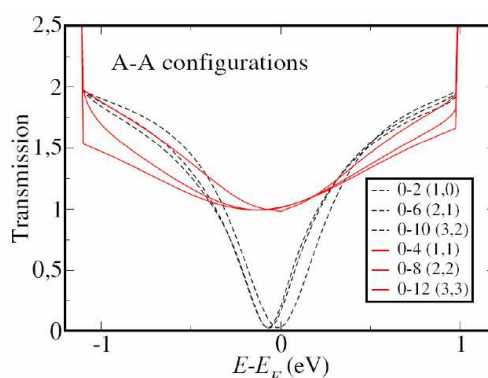
Figure 9.4: Transmission function for a $(6,6)$ CNT with hydrogen atoms placed on the ZW sub-lattice (red full curve) and on sites not in the ZW sub-lattice (black dashed curve). The (n_1, n_2) numbers indicate the position of the second H atom with respect to the first H atom.

pendent of the species of the chemisorbed molecule. Multiple molecules may be chemisorbed on the ZW sublattice without affecting the fully transmitting eigenchannel. However, adsorbing multiple molecules on sites not corresponding to the ZW sublattice leads to both eigenchannels being almost completely blocked at the Fermi level.

9.3   Non-carbon based nanotubes

In the preceding section, it was illustrated how the conductance properties could be altered by site selective control of molecules on a carbon nanotube. Another way of designing a nanotube with a desired property could be to simply use a material other than carbon. Chemical properties of large diameter tubes are expected to be similar to those of the bulk phase. For this reason, small diameter nanotubes are of the most interest. This field is still open for further reseach. However, here we take a small step in this direction by exploring two materials which are known to exist in a layered phase, namely MoS_2 and $\alpha - PtO_2$. Both consist of a metal "sandwiched" between sulfur (S-Mo-S) or oxygen (O-Pt-O). Within a single layer the atoms are arranged in a hexagonal lattice. In the case of MoS_2, the Mo atom is in a trigonal prismatic coordination to the S atoms, so that the S-Mo-S is stacked A-B-A. PtO_2 has a similar structure, but is instead A-B-C stacked.

DFT calculations in this section have been performed with the DACAPO

	DFT	Experiment
Hexagonal lattice constant (Å)	3.21	3.160
S-Mo-S layer height (Å)	3.16	3.172

Table 9.1: Calculated values for a single-layer MoS_2. Experimental structural parameters for MoS_2 are taken from Ref. [139]

code [2] using a plane wave cutoff of 25 Ry and 24 **k**-points to sample the first Brillouin zone. The PBE [32] energy functional was used to treat exchange and correlation.

We first consider MoS_2. Subnanometer MoS_2 nanotubes in a crystal structure were synthesized by Remskar *et al.* [136] and the single tube structure was proposed to be a $(3,3)$ MoS_2 nanotube. However, an extensive first principles study of small diameter MoS_2 structures did not reveal satisfactory agreement with the experiments [137]. Also, a tight-binding study [138] indicated that small diameter MoS_2 nanotubes have a higher strain energy, which indicates that they are not particularly stable.

We have performed DFT calculations for several (n,n) MoS_2 nanotubes. All structures have been relaxed until the force on any atom was below 0.035 eV/Å. The length of the supercell in the tube direction was also optimized. In order to charterize their stability, we define the strain energy per atom for a tube containing N atoms per supercell as

$$E_S = E_{\text{tube}}/N - E_{\text{sheet}}^0, \tag{9.5}$$

where E_{sheet}^0 is the energy per atom of a single infinite MoS_2 sheet. This is where the tube energy should tend to in the limit of large tube diameters. The calculated parameters for a single sheet of MoS_2 are summarized in Table 9.1. Experimental values are also shown.

In Fig. 9.5 we show the calculated strain energy as function of the diameter D, defined with respect to the Mo layer. The corresponding (n,n) values are also shown and the line is a fit to a $1/D^2$ curve. Note that the $(4,4)$ MoS_2 NT is missing in Fig. 9.5, since it spontanously "disolved" and into a cluster structure upon relaxation. We find the strain energy per atom for a MoS_2 NT is rather high when compared with a CNT. For example, at a diameter of 1 nm, the MoS_2 NT's strain energy is an order of magnitude higher than that for the corresponding CNT.

Next, we consider PtO_2. PtO_2 plays an important role as a catalyst in CO oxidation and water splitting. It has recently been suggested that the layered
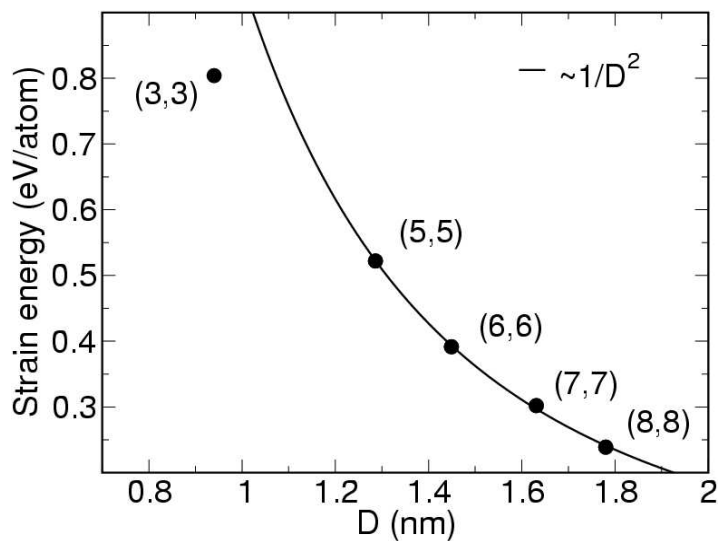
Figure 9.5: Strain energy as function of the Mo layer tube radius. The line is a $1/D^2$ fit.

	DFT	Experiment
Hexagonal lattice constant (Å)	3.18	3.10
O-Pt-O layer height (Å)	1.95	

Table 9.2: Calculated structural parameters for single layer PtO_2. Experimental data for α-PtO_2 is taken from Ref. [140]

phase α-PtO_2 is a good candidate for small diameter nanotubes [6].

In Table 9.2 we show the calculated parameters characterizing a single sheet of α-PtO_2. Note that the hexagonal lattice constant is similar to that of Mo_2. However, the layer thickness is considerably smaller.

In Fig. 9.6 we show the calculated strain energy as a function of the Pt-tube diameter for $(n, 0)$ and (n, n) nanotubes. The strain energy of $(n, 0)$ tubes studied in Ref. [6] is in good agreement with our results. However, we find that the (n, n) nanotubes have a somewhat lower strain energy at small diameters than $(n, 0)$ tubes.

The strain energy for PtO_2 is considerably lower than for MoS_2, which suggests PtO_2 may be a better candidate material for small diameter nanotubes.
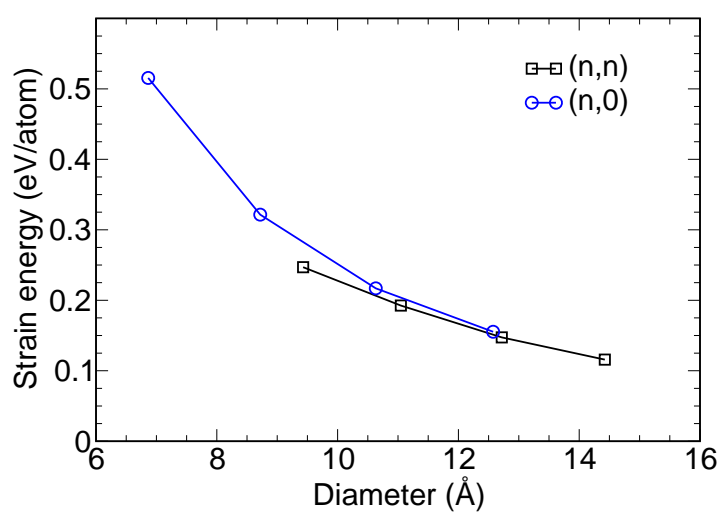
Figure 9.6: Strain energy as a function of the Pt-tube diameter.

Bibliography

[1] W. H. A. Thijssen, M. Strange, J. M. J. aan de Brugh, and J. M. van Ruitenbeek. Formation and properties of metal–oxygen atomic chains. *New Journal of Physics*, 10(3):033005 (16pp), 2008.

[2] S. R. Bahn and K. W. Jacobsen. *Comput. Sci. Eng.*, 4:56, 2002.

[3] José M Soler, Emilio Artacho, Julian D Gale, Alberto García, Javier Junquera, Pablo Ordejón, and Daniel Sánchez-Portal. The siesta method for ab initio order-n materials simulation. *Journal of Physics: Condensed Matter*, 14(11):2745–2779, 2002.

[4] C. Untiedt, D. M. T. Dekker, D. Djukic, and J. M. van Ruitenbeek. Absence of magnetically induced fractional quantization in atomic contacts. *Phys. Rev. B*, 69(8):081401, Feb 2004.

[5] M Kiguchi, D Djukic, and J M van Ruitenbeek. The effect of bonding of a co molecule on the conductance of atomic metal wires. *Nanotechnology*, 18(3):035205 (5pp), 2007.

[6] N. Seriani, Z. Jin, W. Pompe, and L. Colombi Ciacchi. Density functional theory study of platinum oxides: From infinite crystals to nanoscopic particles. *Physical Review B (Condensed Matter and Materials Physics)*, 76(15):155421, 2007.

[7] David Vanderbilt. Soft self-consistent pseudopotentials in a generalized eigenvalue formalism. *Phys. Rev. B*, 41(11):7892–7895, Apr 1990.

[8] K. S. Thygesen, L. B. Hansen, and K. W. Jacobsen. Partly occupied wannier functions. *Phys. Rev. Lett.*, 94(2):026405, 2005.

[9] Gregory H. Wannier. The structure of electronic excitation levels in insulating crystals. *Phys. Rev.*, 52:191–197, 1937.

[10] R. H. M. Smit, Y Noat, C. Untiedt, N. D. Lang, M. C van Hemert, and J. M. van Ruitenbeek. Measurement of the conductance of a hydrogen molecule. *Nature*, 419:906–909, Sep 2002.

[11] C. Joachim, J. K. Gimzewski, and A. Aviram. Electronics using hybrid-molecular and mono-molecular devices. *Nature*, 408:541–548, 2000.

[12] Jiwoong Park, Abhay N. Pasupathy, Jonas I. Goldsmith, Connie Chang, Yuval Yaish, Jason R. Petta1, Marie Rinkoski, James P. Sethna, Hctor D. Abruna, Paul L. McEuen, and Daniel C. Ralph. Coulomb blockade and the kondo effect in single-atom transistors. *Nature*, 417:722–725, 2002.

[13] G. Rubio-Bollinger, S. R. Bahn, N. Agraït, K. W. Jacobsen, and S. Vieira. Mechanical properties and formation mechanisms of a wire of single gold atoms. *Phys. Rev. Lett.*, 87(2):026101, Jun 2001.

[14] N. D. Lang. Anomalous dependence of resistance on length in atomic wires. *Phys. Rev. Lett.*, 79(7):1357–1360, Aug 1997.

[15] R. H. M. Smit, C. Untiedt, G. Rubio-Bollinger, R. C. Segers, and J. M. van Ruitenbeek. Observation of a parity oscillation in the conductance of atomic wires. *Phys. Rev. Lett.*, 91(7):076805, Aug 2003.

[16] P. Hohenberg and W. Kohn. Inhomogeneous electron gas. *Phys. Rev.*, 136:B864–B871, 1964.

[17] W. Kohn and L. J. Sham. Self-consistent equations including exchange and correlation effects. *Phys. Rev.*, 136:A1133–A1138, 1965.

[18] Mads Brandbyge, José-Luis Mozos, Pablo Ordejón, Jeremy Taylor, and Kurt Stokbro. Density-functional method for nonequilibrium electron transport. *Phys. Rev. B*, 65(16):165401, Mar 2002.

[19] K. S. Thygesen and K. W. Jacobsen. Conduction mechanism in a molecular hydrogen contact. *Phys. Rev. Lett.*, 94(3):036807, 2005.

[20] K Stokbro, J. Taylor, M Brandbyge, J.-L. Mozos, and P. Ordejón. Theoredical study of the nonlinear conductance of di-thiol benzene coupled to au(111) surfaces via thiol and thiolate bonds. *Comp. Matt. Science*, 27:151–160, 2003.

[21] M. Di Ventra, S. T. Pantelides, and N. D. Lang. First-principles calculation of transport properties of a molecular device. *Phys. Rev. Lett.*, 84(5):979–982, Jan 2000.

[22] K. Varga and S. T. Pantelides. Quantum transport in molecules and nan-otube devices. *Phys. Rev. Lett.*, 98(7):076804, 2007.

[23] M. A. Reed and C. Zhou. Conductance of a molecular junction. *Science*, 278(5336):p252 –, 1997.

[24] Nicola Marzari and David Vanderbilt. *Phys. Rev. B*, 56(20):12847–12865, Nov 1997.

[25] S. R. Bahn, N. Lopez, J. K. Nørskov, and K. W. Jacobsen. Adsorption-induced restructuring of gold nanochains. *Phys. Rev. B*, 66(8):081405, Aug 2002.

[26] W. H. A. Thijssen, D. Marjenburgh, R. H. Bremmer, and J. M. van Ruiten-beek. Oxygen-enhanced atomic chain formation. *Physical Review Letters*, 96(2):026806, 2006.

[27] Beate Paulus and Krzysztof Rosciszewski. Hartree-fock ground-state prop-erties for the group 1 alkali metals and the group 11 noble metals. *J. of Phys.: Condensed Matter*, 19(34):346217 (13pp), 2007.

[28] Chr. Møller and M. S. Plesset. Note on an approximation treatment for many-electron systems. *Phys. Rev.*, 46(7):618–622, Oct 1934.

[29] Lars Hedin. New method for calculating the one-particle green's function with application to the electron-gas problem. *Phys. Rev.*, 139(3A):A796–A823, Aug 1965.

[30] O. Gunnarsson and B. I. Lundqvist. Exchange and correlation in atoms, molecules, and solids by the spin-density-functional formalism. *Phys. Rev. B*, 13(10):4274–4298, May 1976.

[31] D. M. Ceperley and B. J. Alder. Ground state of the electron gas by a stochastic method. *Phys. Rev. Lett.*, 45(7):566–569, Aug 1980.

[32] John P. Perdew, Kieron Burke, and Matthias Ernzerhof. Generalized gra-dient approximation made simple. *Phys. Rev. Lett.*, 77(18):3865–3868, Oct 1996.

[33] John P. Perdew, J. A. Chevary, S. H. Vosko, Koblar A. Jackson, Mark R. Pederson, D. J. Singh, and Carlos Fiolhais. Atoms, molecules, solids, and surfaces: Applications of the generalized gradient approximation for exchange and correlation. *Phys. Rev. B*, 46(11):6671–6687, Sep 1992.

[34] J. J. Mortensen, L. B. Hansen, and K. W. Jacobsen. Real-space grid implementation of the projector augmented wave method. *Phys. Rev. B*, 71(3):035109, 2005.

[35] Neil. W Ashcroft and N. David Mermin. *Solid state physics.* Saunders College Publishing, 1976.

[36] Hendrik J. Monkhorst and James D. Pack. Special points for brillouin-zone integrations. *Phys. Rev. B*, 13(12):5188–5192, Jun 1976.

[37] P. E. Blöchl. Projector augmented-wave method. *Phys. Rev. B*, 50(24):17953–17979, Dec 1994.

[38] P. E. Blöchl. Projector augmented-wave method: ab-initio molecular dynamics with full wave functions. *Phys. Rev. B*, 50(24):17953–17979, Dec 1994.

[39] Henrik Bruus and Karsten Flensberg. *Many-Body quantum theory in condensed matter physics: An introduction.* Oxford University Press, 2004.

[40] L. V. Keldysh. *Soviet Physics JETP-USSR*, 20:1018, 1965.

[41] Yigal Meir and Ned S. Wingreen. Landauer formula for the current through an interacting electron region. *Phys. Rev. Lett.*, 68(16):2512–2515, Apr 1992.

[42] H. Haug and A.-P. Jauho. *Quantum Kinetics in Transport and Optics of Semi-conductors.* Springer, 1998.

[43] Daniel S. Fisher and Patrick A. Lee. Relation between conductivity and transmission matrix. *Phys. Rev. B*, 23(12):6851–6854, Jun 1981.

[44] D. M. Newns. Self-consistent model of hydrogen chemisorption. *Phys. Rev.*, 178(3):1123–1135, Feb 1969.

[45] Carter T. White and Tchavdar N. Todorov. Quantum electronics: Nanotubes go ballistic. *Nature*, 411:649–651, 2001.

[46] W. Liang, M. Bockrath, D. Bozovic, J. H. Hafner, M. Tinkham, and H. Park. Fabry-perot interference in a nanotube electron waveguide. *Nature*, 411:665–669, 2001.

[47] S. Datta. *Electronic Transport in Mesoscopic Systems.* Cambridge Univ. Press, 1995.

[48] M. Büttiker, Y. Imry, R. Landauer, and S. Pinhas. Generalized many-channel conductance formula with application to small rings. *Phys. Rev B*, 31:6207–6215, 1985.

[49] M. Cahay, M. McLennan, and S. Datta. Conductance of an array of elastic scatterers: A scattering matrix approach. *Phys. Rev B*, 37:10125–10136, 1985.

[50] Mads Brandbyge, Mads R. Sørensen, and Karsten W. Jacobsen. Conductance eigenchannels in nanocontacts. *Phys. Rev. B*, 56(23):14956–14959, Dec 1997.

[51] Emil Prodan and Roberto Car. dc conductance of molecular wires. *Phys. Rev. B)*, 76(11):115102, 2007.

[52] Magnus Paulsson and Mads Brandbyge. Transmission eigenchannels from nonequilibrium green's functions. *Physical Review B (Condensed Matter and Materials Physics)*, 76(11):115117, 2007.

[53] P. Delaney and J. C. Greer. Correlated electron transport in molecular electronics. *Phys. Rev. Lett.*, 93(3):036805, Jul 2004.

[54] Pierre Darancet, Andrea Ferretti, Didier Mayou, and Valerio Olevano. Ab initio gw electron-electron interaction effects in quantum transport. *Physical Review B (Condensed Matter and Materials Physics)*, 75(7):075102, 2007.

[55] Kristian S. Thygesen and Angel Rubio. Nonequilibrium gw approach to quantum transport in nano-scale contacts. *The Journal of Chemical Physics*, 126(9):091101, 2007.

[56] S. Kurth, G. Stefanucci, C.-O. Almbladh, A. Rubio, and E. K. U. Gross. Time-dependent quantum transport: A practical scheme using density functional theory. *Physical Review B (Condensed Matter and Materials Physics)*, 72(3):035308, 2005.

[57] P. Bokes and R. W. Godby. Conductance and polarization in quantum junctions. *Phys. Rev. B*, 69(24):245420, Jun 2004.

[58] F. Guinea, C. Tejedor, F. Flores, and E. Louis. Effective two-dimensional hamiltonian at surfaces. *Phys. Rev. B*, 28(8):4397–4402, Oct 1983.

[59] K. S. Thygesen and K. W. Jacobsen. Interference and k-point sampling in the supercell approach to phase-coherent transport. *Phys. Rev. B*, 72(3):033401, 2005.

[60] Otto F. Sankey and David J. Niklewski. Ab initio multicenter tight-binding model for molecular-dynamics simulations and other applications in covalent systems. *Phys. Rev. B*, 40(6):3979–3995, Aug 1989.

[61] E. Artacho, D. Sánchez-Portal, P. Ordejón, A. García, and J. M. Soler. *Phys. Status Solidi B*, 215:809, 1999.

[62] K. S. Thygesen, L. B. Hansen, and K. W. Jacobsen. Partly occupied wannier functions: Construction and applications. *Phys. Rev. B*, 72(12):125119, 2005.

[63] K.S. Thygesen and K.W. Jacobsen. Molecular transport calculations with wannier functions. *Chem. Phys.*, 319:111–125, 2005.

[64] N. Troullier and J. L. Martins. *Solid State Commun.*, 74:613, 1990.

[65] A. L. Yeyati, N. Agrait, and van J. M. Ruitenbeek. Quantum properties of atomic-sized conductors. *Physics Reports*, 377:81–279, 2003.

[66] A. Nitzan and M. A. Ratner. Electron transport in molecular wire junctions. *Science*, 300:1384, 2003.

[67] J. C. Cuevas, J. Heurich, F. Pauly, W. Wenzel, and Gerd Schön. Theoretical description of the electrical conduction in atomic and molecular junctions. *Nanotechnology*, 14(8):R29–R38, 2003.

[68] V. M. García-Suárez, A. R. Rocha, S. W. Bailey, C. J. Lambert, S. Sanvito, and J. Ferrer. Conductance oscillations in zigzag platinum chains. *Phys. Rev. Lett.*, 95(25):256804, 2005.

[69] David Q. Andrews, Revital Cohen, Richard P. Van Duyne, and Mark A. Ratner. Single molecule electron transport junctions: Charging and geometric effects on conductance. *The Journal of Chemical Physics*, 125(17):174718, 2006.

[70] Sergey V. Faleev, François Léonard, Derek A. Stewart, and Mark van Schilfgaarde. Ab initio tight-binding lmto method for nonequilibrium electron transport in nanosystems. *Phys. Rev. B*, 71(19):195422, 2005.

[71] John Tomfohr and Otto F. Sankey. Theoretical analysis of electron transport through organic molecules. *J. Chem. Phys.*, 120(3):1542–1554, 2004.

[72] N. Nilius, T. M. Wallis, and W. Ho. Localized molecular constraint on electron delocalization in a metallic chain. *Phys. Rev. Lett.*, 90(18):186102, May 2003.

[73] Arrigo Calzolari, Carlo Cavazzoni, and Marco Buongiorno Nardelli. Electronic and transport properties of artificial gold chains. *Phys. Rev. Lett.*, 93(9):096404, Aug 2004.

[74] D. Djukic, K. S. Thygesen, C. Untiedt, R. H. M. Smit, K. W. Jacobsen, and J. M. van Ruitenbeek. Stretching dependence of the vibration modes of a single-molecule Pt-H_2-Pt bridge. *Phys. Rev. B*, 71(16):161402, 2005.

[75] V. M. García-Suárez, A. R. Rocha, S. W. Bailey, C. J. Lambert, S. Sanvito, and J. Ferrer. Single-channel conductance of H_2 molecules attached to platinum or palladium electrodes. *Phys. Rev. B*, 72(4):045437, 2005.

[76] Y. García, J. J. Palacios, E. SanFabián, J. A. Vergés, A. J. Pérez-Jiménez, and E. Louis. Electronic transport and vibrational modes in a small molecular bridge: $h2$ in pt nanocontacts. *Phys. Rev. B*, 69(4):041402, Jan 2004.

[77] M. A. Reed and C. Zhou. Conductance of a molecular junction. *Science*, 278(5336):p252 –, 1997.

[78] Makusu Tsutsui, Yumi Teramae, Shu Kurokawa, and Akira Sakai. High-conductance states of single benzenedithiol molecules. *Appl. Phys. Lett.*, 89(16):163111, 2006.

[79] X.Y. Xiao, B.Q. Xu, and N.J. Tao. Measurement of single molecule conductance: Benzenedithiol and benzenedimethanethiol. *Nano Lett.*, 4(2):267–271, 2004.

[80] J. Ulrich, D. Esrail, W. Pontius, L. Venkataraman, D. Millar, and L.H. Doerrer. Variability of conductance in molecular junctions. *J. Phys. Chem. B*, 110(6):2462–2466, 2006.

[81] Subhasis Ghosh, Henny Halimun, Ajit Kumar Mahapatro, Jaewon Choi, Saurabh Lodha, and David Janes. Device structure for electronic transport through individual molecules using nanoelectrodes. *Appl. Phys. Lett.*, 87(23):233509, 2005.

[82] F. Evers, F. Weigend, and M. Koentopp. Conductance of molecular wires and transport calculations based on density-functional theory. *Phys. Rev. B*, 69(23):235411, Jun 2004.

[83] Hisashi Kondo, Hiori Kino, Jun Nara, Taisuke Ozaki, and Takahisa Ohno. Contact-structure dependence of transport properties of a single organic molecule between au electrodes. *Phys. Rev. B*, 73(23):235323, 2006.

[84] Eldon G. Emberly and George Kirczenow. The smallest molecular switch. *Phys. Rev. Lett.*, 91(18):188301, Oct 2003.

[85] Yongqiang Xue, Supriyo Datta, and Mark A. Ratner. Charge transfer and "band lineup" in molecular electronic devices: A chemical and numerical interpretation. *J. Chem. Phys.*, 115(9):4292–4299, 2001.

[86] San-Huang Ke, Harold U. Baranger, and Weitao Yang. Electron transport through single conjugated organic molecules: Basis set effects in ab initio calculations. *J. Chem. Phys.*, 127(14):144107, 2007.

[87] T. Shiota, A. I. Mares, A. M. C. Valkering, T. H. Oosterkamp, and J. M. van Ruitenbeek. Mechanical properties of pt monatomic chains. *Physical Review B (Condensed Matter and Materials Physics)*, 77(12):125411, 2008.

[88] Frederico D. Novaes, Antônio J. R. da Silva, E. Z. da Silva, and A. Fazzio. Oxygen clamps in gold nanowires. *Phys. Rev. Lett.*, 96(1):016104, 2006.

[89] Eduardo Anglada, José A. Torres, Félix Yndurain, and José M. Soler. Formation of gold nanowires with impurities: A first-principles molecular dynamics simulation. *Phys. Rev. Lett.*, 98(9):096102, 2007.

[90] E. P. M. Amorim, A. J. R. da Silva, A. Fazzio, and E. Z. da Silva. Short linear atomic chains in copper nanowires. *Nanotechnology*, 18(14):145701 (4pp), 2007.

[91] Y. Kondo, H. Ohnishi, and K. Takayanagi. Quantized conductance through indivial rows of suspended gold atoms. *Nature*, 395:780, 1998.

[92] A. I. Yanson, G. R. Bollinger, H. E. van den Brom, N. Agraït, and J. M. van Ruitenbeek. Formation and manipulation of a metallic wire of single gold atoms. *Nature*, 395:783–785, 1998.

[93] R. H. M. Smit, C. Untiedt, A. I. Yanson, and J. M. van Ruitenbeek. Common origin for surface reconstruction and the formation of chains of metal atoms. *Phys. Rev. Lett.*, 87(26):266102, Dec 2001.

[94] S. R. Bahn and K. W. Jacobsen. Chain formation of metal atoms. *Phys. Rev. Lett.*, 87:266101, 2001.

[95] F. Sato, A. S. Moreira, J. Bettini, P. Z. Coura, S. O. Dantas, D. Ugarte, and D. S. Galv ao. Transmission electron microscopy and molecular dynamics study of the formation of suspended copper linear atomic chains. *Phys. Rev. B*, 74(19):193401, 2006.

[96] Johannes V. Barth, Giovanni Costantini, and Klaus Kern. Engineering atomic and molecular nanostructures at surfaces. *Nature*, 437:671–679, 2005.

[97] A. Ayuela, H. Raebiger, M. J. Puska, and R. M. Nieminen. Spontaneous magnetization of aluminum nanowires deposited on the nacl(100) surface. *Phys. Rev. B*, 66(3):035417, Jul 2002.

[98] Lucas Fernández-Seivane, Víctor M. García-Suárez, and Jaime Ferrer. Predictions for the formation of atomic chains in mechanically controllable break-junction experiments. *Phys. Rev. B*, 75(7):075415, 2007.

[99] K. W. Jacobsen, J. K. Nørskov, and M. J. Puska. Interatomic interactions in the effective-medium theory. *Phys. Rev. B*, 35(14):7423–7442, May 1987.

[100] E. Tosatti, S. Prestipino, S. Kosttmeier, A. Dal Corso, and F. D. Di Tolla. String tension and stability of magic tip-suspended nanowires. *Science*, 291:288–290, 201.

[101] P. Raybaud, J. Hafner, G. Kresse, S. Kasztelan, and H. Toulhoat. Ab initio study of the $H_2 - H_2S/MoS_2$ gas-solid interface: The nature of the catalytically active sites. *J. Catal.*, 189:129, 2000.

[102] Karsten Reuter and Matthias Scheffler. Composition, structure, and stability of $RuO_2(110)$ as a function of oxygen pressure. *Phys. Rev. B*, 65(3):035406, Dec 2001.

[103] M. V. Bollinger, K. W. Jacobsen, and J. K. Nørskov. Atomic and electronic structure of MoS_2 nanoparticles. *Phys. Rev. B*, 67(8):085410, Feb 2003.

[104] Daniel Sánchez-Portal, Emilio Artacho, Javier Junquera, Pablo Ordejón, Alberto García, and José M. Soler. Stiff monatomic gold wires with a spinning zigzag geometry. *Phys. Rev. Lett.*, 83(19):3884–3887, Nov 1999.

[105] Prasenjit Sen, S. Ciraci, A. Buldum, and Inder P. Batra. Structure of aluminum atomic chains. *Phys. Rev. B*, 64(19):195420, Oct 2001.

[106] N. D. Lang and Ph. Avouris. Oscillatory conductance of carbon-atom wires. *Phys. Rev. Lett.*, 81(16):3515–3518, Oct 1998.

[107] K. S. Thygesen and K. W. Jacobsen. Four-atom period in the conductance of monatomic al wires. *Phys. Rev. Lett.*, 91(14):146801, Sep 2003.

[108] L. de la Vega, A. Martín-Rodero, A. Levy Yeyati, and A. Saúl. Different wavelength oscillations in the conductance of $5d$ metal atomic chains. *Phys. Rev. B*, 70(11):113107, Sep 2004.

[109] Y. J. Lee, M. Brandbyge, M. J. Puska, J. Taylor, K. Stokbro, and R. M. Nieminen. Electron transport through monovalent atomic wires. *Phys. Rev. B*, 69(12):125409, Mar 2004.

[110] H. Ishida. Embedded green-function calculation of the conductance of oxygen-incorporated au and ag monatomic wires. *Phys. Rev. B*, 75(20):205419, 2007.

[111] Yuanhua Qi, Daren Guan, Yuansheng Jiang, Yujun Zheng, and Chengbu Liu. How do oxygen molecules move into silver contacts and change their electronic transport properties? *Phys. Rev. Lett.*, 97(25):256101, 2006.

[112] Chun Zhang, Robert N. Barnett, and Uzi Landman. Bonding, conductance, and magnetization of oxygenated au nanowires. *Phys. Rev. Lett.*, 100(4):046801, 2008.

[113] David Jacob, J. Fernández-Rossier, and J. J. Palacios. Emergence of half-metallicity in suspended nio chains: Ab initio electronic structure and quantum transport calculations. *Phys. Rev. B*, 74(8):081402, 2006.

[114] J. Moreland and J. W. Ekin. *J. Appl. Phys.*, 58:3888, 1985.

[115] C. J. Muller, J. M. van Ruitenbeek, and L. J. de Jongh. Experimental observation of the transition from weak link to tunnel junction. *Physica c*, 191:485, 1992.

[116] L. de la Vega, A. Martín-Rodero, N. Agraït, and A. Levy Yeyati. Universal features of electron-phonon interactions in atomic wires. *Phys. Rev. B)*, 73(7):075428, 2006.

[117] Magnus Paulsson, Thomas Frederiksen, and Mads Brandbyge. Modeling inelastic phonon scattering in atomic- and molecular-wire junctions. *Physical Review B (Condensed Matter and Materials Physics)*, 72(20):201101, 2005.

[118] J.I. Martinez. Unpublished, 2009.

[119] D. M. Eigler, C. P. Lutz, and W. E. Rudge. An atomic switch realized with the scanning tunnelling microscope. *Nature*, 352:600–603, 1991.

[120] A. Aviram and M. A. Ratner. Molecular rectifiers. *Chem. Phys. Lett.*, 29:277–283, 1976.

[121] J. Reichert, R. Ochs, D. Beckmann, H. B. Weber, M. Mayor, and H. v. Löhneysen. Driving current through single organic molecules. *Phys. Rev. Lett.*, 88(17):176804, Apr 2002.

[122] Bingqian Xu and Nongjian J. Tao. Measurement of single-molecule resistance by repeatedformation of molecular junctions. *Science*, 301(5637):p1221 – 1223, 2003.

[123] S. K. Nielsen, Y. Noat, M. Brandbyge, R. H. M. Smit, K. Hansen, L. Y. Chen, A. I. Yanson, F. Besenbacher, and J. M. van Ruitenbeek. Conductance of single-atom platinum contacts: Voltage dependence of the conductance histogram. *Phys. Rev. B*, 67(24):245411, Jun 2003.

[124] G. Rubio, N. Agraït, and S. Vieira. Atomic-sized metallic contacts: Mechanical properties and electronic transport. *Phys. Rev. Lett.*, 76(13):2302–2305, Mar 1996.

[125] T. Shiota, A. I. Mares, A. M. C. Valkering, T. H. Oosterkamp, and J. M. van Ruitenbeek. Mechanical properties of pt monatomic chains. *Phys. Rev. B*, 77(12):125411, 2008.

[126] B. Hammer, Y. Morikawa, and J. K. Nørskov. Co chemisorption at metal surfaces and overlayers. *Phys. Rev. Lett.*, 76(12):2141–2144, Mar 1996.

[127] G. Blyholder. Molecular orbital view of chemisorbed carbon monoxide. *. Phys. Chem.*, 68:2772–2777, 1964.

[128] K. Doll. Co adsorption on the pt(1 1 1) surface: a comparison of a gradient corrected functional and a hybrid functional. *Surf. Science*, 573:464–473, 2004.

[129] D. Djukic. private communication, 2006.

[130] A. Smogunov, A. Dal Corso, and E. Tosatti. Ballistic conductance and magnetism in short tip suspended ni nanowires. *Phys. Rev. B*, 73(7):075418, 2006.

[131] S. Iijima. *Nature*, 354:56, 1991.

[132] J. W. Mintmire, B. I. Dunlap, and C. T. White. Are fullerene tubules metallic? *Phys. Rev. Lett.*, 68(5):631–634, Feb 1992.

[133] P. N. D'yachkov and D. V. Makaev. Account of helical and rotational symmetries in the linear augmented cylindrical wave method for calculating the electronic structure of nanotubes: Towards the ab initio determination of the band structure of a (100, 99) tubule. *Physical Review B (Condensed Matter and Materials Physics)*, 76(19):195411, 2007.

[134] J. W. Mintmire, B. I. Dunlap, and C. T. White. Are fullerene tubules metallic? *Phys. Rev. Lett.*, 68(5):631–634, Feb 1992.

[135] Noriaki Hamada, Shin-ichi Sawada, and Atsushi Oshiyama. New one-dimensional conductors: Graphitic microtubules. *Phys. Rev. Lett.*, 68(10):1579–1581, Mar 1992.

[136] Maja Remskar, Ales Mrzel, Zora Skraba, Adolf Jesih, Miran Ceh, Jure Demsar, Pierre Stadelmann, Francis Levy, and Dragan Mihailovic. Self-assembly of subnanometer-diameter single-wall mos_2 nanotubes. *Science*, 292:479–481, 2001.

[137] Matthieu Verstraete and Jean-Christophe Charlier. Ab initio study of $mos2$ nanotube bundles. *Phys. Rev. B*, 68(4):045423, Jul 2003.

[138] Gotthard Seifert, Humberto Terrones, Mauricio Terrones, Gerd Jungnickel, and Thomas Frauenheim. Structure and electronic properties of $mos2$ nanotubes. *Phys. Rev. Lett.*, 85(1):146–149, Jul 2000.

[139] Th. Böker, R. Severin, A. Müller, C. Janowitz, R. Manzke, D. Voß, P. Krüger, A. Mazur, and J. Pollmann. Band structure of $mos2$, $mose2$, and $\alpha - mote2$: angle-resolved photoelectron spectroscopy and ab initio calculations. *Phys. Rev. B*, 64(23):235305, Nov 2001.

[140] Olaf Muller* and Rustum Roy. Formation and stability of the platinum and rhodium oxides at high oxygen pressures and the structures pt3o4,beta-pto2 and rho2. *J. Less-Commen Met.*, 16:129–146, 1968.